Mechanisms of homologous chromosome synapsis and recombination in mammalian meiosis

Dissertation
for the award of the degree
"Doctor of Philosophy"
Division of Mathematics and Natural Sciences
of the Georg-August-Universität Göttingen

within the doctoral program (IMPRS-PBCS)

of the Georg-August University School of Science (GAUSS)

submitted by
Chloe Amelia Charalambous
October 2020

Thesis Committee

Dr. Melina Schuh, Department of Meiosis, Max Planck Institute for Biophysical Chemistry (MPI-BPC)

Prof. Dr. Rüdiger Behr, Department of Degenerative Diseases, Deutsches Primatenzentrum (DPZ)

Prof. Dr. Karen Alim, Department of Physics, Technical University of Munich (TUM)

Members of the Examination Board

Referee: **Dr. Melina Schuh**, Department of Meiosis, Max Planck Institute for Biophysical Chemistry (MPI-BPC)

2nd Referee: **Prof. Dr. Matthias Dobbelstein**, Institute of Molecular Oncology, Universitätsmedizin Göttingen (UMG)

Further members of the Examination Board

Prof. Dr. Matthias Dobbelstein, Institute of Molecular Oncology, Universitätsmedizin Göttingen (UMG)

Prof. Dr. Stefan Jakobs, Department of NanoBiophotonics, Max Planck Institute for Biophysical Chemistry (MPI-BPC)

Prof. Dr. Claudia Steinem, Institute for Organic and Biomolecular Chemistry, Georg-August-Universität Göttingen

Date of oral examination: 2nd December 2020

TABLE OF CONTENTS

Abstract

Homologous chromosome synapsis and recombination are key events that occur during meiotic prophase and result in the formation of chromatin structures called chiasmata. These chromatin structures physically connect homologous chromosomes, which in turn ensures that each set of homologs are correctly segregated later in meiosis. During my PhD, I identified novel aspects that promote the synapsis and recombination of homologs during mammalian female and male meiotic prophase. In addition, I devised a new method that enables mouse fetal oocytes to be studied through live-cell microscopy. The details of these findings are discussed within this thesis.

List of Abbreviations

Actin components: Actin, ARP2/3, and nm-myosin IIB

ADP: Adenosine diphosphate

ARP: Actin related protein

ATP: Adenosine triphosphate

BAC: Bacterial artificial chromosome

BLM: Bloom syndrome protein

BSA: Bovine serum albumin

CDK1: Cyclin dependent kinase 1

cDNA: Complementary deoxyribonucleic acid

ChIP: Chromatin immunoprecipitation

CMV: Human cytomegalovirus

Cyt-D: Cytochalasin-D

dHJs: Double Holliday junctions

D-loop: Displacement loop

DMC1: Disrupted meiotic cDNA protein 1

DMSO: Dimethylsulfoxide

DNA: Deoxyribonucleic acid

DNA2: DNA replication ATP-dependent nuclease 2

DNA-PKc: DNA-dependent protein kinase catalytic subunit

Dpc: Days post coitum

DSB: Double-strand break

DTT: Dithiothreitol

EDTA: Ethylenediaminetetraacetic acid

EF1α: Human elongation factor 1α

EGTA: Ethylene glycol tetraacetic acid

ERCC1: Excision repair cross-complementing rodent repair deficiency protein 1

EXO1: Exonuclease 1

FBS: Fetal bovine serum

FISH: Fluorescent in situ hybridization

g: Gravitational force

GFP: Green fluorescent protein

γH2AX: Phosphorylated H2A histone variant

HCL: Hydrochloride

HEPES: Hydroxyethyl piperazineethanesulfonic acid

HR nodules: Homologous recombination nodules

MEM: Minimal essential medium

MLH-1: MutL homolog 1

MLH-3: MutL homolog 3

MSH-4: MutS homolog 4

MSH-5: MutS homolog 5

NES: Nuclear export sequences

NHEJ: Non-homologous end joining

NLS: Nuclear localization sequences

nm: Non-muscle

NM-HC: nm-myosin II heavy chain

P_i : Inorganic phosphate

PAR: Pseudoautosomal region

PBS: Phosphate-buffered saline

PBT: Phosphate-buffered saline with triton X-100

PGCs: Primordial germ cells

PCR: Polymerase chain reaction

PP1: Protein phosphatase 1

PP2A: Protein phosphtase 2A

PRDM9: PR domain containing 9

REC8: Meiotic recombination protein 8

RNA: Ribonucleic acid

RPA: Replication protein A

SDSA: Synthesis dependent strand annealing

SSC: Saline-sodium citrate

ssDNA: single-stranded DNA

SC: Synaptonemal complex

Stra8: Stimulated by retinoic acid gene 8

SYCP: Synaptonemal complex protein

TMEJ: Theta mediated end joining

WASP: Wiskott–Aldrich Syndrome protein

WH2: WASP homology 2

XPA: Xeroderma pigmentosum Group A-complementing protein

Chapter 1: An overview of mammalian meiosis

1.0. Introduction

Meiosis is a specialized type of cell division employed by sexually reproducing organisms to generate sex-specific gametes: female egg cells and male sperm cells. Eggs and sperm originate from an identical population of primordial germ cells that differentiate into either female or male germ cells. These germ cells must undergo a wave of DNA double-strand breaks (DSBs) induced by the SPO11 endonuclease, followed by a unique period of DNA repair that involves the pairing and synapsis of homologous chromosomes. During DSB repair, at least one DSB must be repaired between each set of homologous chromosomes as an inter-homolog crossover through homologous recombination. I present in this dissertation an examination of the methods employed by mammalian germ cells to repair DSBs. In the first chapter, I discuss current knowledge regarding homologous chromosome synapsis and homologous recombination in mammalian germ cells. In the second chapter, I describe the experimental results obtained during my PhD concerning how actin and actin-associated factors are involved in homologous chromosome synapsis and recombination in male germ cells. In the third and final chapter, I describe my work towards investigating chromosome pairing in female germ cells and culturing of female germ cells to study chromosome dynamics in the context of living cells.

1.1. Establishment of meiotic germ cells in mammals

Eggs and sperm originate from a common progenitor cell type called primordial germ cells (PGCs) (McLaren, 2000). PGCs arise in the epiblast during early embryonic development and migrate to the gonadal ridge before differentiating into meiotic germ cells (Garcia-Castro et al., 1997; Ginsburg et al., 1990; Gomperts et al., 1994; Lawson and Hage, 1994; Tam and Zhou,

1996). PGCs differentiate into female germ cells called oocytes in fetal ovaries. In mice, this occurs between 12.5 and 13.5 days post coitum (dpc) (McLaren and Southee, 1997). By contrast, PGCs in fetal testes enter mitotic arrest from 12 dpc in mice and differentiate into male germ cells called spermatocytes after birth (McLaren and Southee, 1997). Initiation of both female and male meiosis requires transcriptional activation of *Stra8* (stimulated by retinoic acid gene 8) through retinoic acid signaling (Anderson et al., 2008; Dokshin et al., 2013). The delay in male meiotic initiation is achieved through expression of the P450 enzyme CYP26B1 in fetal testes that degrades signaling molecules, including retinoic acid, until after birth (Bellutti et al., 2019; Bowles et al., 2006; Koubova et al., 2006; Kumar et al., 2011; Li et al., 2009; MacLean et al., 2001). Conversely, in females the signaling molecules are not degraded during fetal development, thus leading to the expression of Stra8-responsive genes and the establishment of female germ cells in the fetus (Anderson et al., 2008; Dokshin et al., 2013).

1.2. The five stages of meiotic prophase

After meiotic initiation, both fetal oocytes and spermatocytes progress through meiotic prophase. Meiotic prophase is an extensive stage of meiosis that requires seven to eight days for completion in both mouse fetal oocytes and mouse spermatocytes (around four weeks for human fetal oocytes and three weeks for human spermatocytes) (Adler, 1996; Borum, 1961; Dietrich and Mulder, 1983). Prophase is subdivided into five chronological stages: leptotene, zygotene, pachytene, diplotene, and diakinesis (Fig. 1) (Page and Hawley, 2003). At the beginning of prophase, DNA replication generates two sister chromatids for each maternal and paternal homologous chromosome (Fig. 1). Cohesin complexes, including Rec8-containing cohesin, are installed around sister chromatids to associate them during subsequent stages of

meiosis (Klein et al., 1999; Watanabe and Nurse, 1999). Following replication, a wave of DSBs are induced, initiating the key processes of homologous chromosome synapsis and homologous recombination (Fig. 1). Through these events, DSBs are repaired and large chromosomal regions are exchanged between maternal and paternal homologous chromosomes (termed inter-homolog crossovers). Subsequently, the maternal and paternal homologous chromosomes become physically tethered by cohesin complexes (Webster and Schuh, 2017). The resulting structure termed the bivalent ensures that each set of homologous chromosomes are correctly segregated during later stages of meiosis (Hassold et al., 2007). In addition, crossover events generated by homologous recombination also rearrange alleles between maternal and paternal chromosomes, increasing genetic diversity in offspring (Coop and Przeworski, 2007).

1.3. Leptotene

1.3.1. The induction of DNA double-strand breaks

Following DNA replication, a wave of DSBs are induced during leptotene by the meiotic topoisomerase-like protein SPO11 (Fig. 1, Fig. 2) (Bergerat et al., 1997; Cao et al., 1990; Keeney et al., 1997). The location and number of DSBs induced by SPO11 is tightly regulated. In particular, PRDM9 (PR domain containing 9) binds to specific DNA sequences termed 'hot spots' throughout the genome where it catalyzes histone H3 lysine 4 trimethylation in the surrounding chromatin (Baudat et al., 2010; Brick et al., 2012; Grey et al., 2011; Myers et al., 2008, 2010). These histone modifications direct the recruitment of DSB machinery, including a set of proteins (REC114, MEI4, MEI1 and IHO1) that facilitate the recruitment and activity of SPO11 (Sasanuma et al., 2007). In humans and mice, two isoforms of SPO11 (SPO11α and SPO11β) are expressed, although SPO11β is responsible for generating the majority of meiotic

DSBs (Bellani et al., 2010). SPO11 homo-dimerizes and catalyzes DSB formation through a topoisomerase II–like mechanism, where both strands of DNA are simultaneously cut (Fig. 2) (Diaz et al., 2002; Shingu et al., 2010). SPO11 generates between 200 to 400 DSBs during mammalian meiosis though only a small minority (approximately 27 DSBs in mice) are repaired in such a way as to generate bona fide inter-homolog crossovers (Baudat and De Massy, 2007; Broman et al., 2002). Following DSB induction by SPO11, the ATM kinase is activated and negatively regulates further induction of DSBs (Lange et al., 2011). I will discuss in later sections how DSBs are repaired and how only a subset gives rise to inter-homolog crossovers.

1.3.2. Assembly of the chromosome axes

Contemporaneously to leptotene, around the time of DSB induction, sister chromatids become organized into an array of chromatin loops in a cohesin-dependent manner (Blat et al., 2002; Klein et al., 1999). Lateral synaptonemal complex proteins including SYCP3 bind to DNA at the base of chromatin loops and self-assemble into regular filamentous structures called chromosome axes (Fig. 1) (Smith and Roeder, 1997; Syrjänen et al., 2014). DSBs induced at chromatin loops are translocated to chromosome axes for repair (Blat et al., 2002; Plug et al., 1998). Numerous proteins, including Rec8-containing cohesin complexes and proteins involved in DSB repair are also recruited to chromosome axes (Watanabe and Nurse, 1999). Specifically, proteins involved in homologous recombination cluster together at DSBs generating homologous recombination nodules (HR nodules) that will repair DNA DSBs (Fig. 1) (Klein et al., 1999; Moens et al., 2002; Plug et al., 1998).

1.3.3. Homologous recombination begins with strand resection

Following DSB induction, ATM and ATR kinases phosphorylate and activate numerous proteins involved in DSB repair (Barchi et al., 2005; Bellani et al., 2005). One of the first targets of ATM phosphorylation is H2AX (an H2A histone variant) present in the chromatin surrounding a DSB (Bellani et al., 2005). ATM phosphorylates mammalian H2AX at serine-139 to generate γH2AX (Rogakou et al., 1998). Notably, γH2AX can be detected approximately 50 kilobases from a DSB (Shroff et al., 2004) and may function as a docking platform where proteins involved in DSB repair can assemble. Numerous pathways operate in cells to repair DSBs (described in more detail below). However, proteins involved in the homologous recombination repair pathway are preferentially recruited to γH2AX sites during meiosis. The first stage of homologous recombination involves resecting the DNA at DSB sites to generate single-stranded DNA (ssDNA) overhangs (Fig. 1, Fig. 2). This process is performed by the MRN (MRE11-RAD50-NBS1) complex (Keeney and Kleckner, 1995; Liu et al., 1995; De Massy et al., 1995; Sun et al., 1991). Through DNA resection, the MRN complex also removes SPO11 from the DSB site, which remained covalently linked to the 5' ends of the two broken strands of DNA (Fig. 2) (Neale et al., 2005). Further DNA resection via EXO1 (Exonuclease 1) or DNA2 (DNA replication helicase/nuclease 2) can generate ssDNA overhangs of up to 800 nucleotides in length on either side of the DSB site (Fig. 2) (Garcia et al., 2011; Lukaszewicz et al., 2015; Sun et al., 1991; Zakharyevich et al., 2010; Zhu et al., 2008). Following DNA resection, the ssDNA becomes coated by RPA (Replication Protein A) (Fig. 2). RPA is a heterotrimeric complex comprised of RPA1, RPA2, and RPA3 (Bochkareva et al., 2002). Each RPA subunit contains DNA binding domains that enables one RPA complex to bind a footprint of up to 32 nucleotides of ssDNA (Blackwell and Borowiec, 1994; Brosey et al., 2009; Deng et al., 2007; Fan and Pavletich, 2012). RPA bound to ssDNA prevents degradation of the ssDNA while perturbing the

formation of secondary DNA structures that can impede subsequent steps of homologous recombination (Alani et al., 1992; Bochkareva et al., 2002). Through the formation and protection of ssDNA overhangs, the next stage of homologous recombination termed strand invasion can occur. The process of strand invasion will be described in the next section. Notably, the formation of long ssDNA overhangs also prevents the repair of the DSB by other DSB repair pathways such as non-homologous end joining (NHEJ) and theta-mediated end joining (TMEJ). These alternative DSB pathways will be described in further detail in later sections.

1.4. Leptotene to zygotene

Homologous chromosome pairing and strand invasion generally occur between leptotene and zygotene in mammalian meiosis. Pairing of homologous chromosomes occurs when maternal and paternal homologs of each chromosome bind together within the nucleoplasm. Here, DSB sites that have been resected help in the chromosome pairing process, as discussed in the next section. It is important to note that chromosome pairing can commence in male meiosis as early as pre-leptotene, while chromosome pairing may proceed through pachytene in female meiosis (Boateng et al., 2013; O'Keeffe et al., 1997; Tankimanova et al., 2004). During strand invasion, RPA-protected ssDNA invade homologous DNA in a process directed by the recombinase proteins RAD51 and DMC1 (DNA meiotic recombinase 1) (Gaines et al., 2015; Jensen et al., 2010; Sugiyama et al., 2006; Sung, 1997). The invaded homologous DNA strands can then be used as a template for DSB repair to form either crossovers or non-crossovers (described in a later section). There are two suitable homologous DNA templates present: both the sister chromatid and the homologous chromosome contain unbroken strands of similar DNA that can be used for repair. During meiosis, homologous recombination

preferentially utilizes the homologous chromosome template for DSB repair (Sandhu et al., 2020; Schwacha and Kleckner, 1997). This preference is ensured through the pairing and synapsis of homologous chromosomes.

The transition from leptotene to zygotene requires approximately 36 hours (Adler, 1996; Borum, 1961; Dietrich and Mulder, 1983). Entry into zygotene is identifiable by labeling of chromosome axes by SYCP3, which has extended along the entire length of each chromosome (Fig. 1). In addition, a marked increase in RPA and RAD51/DMC1 proteins are present at HR nodules along chromosome axes (Moens et al., 2002; Plug et al., 1998). In the next section I will discuss the processes involved in homologous chromosome pairing, alignment, and synapsis. Following this, I will describe how strand invasion occurs.

1.4.1. The pairing and alignment of homologous chromosomes leads to synapsis

A fundamental question that underlies homologous recombination is how two homologous chromosomes can search the nucleoplasm to find and pair with each other. The process of homologous chromosome pairing appears to be strictly regulated, since the maternal and paternal homologs of each chromosome preferentially pair together instead of with different chromosomes. Indeed, non-mammalian organisms utilize a variety of strategies to regulate the pairing of homologous chromosomes. Homolog pairing occurs through the coupling of chromosome-specific proteins (e.g. *C.elegans*), or through interactions between RNA and RNA binding proteins (e.g. *S.pombe*) with specific DNA sequences that are uniquely located on each homologous chromosome (Ding et al., 2012, 2019; Phillips and Dernburg, 2006; Phillips et al., 2009). In both of these examples, DNA sequences act as ‘barcodes’ that enable the unique

identification of homologous chromosomes and nucleate pairing during meiosis via protein-protein interactions.

The molecular mechanisms that drive specificity in the pairing of homologous chromosomes in mammalian meiosis remain unknown, though cohesins and rapid chromosome movements have been implicated in promoting chromosome pairing (Fig. 1) (Ding et al., 2007; Horn et al., 2013; Ishiguro et al., 2014; Lee et al., 2015; Link et al., 2014; Morimoto et al., 2012; Shibuya et al., 2014a, 2015). In mammals, pairing of homologous chromosomes occurs from pre-leptotene to zygotene in male meiosis and from leptotene to pachytene in female meiosis (Boateng et al., 2013; Ishiguro et al., 2014; O'Keeffe et al., 1997; Scherthan and Schönborn, 2001; Scherthan et al., 1996, 1998; Tankimanova et al., 2004). Between leptotene and zygotene, chromosomes move rapidly within the nucleus. The rapid movements may allow chromosomes to search for their homologs through transient interactions between chromosomes. The forces that drive rapid chromosome movements are generated in the cytoplasm through actions of the motor protein dynein along microtubules (Lee et al., 2015; Shibuya et al., 2014a, 2015). SUN1/KASH5 complexes that transverse the nuclear membrane link dynein in the cytoplasm through KASH5, to telomeres in the nucleus through SUN1 (Fig. 1) (Ding et al., 2007; Horn et al., 2013; Link et al., 2014; Morimoto et al., 2012). Microtubule-induced forces can also cluster telomeres of chromosomes together, generating a structure called the chromosomal bouquet. Through either rapid chromosome movements and/or the formation of the chromosomal bouquet, homologs find each other and pair (Ding et al., 2007; Horn et al., 2013; Lee et al., 2015; Link et al., 2014; Morimoto et al., 2012; Pfeifer et al., 2001, 2003; Scherthan et al., 1996; Shibuya et al., 2015, 2014b, 2014a; Tankimanova et al., 2004).

Regions of the homologous chromosome axes begin to align in a side-by-side parallel manner following the pairing of homologous chromosomes. Alignment is the subsequent step following homologous chromosome pairing. The pairing of homologous chromosomes may occur only at one or a small number of sites between the homologous chromosomes. However, alignment ensures that the entire lengths of homologous chromosomes become adjacent to each other so that homologous, or syntenic, regions are side by side. In mammalian meiosis, pairing and alignment of homologs is generally asynchronous, as smaller chromosomes tend to pair and align before larger chromosomes (Scherthan and Schönborn, 2001). Alignment facilitates RAD51/DMC1-mediated strand invasion between homologous chromosomes (Ding et al., 2007; Shibuya et al., 2014a, 2015). Indeed, RAD51/DMC1-mediated strand invasion can itself promote the pairing and alignment of homologous chromosomes (Kauppi et al., 2013; Rockmill et al., 1995). This indicates that the processes of homologous chromosome pairing and strand invasion facilitate each other. Together these processes initiate the formation of inter-homolog crossovers.

At sites where homologs have started to align, the synaptonemal complex (SC) assembles between the chromosome axes of the two homologous chromosomes to stabilize alignment (Fig. 1). This process is termed synapsis. The SC is a tripartite structure comprised of two lateral elements (assembled along the two homologous chromosome axes) that are held together by transverse filaments (Fig. 1) (Gao and Colaiácovo, 2018). The lateral SC elements are first installed along chromosome axes during leptotene and include the SC proteins SYCP2 and SYCP3 (Fig. 1). During zygotene, the transverse filaments assemble between the lateral elements. The transverse filaments are comprised of homodimers of the SC protein SYCP1 (Fig. 1). SYCP1 associates with the lateral elements on the two homologous chromosome axes

by anti-parallel interactions at the C-terminal end (Fig. 1) (Anderson et al., 2005; Hernández-Hernández et al., 2016; Schild-Prüfert et al., 2011). In mice, SC assembly is first initiated at DSB sites during zygotene (Romanienko and Camerini-Otero, 2000). Installation of transverse filaments continues between homologous chromosomes outwards from DSB sites. By the third stage of meiotic prophase (pachytene), the SC has assembled along the entire length of homologous chromosome axes (Fig. 1). SC assembly maintains aligned homologous chromosomes approximately 200 nm from each other, with homologous regions oriented in a parallel manner (Prakash et al., 2015; Schücker et al., 2015).

Pairing of male sex chromosomes requires additional consideration. Oocytes contain a maternal and a paternal copy of the X sex chromosome and can fully synapse. Conversely, spermatocytes contain a paternal Y chromosome and a maternal X chromosome and do not fully synapse. In spermatocytes, SYCP1 transverse filaments are only installed between the homologous chromosome axes of the pseudo-autosomal regions (PAR) of the X and Y chromosomes (Baudat et al., 2013). Indeed, DSBs are induced throughout the X and Y chromosomes in males, though only the PAR region undergoes inter-homolog crossover repair. In this way, the non-homologous regions of X and Y chromosomes are unable to generate inter-homolog crossover sites (described in a later section).

Overall, homologous chromosome pairing is a complex process that is facilitated by rapid chromosome movements. After homologs are paired (through a mechanism that remains unclear in mammals), alignment brings the axes of the homologous chromosomes together in a parallel orientation. Subsequently, aligned homologous chromosome axes are stabilized by the installment of the SC, leading to homologous chromosome synapsis. Synapsis stabilizes

homologous chromosomes together in close proximity, which facilitates homologous recombination events such as strand invasion and inter-homolog crossover formation. The subsequent events of homologous recombination are described below.

Figure 1. Mammalian meiotic prophase. Shown on next page. Meiotic prophase can be divided into five stages termed leptotene, zygotene, pachytene, diplotene, and diakinesis. The morphology of chromosomes during prophase is illustrated by the maternal (pink) and paternal (blue) homologous chromosomes, each comprised of two sister chromatids. Homologous recombination commences after the induction of DNA double-strand breaks (DSBs) during leptotene and is completed by the end of pachytene. Proteins involved in homologous recombination cluster at DSB sites, generating homologous recombination nodules. Steps involved in homologous recombination (strand resection, strand invasion, and crossover/non-crossover formation) occur in the stages of prophase depicted (arrows do not accurately depict duration). Homologous chromosomes pair, align, and synapse between leptotene and pachytene. This enables homologous chromosomes to be utilized as a template for DSB repair through homologous recombination. The pairing and alignment of homologs is facilitated by the induction of rapid chromosome movements (depicted as arrows). SUN1/KASH5 on the nuclear membrane associate with both the microtubule associated motor protein dynein (not depicted), and, the telomeres of chromosomes (not depicted). Through these interactions, microtubule forces in the cytoplasm drive chromosome movements in the nucleus. Chromosome axes are assembled along the base of chromatin loops of chromosomes during leptotene. Synapsis of maternal and paternal homologs starts during zygotene through the assembly of the synaptonemal complex, comprised of lateral elements (e.g. SYCP3) on the chromosome axes and transverse filaments (SYCP1). The transverse filaments are comprised of SYCP1 homodimers, which associate with the lateral elements through the C-terminal ends and associate with other SYCP1 homodimers through the N-terminal ends, as depicted. After homologous chromosome synapsis is complete, the final stage of homologous recombination can occur, where DSBs are repaired as either crossovers or non-crossovers. Crossovers between homologous chromosomes (inter-homolog crossovers) can mature into chiasmata, chromatin structures that hold homologous chromosomes together (a single chiasma is depicted). During diplotene, the synaptonemal complex disassembles from chromosomes. Following this, germ cells enter the final stage of prophase (diakinesis) before transitioning into meiosis I where segregation of homologous chromosomes occurs (not depicted).

Figure 1

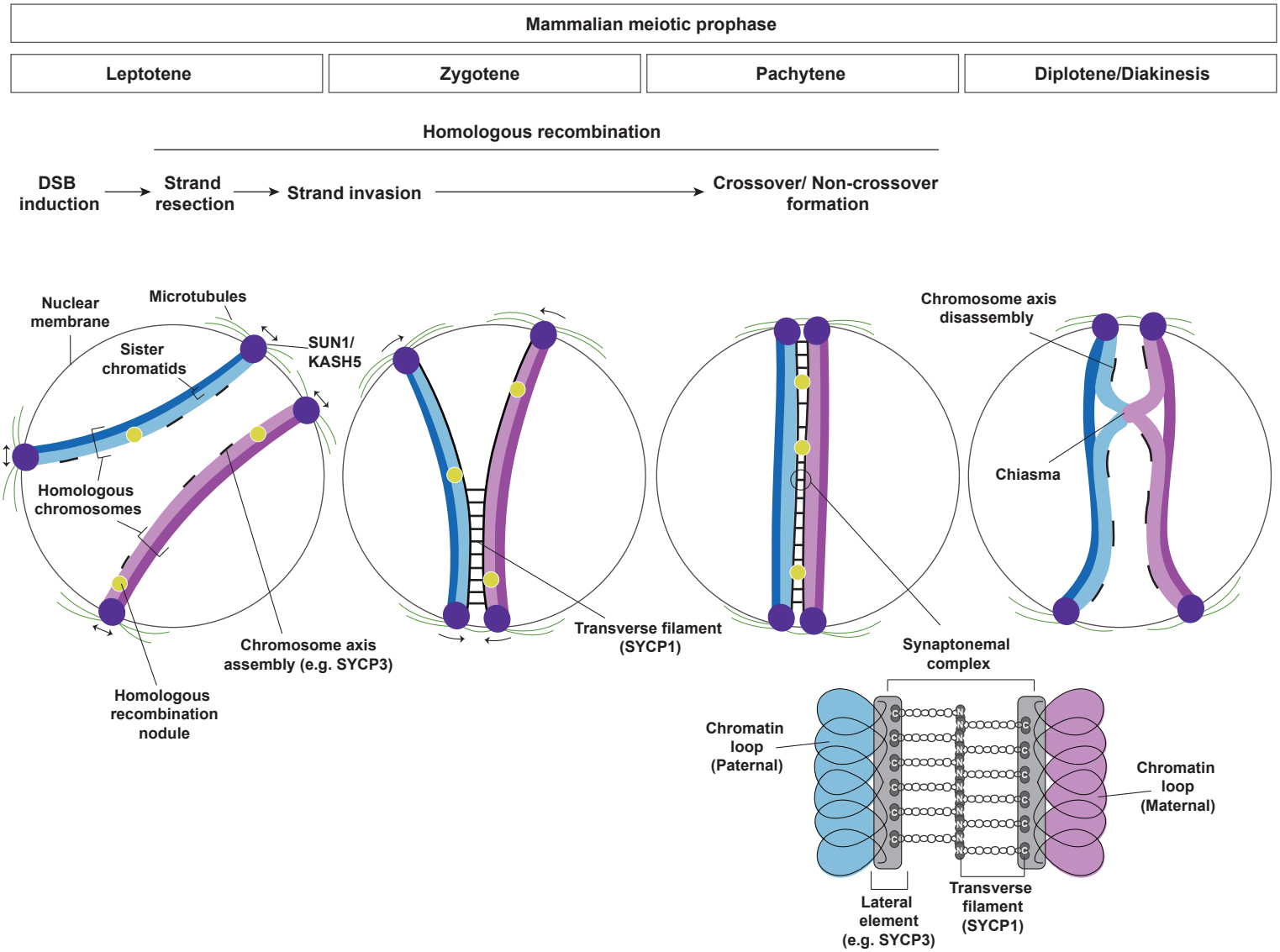
Mammalian meiotic prophase
Leptotene
Zygotene
Pachytene
Diplotene/Diakinesis
Homologous recombination
DSB induction
Strand resection
Strand invasion
Crossover/ Non-crossover formation
Nuclear membrane
Microtubules
Sister chromatids
SUN1/ KASH5
Homologous chromosomes
Chromosome axis assembly (e.g. SYCP3)
Homologous recombination nodule
Transverse filament (SYCP1)
Chromosome axis disassembly
Chiasma
Synaptonemal complex
Chromatin loop (Paternal)
Chromatin loop (Maternal)
Lateral element (e.g. SYCP3)
Transverse filament (SYCP1)

1.4.2. Strand invasion initiates the formation of a D-loop intermediate between homologs

Synchronous to homologous chromosome pairing, alignment, and synapsis, the strand invasion stage of homologous recombination begins to take place. Strand invasion is initiated when RAD51 and DMC1 recombinases are recruited to RPA-coated ssDNA (Fig. 2) (Gaines et al., 2015; Jensen et al., 2010; Sugiyama et al., 2006; Sung, 1997). Each RAD51 and DMC1 subunit can bind to three nucleotides of ssDNA (Chen et al., 2008). Many RAD51/DMC1 subunits associate along ssDNA that can be up to 800 nucleotides in length (Sun et al., 1991). This leads to the assembly of a RAD51/DMC1-DNA nucleoprotein filament, which can elongate the associated ssDNA by 1.5-fold in length through the stretching of phosphodiester bonds between nucleotides (Chen et al., 2008). Nucleoprotein filaments are capable of searching through the nucleoplasm to locate a region of sequence homology within the genome (Haber, 2018), and as mentioned earlier may assist in pairing and alignment of homologs (Kauppi et al., 2013; Rockmill et al., 1995). Several studies indicate that RAD51 mediates homology search by sliding along DNA segments to test base-pair alignment (Ragunathan et al., 2012; Renkawitz et al., 2013). As described earlier, the DNA sequence in the homologous chromosome is utilized as the template during homologous recombination in meiosis. Once the homologous DNA sequence is identified, the RAD51/DMC1-coated ssDNA translocates into the homologous DNA duplex through what is termed strand invasion (Fig. 2). The invading ssDNA nucleoprotein filament creates a displacement loop (D-loop) where the ssDNA locally displaces the annealed DNA duplex of the homologous chromosome (Fig. 2) (Chen et al., 2008). Notably, RPA persisting on the ssDNA during homology search enhances the efficiency of strand invasion (Wang and Haber, 2004). Strand invasion between sister chromatids is as rapid and efficient as strand invasion between homologous chromosomes (Haber, 2018). However, D-loops formed between sister chromatids are rapidly dissociated during meiosis

by MPH1/FANCM proteins (Sandhu et al., 2020). This ensures that strand invasion is predominantly induced between homologous chromosomes.

In summary, RAD51/DMC1 mediate strand invasion by searching for complementary DNA sequences in the adjacent homologous chromosome. The invading ssDNA creates a D-loop intermediate, which is essential for the repair of the DSB site as either a crossover or a non-crossover during pachytene. The entry into pachytene and the repair of DSBs through either crossover or non-crossover formation will now be discussed.

1.5. Zygotene to pachytene

The transition from zygotene to pachytene takes place over approximately 36 hours (Adler, 1996; Borum, 1961; Dietrich and Mulder, 1983). Pachytene is identified when the SC is fully assembled between homologous chromosome axes marking the completion of synapsis (Fig. 1). In addition, RPA and RAD51/DMC1 proteins are slowly removed from HR nodules along chromosome axes (Moens et al., 2002; Plug et al., 1998). Correspondingly, proteins involved in crossover and non-crossover formation begin to accumulate at HR nodules. Pachytene is the longest stage of meiotic prophase and can last up to 3 days (Adler, 1996; Borum, 1961; Dietrich and Mulder, 1983). This prolonged stage ensures that a sufficient number of inter-homolog crossovers are installed between homologs and that the remaining DSBs are repaired with fidelity. Indeed, every pair of homologous chromosomes requires at least one inter-homolog crossover for the successful completion of meiosis. The processes involved in generating inter-homolog crossovers and repairing remaining DSBs will now be described.

1.6. Pachytene

1.6.1. Homologous recombination induces crossovers and non-crossovers

Following strand invasion and D-loop formation, the 3' end of the invading ssDNA anneals to the complementary template strand at the D-loop (Fig. 2). Subsequently, the ssDNA is extended by DNA polymerases (including polymerase δ) using the complementary strand as a template (Fig. 2) (McVey et al., 2016). After initial extension of the ssDNA, the homologous recombination pathway can branch into three consecutive pathways namely, the synthesis-dependent strand annealing (SDSA) pathway; the class II crossover pathway; and the class I crossover pathway (Fig.2). These different pathways promote the repair of DSBs through the formation of non-crossovers (SDSA pathway) and crossovers (class I and class II crossover pathways) (Fig. 2) (Gray and Cohen, 2016). In particular, the SDSA pathway arises directly following initial ssDNA extension (Fig. 2) (Allers and Lichten, 2001). Through the SDSA pathway, the extended ssDNA is destabilized from the D-loop and displaced back to the DSB site. From here the extended ssDNA serves as a template for the extension and repair of the other ssDNA at the DSB site (Fig. 2) (Allers and Lichten, 2001). Alternatively, if the ssDNA is not destabilized, the invading ssDNA can be further extended at the D-loop. From here, the D-loop can associate with the other side of the DSB, a process called second end capture (Fig. 2). Consequently, the 3' end of the other ssDNA can anneal to the complementary template strand before extension by DNA polymerases (Fig. 2) (Gray and Cohen, 2016). Extension of the second ssDNA leads to the formation of a joint DNA molecule comprised of the two damaged (extended) DNA strands and the two template DNA strands (Fig. 2) (Gray and Cohen, 2016). At this stage, the class II crossover pathway can be employed (Fig. 2) (Gray and Cohen, 2016; Hollingsworth and Brill, 2004). Components of the class II crossover pathway cleave DNA strands at specific sites in the joint DNA molecule (Fig. 2) (Jessop and Lichten, 2008; Osman et

al., 2003). This enables the four DNA strands of the joint DNA molecule to be recombined and resolved into two DNA duplexes (Fig. 2) (Jessop and Lichten, 2008; Osman et al., 2003). Together, extension of the damaged DNA strands at the joint DNA molecule and resolution of the joint DNA molecule into DNA duplexes repairs the DSB. Finally, if the joint DNA molecule is not cleaved by components of the class II crossover pathway, the damaged DNA strands can be further extended before becoming covalently linked to the template DNA strands, generating a double Holliday junction (dHJ) (Fig. 2) (Gray and Cohen, 2016). Here, the class I crossover pathway can be employed (Cannavo et al., 2020). Components in the class I crossover pathway cleave DNA strands at specific sites in the dHJ, enabling the four DNA strands of the dHJ to be recombined and resolved into two DNA duplexes (Fig. 2) (Rogacheva et al., 2014; Zakharyevich et al., 2012). Similar to the class II crossover pathway, extension of the damaged DNA strands at the dHJ and resolution of the dHJ into DNA duplexes repairs the DSB.

It currently remains unclear how the three repair pathways (SDSA, class II crossover, and class I crossover) are specified to each DSB site. However, of the hundreds of DSBs induced by SPO11 only a minority are resolved through the class I and class II crossover pathways as inter-homolog crossovers (Holloway et al., 2008; Plug et al., 1998). In mice, approximately 27 DSBs in the genome are resolved as inter-homolog crossovers, where one or two inter-homolog crossovers typically form between each of the 20 pairs of homologous chromosomes (Broman et al., 2002). While inter-homolog crossovers are essential for successful meiosis, most DSBs are repaired through the SDSA pathway as non-crossovers (Allers and Lichten, 2001; McMahill et al., 2007). Interestingly, the DSBs that are repaired as non-crossovers facilitate homologous chromosome alignment through RAD51-mediated strand invasion (Zickler, 2006). Through the

SDSA pathway, relatively small DNA sequences are unidirectionally transferred from the homologous DNA template to the chromosome that originally contained the DSB. This method of DSB repair generates non-crossovers (Fig. 2) (Allers and Lichten, 2001; McMahill et al., 2007). In contrast, through the class II and class I crossover pathways, large DNA sequences are exchanged (crossed-over) between maternal and paternal chromosomal regions through the resolution of joint DNA molecules and dHJs (Fig. 2) (Baudat et al., 2013). Thus, the class II and class I crossover pathways repair DSBs as crossovers, and specifically inter-homolog crossovers when the homologous chromosome is utilized as the template.

In mice, approximately 90% of inter-homolog crossovers are produced by the class I crossover pathway and the remaining 10% are formed through the class II crossover pathway (Holloway et al., 2008, 2011). The exchange of large DNA sequences between homologous chromosomes through inter-homolog crossover formation generates genetic diversity between gametes (Baudat et al., 2013). In addition, the process of inter-homolog crossover formation links homologous chromosomes through specialized chromatin structures called chiasmata (Fig. 1). At a chiasma, the sister chromatid of one homologous chromosome recombines with a sister chromatid of the other homologous chromosome (Pollard et al., 2017). As a result, the Rec8-containing cohesin complexes that once linked sister chromatids together now links homologous chromosomes together, forming a bivalent chromosome structure (Watanabe and Nurse, 1999). These changes in homologous chromosome architecture are sufficient to secure homologous chromosomes together, and ensure that each set of homologs are correctly segregated during later stages of meiosis (Hassold et al., 2007).

It should be noted that if homologous recombination between homologous chromosomes fails to occur by mid-pachytene, DSBs can be repaired through homologous recombination using the sister chromatid as a template (Sandhu et al., 2020), leading to the generation of inter-sister crossovers and inter-sister non-crossovers. Alternatively, unrepaired DSBs can also be repaired through the NHEJ or TMEJ pathways from mid-pachytene (described in further detail in a later section) (Macaisne et al., 2018; Martin et al., 2005; Smolikove et al., 2007; Yin and Smolikove, 2013). These processes ensure that DSBs are effectively repaired by the end of meiotic prophase. In the next section I will describe the components involved in the SDSA, class II crossover, and class I crossover pathways.

1.6.2. The SDSA pathway destabilizes D-loops and directs the repair of DSBs as non-crossovers

RecQ helicases and the topoisomerase Top3 are key components involved in the SDSA pathway. In particular, these proteins unwind the invading ssDNA from the homologous DNA template strand (Kaur et al., 2015; De Muyt et al., 2012; Oh et al., 2007; Tang et al., 2015). Consequently, the D-loop structure is destabilized and the invading ssDNA is translocated back to the DSB site (Fig. 2). As the ssDNA was extended following D-loop formation, it can serve as a template for repair of the complementary ssDNA at the DSB site (Fig. 2). Through subsequent DNA synthesis and ligation of the DNA ends the DSB is repaired into a non-crossover (Allers and Lichten, 2001; McMahill et al., 2007). As previously mentioned, bidirectional exchange of DNA between homologous chromosomes does not occur through the SDSA pathway. Instead a DNA sequence from the homologous template is unidirectionally transferred via the extended ssDNA to the chromosome that originally contained the DSB (Fig. 2). This can result

in gene conversion, where the allele of a gene becomes identical between homologous chromosomes following DSB repair (McMahill et al., 2007).

1.6.3. The class II crossover pathway resolves joint DNA molecules into crossovers

The MUS81/EME1 heterodimer is a major component involved in the class II crossover pathway. MUS81 is a member of the XPF structure specific endonuclease family and requires the non-catalytic EME1 subunit for function (Ciccia et al., 2008; Jeong et al., 2008). MUS81/EME1 can recognize and cleave joint DNA molecules before dHJs arise (Osman et al., 2003). In particular, the MUS81 endonuclease is thought to cleave one side of the D-loop and the half-junction generated following second end capture (Fig. 2) (Osman et al., 2003). From here, the RecQ helicase, BLM helicase, cooperates with MUS81/EME1 in resolving and recombining the four DNA strands of the joint DNA molecule into two DNA duplexes (Jessop and Lichten, 2008). Subsequent extension and ligation of DNA ends in the DNA duplexes repairs the DSB as a crossover (Fig. 2) (Osman et al., 2003). As mentioned earlier the class I crossover pathway generates approximately 90% of inter-homolog crossovers while the remaining 10% are formed through the class II crossover pathway (Holloway et al., 2008, 2011). It remains unclear how the class I and class II crossover pathways are specified to DSB sites. However, the class II crossover pathway may be involved in repairing aberrant recombination structures that can arise during D-loop extension and joint DNA molecule formation (Holloway et al., 2011). While these aberrant structures can be repaired by Top3 and BLM helicase through the SDSA pathway they can also be shunted into the class II crossover pathway for repair (Holloway et al., 2011; Kaur et al., 2015; De Muyt et al., 2012; Oh et al., 2007; Tang et al., 2015; Zakharyevich et al., 2012).

Notably, the XPF structure specific endonuclease also resolves joint DNA molecules by interacting with the non-catalytic ERCC1 subunit (Ciccia et al., 2008; Kikuchi et al., 2013). Specifically, XPF/ERCC1 cooperates with MUS81/EME1 in the resolution of joint DNA molecules in mammalian somatic cells (Kikuchi et al., 2013) and during meiosis in *C.elegans* (Agostinho et al., 2013; O'Neil et al., 2013). Both ERCC1 and XPF are expressed in mouse spermatocytes and *Ercc1* homozygous mutant mice are infertile, indicating a role for XPF/ERCC1 in mammalian meiosis (Hsia et al., 2003; Shannon et al., 1999).

1.6.4. The class I crossover pathway resolves dHJs into crossovers

The heterodimers MSH-4/MSH-5 (MutS homolog proteins) and MLH-1/MLH-3 (MutL homolog proteins) are essential components involved in the class I crossover pathway (Bocker et al., 1999; Hollingsworth et al., 1995; Hunter and Borts, 1997; Rogacheva et al., 2014; Ross-Macdonald and Roeder, 1994). In particular, MSH-4/MSH-5 heterodimers form sliding clamps that encircle and stabilize dHJs (Fig. 2) (Snowden et al., 2004). In addition, MSH-4/MSH-5 recruits and stabilizes MLH-1/MLH-3 heterodimers to dHJs (Santucci-Darmanin et al., 2000). MLH-1/MLH-3 recognizes and cleaves dHJs through the endonuclease activity of MLH-3 (Cannavo et al., 2020; Claeys Bouuaert and Keeney, 2017; Hunter and Borts, 1997; Ranjha et al., 2014; Rogacheva et al., 2014). In particular, MLH-1/MLH-3 cleave dHJs at two exterior sides and one inner junction (Fig. 2) (Cannavo et al., 2020). Similar to the class II crossover pathway, the RecQ helicase, BLM helicase, cooperates with MLH-1/MLH-3 in resolving and recombining the four DNA strands of the dHJ into two DNA duplexes, before extension and ligation of DNA ends in the DNA duplexes repairs the DSB as a crossover (Fig. 2) (Rogacheva et al., 2014; Zakharyevich et al., 2012).

While dHJs can be resolved into crossovers as described above, dHJs can also be dissolved into non-crossovers through the functions of helicases and topoisomerases, which promote the production of two DNA duplexes without recombining maternal and paternal DNA sequences (Raynard et al., 2006). However, during meiosis the repair of dHJs is biased towards crossover formation, with the majority of non-crossovers generated through the SDSA pathway (Allers and Lichten, 2001).

1.6.5. Interplay between class I and class II crossover pathways can induce inter-homolog and inter-sister crossovers

There is likely a degree of interaction between the class I and class II crossover pathways to ensure DSBs are repaired (Holloway et al., 2011). Indeed, in *Mus81* homozygous mutant male mice, loss of the class II crossover pathway leads to an increase in MLH-1/MLH-3 foci without an increase in inter-homolog crossover frequency (Holloway et al., 2008). Notably, both class I and class II crossover pathways can induce inter-sister crossovers in addition to inter-homolog crossovers (Holloway et al., 2008; Sandhu et al., 2020). Therefore, it is plausible that in *Mus81* homozygous mutant mice, MLH-1/MLH-3 induces sufficient inter-homolog crossovers and the remaining DSB sites are repaired by MLH-1/MLH-3 through the formation of inter-sister crossovers. In comparison, double *Mus81; Mlh3* homozygous mutant male mice have fewer inter-homolog crossovers than single *Mlh3* homozygous mutant male mice, indicating that the class II crossover pathway compensates in generating inter-homolog crossovers when the class I crossover pathway is perturbed (Holloway et al., 2008).

1.7. Crossover regulation ensures chiasmata are installed between homologous chromosomes

The formation of inter-homolog crossovers is a highly regulated process. Indeed, the timing, frequency, and distribution of inter-homolog crossover formation are all regulated through processes that are still not fully understood (reviewed in Gray and Cohen, 2016). The strict control of inter-homolog crossover formation ensures that a sufficient number of chiasmata are installed at specific locations between homologous chromosomes. In this section, three key types of crossover regulation are described.

1.7.1. Crossover regulation through obligate crossover formation

During meiosis, at least one inter-homolog crossover is installed between each pair of homologous chromosomes (Broman et al., 2002; Jagielio and Fang, 1987; Polani, 1972). These obligate crossovers tend to form at certain regions along chromosomal arms termed 'hot spots' and are rarely detected around centromeres (Nambiar and Smith, 2016). Indeed, cohesin complexes found at centromeric regions can impede SPO11-mediated DSB induction (Nambiar and Smith, 2018). In addition, PRDM9 directs SPO11 away from active genomic regions (Brick et al., 2012; Grey et al., 2011). Together these processes regulate the locations where DSBs are induced. Yet, how specific DSBs are then selected to become inter-homolog crossover sites, while others are not, remains unclear.

1.7.2. Crossover interference regulates the distance between neighboring crossovers

Crossover interference is a phenomenon whereby one crossover site restricts the formation of neighboring crossovers. Following the establishment of an inter-homolog crossover, additional crossovers are prevented from being induced within the nearby genomic vicinity

(Broman et al., 2002; Rasmussen and Holm, 1984). Interestingly, the class I crossover pathway is subject to crossover interference, while the class II crossover pathway is not (Berchowitz et al., 2007; Holloway et al., 2008; De los Santos et al., 2003). However, in male mice deficient for the *Mus81* gene, loss of the class II crossover pathway leads to the appearance of additional MLH1 foci on chromosome axes (Holloway et al., 2008). This suggests that the factors normally imposing crossover interference are superseded to ensure DSB repair. It remains unknown how crossover interference is regulated, though the SC is implicated in maintaining crossover interference in *S.cerevisiae* (Sym and Roeder, 1994). Notably, the stringency of crossover interference control may differ between male and female meiosis. This is highlighted by the observation that human oocytes have on average 1.6-fold more crossovers than spermatocytes (Broman and Weber, 2000; Kong et al., 2010). Female meiotic chromosomes also have 2-fold more chromatin loops along chromosome axes than males (Tease and Hultén, 2004). Related to this observation is the finding that the chromosomal locations of crossover hot spots differ between male and female meiosis, with a higher frequency of crossovers detected towards to the telomeres in spermatocytes compared to oocytes (Brick et al., 2018; Broman et al., 1998; Kong et al., 2002). How the increase in crossover formation can be accounted for, and if male and female meiosis have different crossover interference mechanisms, remains to be determined. Other types of sex-specific regulation have also been described, including the observation that mutations in genes that affect the same process in male and female meiotic recombination lead to different severities of phenotypes (Cohen et al., 2006).

1.7.3. Crossover homeostasis ensures a sufficient number of crossovers are installed between homologous chromosomes

The number of inter-homolog crossovers installed in the genome remains fairly consistent even when the number of formed DSBs are altered (Ahmed et al., 2010; Cole et al., 2012; Kan et al., 2011; Martini et al., 2006; Schoenmakers et al., 2008). For example, inter-homolog crossovers remain consistent when either DSBs are reduced by mutating *Spo11* (Cole et al., 2012; Kan et al., 2011; Martini et al., 2006), or when DSBs are increased through treatment with DSB-inducing agents (Ahmed et al., 2010; Schoenmakers et al., 2008). Together, these findings indicate that cellular mechanisms regulate inter-homolog crossover installation, independently of DSB formation. Potentially, obligate crossover control could regulate the minimum number of crossovers installed, while crossover interference could control the maximum number of crossovers installed, together providing crossover homeostasis control (Gray and Cohen, 2016).

Figure 2. Homologous recombination during meiotic prophase. Shown on next page. (A) Homologous recombination is initiated in meiotic prophase following the formation of DNA double-strand breaks (DSBs) by SPO11 homodimers. SPO11 is released from the DSB site by endonucleolytic cleavage through the MRN complex (the DNA strands excised with SPO11 are shown in light pink). (B) The MRN complex, EXO1, and DNA2 further resect DNA strands at the DSB site, generating single-stranded DNA (ssDNA) overhangs that are protected by RPA. (C) RAD51 and DMC1 assemble along a ssDNA, generating a nucleoprotein filament that stretches the ssDNA. The nucleoprotein filament invades the DNA template located on the homologous chromosome, with maternal (pink) and paternal (paternal) homologous DNA duplexes depicted. Following this, the nucleoprotein filament displaces the annealed template DNA duplex creating a displacement loop (D-loop). (D) The invading ssDNA anneals to the complementary DNA strand and is extended by DNA polymerases using the homologous DNA template (extended DNA depicted as dashed lines). During strand invasion (C) and ssDNA extension (D), RPA continues to protect ssDNA. (I) The partially extended ssDNA can be destabilized and displaced from the D-loop by Top3 topoisomerase and RecQ helicases. The displaced ssDNA reanneals with the opposite strand at the DSB and is used as a template for extension and repair of the DSB by DNA polymerases. Here the DSB is repaired as a non-crossover through the synthesis-dependent strand annealing (SDSA) pathway. (E) Alternatively, the invading ssDNA can be further extended and the D-loop can associate with the other side of the DSB through second end capture. After extension of the second ssDNA by DNA polymerases, a joint DNA molecule comprised of the two damaged DNA strands and two template DNA strands is generated. (H) Joint DNA molecules can be cleaved by MUS81/EME1 of the class II crossover (CO) pathway as depicted by orange triangles. This enables the joint DNA molecule to be resolved and recombined into two DNA duplexes, repairing the DSB as a crossover. (F) Alternatively, damaged DNA strands can be further extended at joint DNA molecules before becoming covalently linked with the template DNA strands, generating a double Holliday junction (dHJ). (G) dHJs are stabilized by MSH-4/MSH-5 sliding clamps before being cleaved by MLH-1/MLH-3, as depicted by green triangles. These class I crossover (CO) pathway components (MSH-4/MSH-5 and MLH-1/MLH-3) facilitate the resolution of dHJs into two recombined DNA duplexes, repairing the DSB as a crossover. Note that resolution of joint DNA molecules (H) and dHJs (G) leads to the exchange (crossover) of maternal (pink) and paternal (blue) DNA sequences between homologous chromosomes. In contrast, a relatively small DNA sequence is unidirectionally transferred from one homologous chromosome to the other homologous chromosome through the SDSA pathway (I).

Figure 2

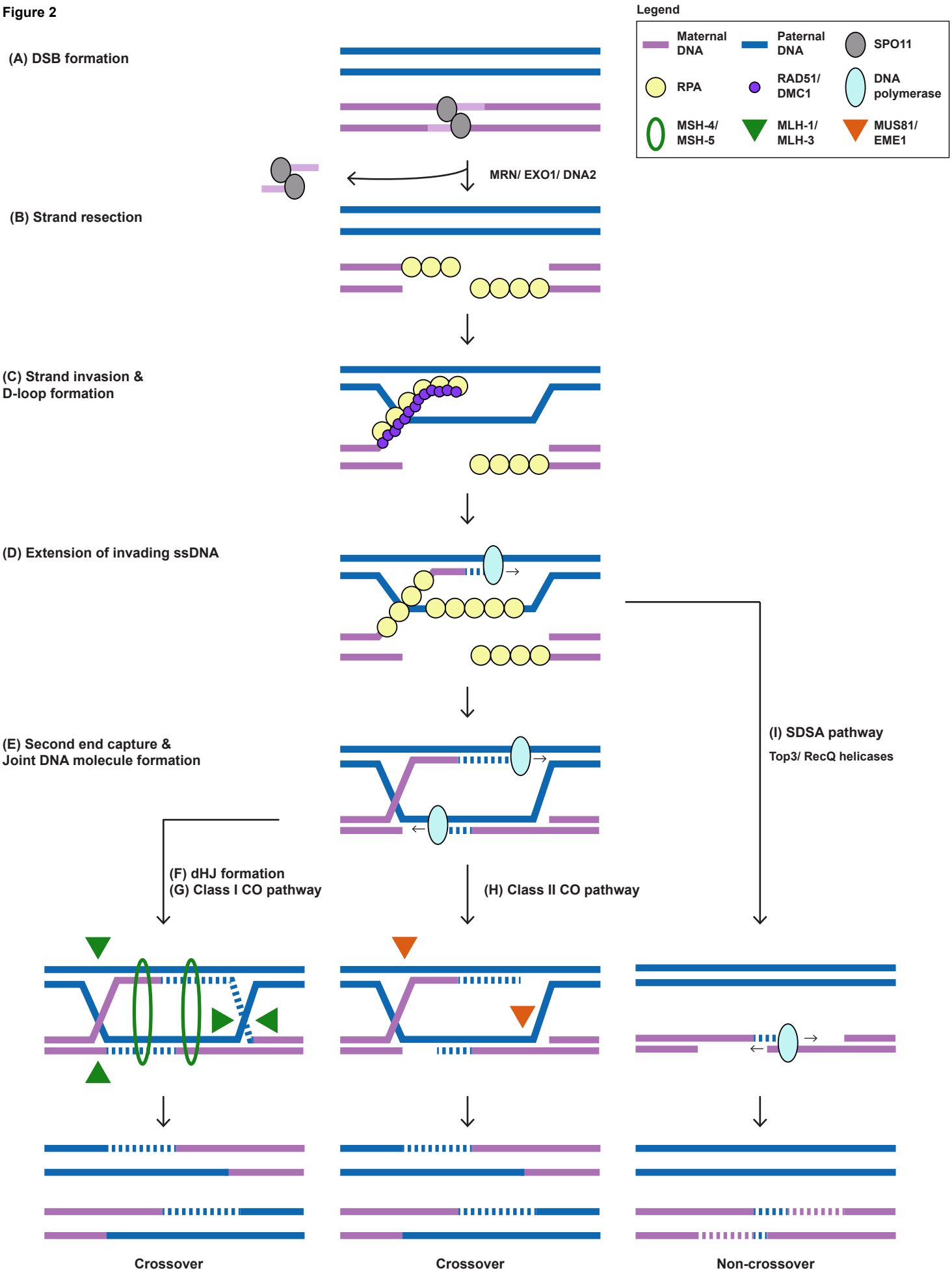
Legend
Maternal DNA
Paternal DNA
SPO11
RPA
RAD51/ DMC1
DNA polymerase
MSH-4/ MSH-5
MLH-1/ MLH-3
MUS81/ EME1
(A) DSB formation
MRN/ EXO1/ DNA2
(B) Strand resection
(C) Strand invasion & D-loop formation
(D) Extension of invading ssDNA
(E) Second end capture & Joint DNA molecule formation
(I) SDSA pathway
Top3/ RecQ helicases
(F) dHJ formation
(G) Class I CO pathway
(H) Class II CO pathway
Crossover
Crossover
Non-crossover

1.8. The NHEJ and TMEJ pathways can also repair DSBs in meiosis

In addition to homologous recombination, other pathways such as NHEJ and TMEJ can repair DSBs in cells (Chang et al., 2017). Proteins involved in these two pathways can be recruited to DSB sites, similar to proteins involved in homologous recombination (Chang et al., 2017). Strand resection is not required for DNA repair via the NHEJ pathway as it is for homologous recombination pathways (i.e. SDSA, class I crossover, and class II crossover). The NHEJ pathway is initiated when Ku70/Ku80 heterodimers are recruited to DSB sites where they protect DNA ends from resection (Ramsden and Geliert, 1998). Subsequently, DNA-PKc (DNA-dependent protein kinase catalytic subunit) (Gottlieb and Jackson, 1993) and DNA polymerases, including polymerase λ (Ramsden, 2011) are recruited to the DSB site. Unlike homologous recombination, a DNA template is not utilized by DNA polymerases to repair the DSB in the NHEJ pathway. Instead, DNA polymerases can stabilize two ends of a DSB and may insert bases at small gaps (Ramsden, 2011). After DNA synthesis is complete, the DNA ends are ligated together via the XLF-XRCC4-DNA ligase IV complex (Ahnesorg et al., 2006; Critchlow et al., 1997; Grawunder et al., 1997).

During meiosis, DSB repair through NHEJ occurs considerably less frequently than homologous recombination (Ahmed et al., 2007; Goedecke et al., 1999). One possible reason for this is that homologous recombination is less error prone than NHEJ, hence reducing the frequency of *de novo* mutations in the germ line (Rodgers and Mcvey, 2016). Specific mechanisms promote DSB repair via homologous recombination during meiosis. In particular, recruitment of the 9-1-1 (RAD9-RAD1-HUS1) complex to DSBs prevents recruitment of the Ku70/Ku80 heterodimer during meiosis in *O.sativa* (Hu et al., 2016). Furthermore in *D. melanogaster,* proteins specific to the homologous recombination pathway accumulate at DSBs and prevent the recruitment

of proteins involved in NHEJ (Joyce et al., 2012). Nevertheless, NHEJ proteins are detected in late pachytene in mammalian meiosis (Goedecke et al., 1999). Notably, the NHEJ pathway can repair DSBs on the X and Y chromosomes in spermatocytes (described in further detail in the next section) (Goedecke et al., 1999). Furthermore, DSBs that are induced late in meiotic prophase (typically in the context of perturbation experiments) are repaired dominantly via the NHEJ pathway (Ahmed et al., 2010; Enguita-Marruedo et al., 2019). Therefore, the NHEJ pathway can be activated later in meiotic prophase to repair any unresolved DSBs. Indeed, the NHEJ pathway can compensate in DSB repair when the homologous recombination pathway is perturbed (Macaisne et al., 2018; Smolikove et al., 2007; Yin and Smolikove, 2013). For the NHEJ pathway to repair DSBs destined for homologous recombination, the ssDNA overhangs may be nucleolytically removed via the Artemis nuclease or the RecQ WRN helicase (Kusumoto et al., 2008; Li and Comai, 2001; Ma et al., 2002). From here, classical NHEJ can proceed to repair DSBs. However, this results in a deletion of genomic DNA since the ssDNA overhangs are removed.

The TMEJ pathway may also repair DSBs in meiosis, particularly when the homologous recombination pathway is perturbed (Macaisne et al., 2018; Martin et al., 2005). TMEJ, or theta mediated end joining, is a type of microhomology-mediated end joining that can be activated following DNA resection by the MRN complex, similar to homologous recombination (Rass et al., 2009; Truong et al., 2013; Xie et al., 2009). However, unlike homologous recombination, extensive strand resection is not required for DNA repair via TMEJ, with microhomologies of approximately two to 22 nucleotides sufficient to stimulate DNA repair (Chang et al., 2017). To repair DSBs via the TMEJ pathway, polymerase θ (theta) oscillates between template-dependent and template-independent activities to extend DNA at the

break site before the DNA ends are ligated by DNA ligase III (Audebert et al., 2004; Black et al., 2016). Polymerase theta can displace RPA and RAD51 from ssDNA, promoting the shift from homologous recombination to TMEJ (Ceccaldi et al., 2015; Mateos-Gomez et al., 2017). Similar to NHEJ, TMEJ may also induce mutations that are deleterious to the germline (Chang et al., 2017).

1.9. XY chromosome biology

As with oocytes, spermatocytes must also generate inter-homolog crossovers between all homologous chromosomes for successful meiosis. However, spermatocytes experience a unique circumstance as the X and Y sex chromosomes are not fully homologous. Therefore, only one inter-homolog crossover can be induced between the X and Y chromosomes at the synapsed homologous PAR sections of the sex chromosomes (Acquaviva et al., 2020). The remaining chromosomal arm regions of the X and Y chromosomes are non-homologous (non-PAR) and thus cannot be synapsed (termed asynapsed). Nevertheless, DSBs are induced along both PAR and non-PAR sections of the X and Y chromosomes (Moens et al., 2002). The DSBs in non-PAR sections are likely repaired through either inter-sister homologous recombination or through the NHEJ pathway, but are excluded from inter-homolog crossover formation (Hoyer-Fender, 2003). In addition, the DSBs in the non-PAR sections are repaired later in pachytene than DSBs on autosomes (Moens et al., 2002). Presumably, this is due to the fact that inter-sister recombination and NHEJ repair are repressed until late pachytene when finally they become active (Goedecke et al., 1999; Sandhu et al., 2020). During mid-pachytene, the presence of asynapsis and unrepaired DSBs on the X and Y chromosomes are detected by cellular machinery (described in further detail in a later section) (Hoyer-Fender, 2003). In an attempt to repair DSBs, the X and Y chromosomes are sequestered into a chromatin domain

called the XY body. Here, the chromatin in both the X and Y chromosomes is remodeled and becomes enriched in histone variants including γH2AX while other histones are modified (including deacetylation of histones H3 and H4) (Fernandez-Capetillo et al., 2003; Khalil et al., 2004). Together, this promotes the transcriptional silencing of the sex chromosomes until DSB repair is complete by the end of pachytene (Royo et al., 2010). The reasons why transcriptional silencing is induced remain unclear however silencing could prevent the expression of meiotic lethal sex-linked genes during pachytene (Cloutier and Turner, 2010). Overall, spermatocytes have developed mechanisms to ensure that DSBs can be repaired along the X and Y chromosomes even in the absence of full synapsis. This ensures that spermatocytes progress through meiotic prophase and into later stages of meiosis to generate sperm.

1.10. From prophase to meiosis II: the generation of haploid gametes

In the next section I will describe how germ cells progress from pachytene of meiotic prophase into later stages of meiosis. Following meiotic prophase, germ cells progress through two successive rounds of meiotic division (meiosis I and meiosis II), with each division reducing the number of chromosomes within a cell by half, leading to the generation of the haploid egg and sperm. The processes that regulate the formation of haploid gametes will now be discussed.

1.10.1. Diplotene to meiosis I

Diplotene is the fourth stage of meiotic prophase, following pachytene. At this stage the repair of DSBs in spermatocytes and oocytes is complete and chiasmata are installed (Moens et al., 2002; Plug et al., 1998). During diplotene, the SC between homologous chromosomes disassembles (Fig.1), remaining only at the centromeric regions of chromosomes until

metaphase I (Bisig et al., 2012; Cahoon and Hawley, 2016). Germ cells next progress into diakinesis, which is the final stage of meiotic prophase. From here, spermatocytes directly proceed into meiosis I, while oocytes enter a prolonged period of cellular quiescence termed dictyate arrest. For mammalian oocytes, dictyate arrest lasts from birth until puberty (Clift and Schuh, 2013). Oocytes may remain in dictyate arrest for months to years in mice, or decades in humans. After puberty, a subset of oocytes are released from dictyate arrest during each ovulatory cycle in order to generate a haploid egg. It is generally considered that a finite pool of oocytes is generated during fetal development that becomes gradually diminished during reproductive life (Horan and Williams, 2017). While several studies suggest that oogonial stem cells could replenish this pool (Sriraman et al., 2015; Wang et al., 2017; Woods et al., 2013), further evidence substantiating this theory is currently lacking. In comparison, haploid sperm are continuously produced in adult mammalian testes due to the presence of spermatogonial stem cells (de Rooij, 2001; Shinohara et al., 2000). These stem cells are derived from PGCs and are detected in testes from postnatal day 2 in mice (McLean et al., 2003; Yoshida et al., 2006). In mice, spermatogonial stem cells differentiate into spermatocytes in an asynchronous manner from approximately postnatal day 20 in mice (Bellve et al., 1977). Spermatocytes then proceed through meiosis to generate a continuous supply of sperm. However, a synchronous wave of male meiosis begins directly from PGCs prior to postnatal day 20 (Kluin et al., 1982; Yoshida et al., 2006). Here, meiotic prophase commences from postnatal day 10, with sperm from this synchronous wave of meiosis produced by postnatal day 30 in mice (Bellve et al., 1977).

1.10.2. Meiosis I to meiosis II

In oocytes and spermatocytes, activation of CDK1 (Cyclin dependent kinase 1)/CyclinB promotes the transition from prophase into meiosis I (Wiltshire et al., 1995). After entry into meiosis I, homologous chromosomes condense and the nuclear envelope breaks down, releasing the chromosomes into the cytoplasm. During metaphase I, the homologous chromosomes align on the meiotic spindle. The spindle is composed of a bipolar assembly of microtubule fibers that bind kinetochores (associated with centromeres) and exert tension forces across the chromosomes (Kitajima, 2018). Here, the chiasmata between homologs play a critical role in resisting spindle forces, enabling the correct segregation of homologous chromosomes during anaphase I (Kitajima, 2018). At the onset of anaphase I, Rec8-containing cohesin complexes are cleaved by the endoproteolytic enzyme, separase, leading to segregation of homologous chromosomes (Kitajima et al., 2003). At the end of meiosis I in females, one set of homologous chromosomes remain within the oocyte while the other set is extruded into the first polar body. For males, the two sets of homologous chromosomes are segregated into two secondary spermatocytes. Following entry into meiosis II, a second meiotic spindle is assembled to segregate the two sets of sister chromatids into two sperm cells. Oocytes only complete meiosis II upon fertilization by sperm (Clift and Schuh, 2013). Following fertilization, the two sets of sister chromatids in the oocyte are segregated, with one set of sister chromatids extruded into the second polar body. Subsequently, the haploid egg and sperm chromosomes form pronuclei that fuse to generate a new diploid organism (Chaigne et al., 2016). Once again, a germ cell lineage will establish in the newly formed embryo and the cycle continues.

1.11. Defects during meiotic prophase activate meiotic checkpoints

During meiotic prophase, an insufficient number of chiasmata may sometimes be installed if errors occur during either homologous chromosome synapsis or homologous recombination. In the majority of cases, defects in either homologous chromosome synapsis or homologous recombination are detected through two key meiotic checkpoints, namely the pachytene checkpoint and the spindle assembly checkpoint. This can delay meiotic progression in an attempt rectify the meiotic defects. If defects cannot be resolved, cells are eliminated via apoptosis. In this final section, the processes involved in activating the pachytene checkpoint and the spindle assembly checkpoint are described. In addition, the consequences of escaping checkpoint activation will be discussed.

1.11.1. The pachytene checkpoint

During prophase, defects during either homologous chromosome synapsis (including pairing and alignment) or homologous recombination can perturb the repair of DSBs and the formation of chiasmata (Dai et al., 2017; Kneitz et al., 2000; Pittman et al., 1998; Shi et al., 2019; De Vries et al., 2005, 1999; Yoshida et al., 1998). These defects can be detected by cellular machinery, leading to the activation of the pachytene checkpoint during mid-pachytene (reviewed in Roeder and Bailis, 2000). Key activators of the pachytene checkpoint are the HORMA domain-containing proteins, HORMAD1 and HORMAD2 (Daniel et al., 2011; Kogo et al., 2012a, 2012b; Wojtasz et al., 2009, 2012). HORMAD1 and HORMAD2 are assembled along chromosome axes during leptotene and are normally removed from axes following synapsis in early pachytene (Wojtasz et al., 2009). The persistence of HORMAD1 and HORMAD2 on chromosome axes during mid-pachytene activates the pachytene checkpoint (Daniel et al., 2011; Kogo et al., 2012a, 2012b; Wojtasz et al., 2009, 2012). As homologous

chromosome synapsis is required to induce inter-homolog crossovers, HORMAD proteins also indirectly signal defects in homologous recombination (Roig et al., 2010). If homologous chromosome synapsis proceeds correctly but homologous recombination is perturbed, proteins involved in the DNA damage checkpoint (RAD24, RAD17, MEC3, DDC1 and MEC1) will activate the pachytene checkpoint (Bailis and Roeder, 2000; Lydall et al., 1996; San-Segundo and Shirleen Roeder, 1999). The activation of the pachytene checkpoint delays progression into later stages of meiosis until DSBs are repaired. While direct evidence is lacking, it is likely that during this delayed period a variety of mechanisms promote DSB repair including inter-sister homologous recombination as well as the NHEJ and TMEJ pathways. However, while these processes can repair persisting DSBs, the germ cell is likely to contain an insufficient number of chiasmata between each pair of homologs. This will have negative consequences on chromosome segregation during meiosis I (described below). Failure to repair DSBs after pachytene delay results in the activation of checkpoint kinases CHK1 and CHK2, which in turn promote cell elimination via p53/p63-dependent apoptosis (Bolcun-Filas et al., 2014; Pacheco et al., 2015; Rinaldi et al., 2017, 2020).

1.11.2. The spindle assembly checkpoint

Germ cells with an insufficient number of chiasmata between homologous chromosomes may progress through meiotic prophase and into meiosis I (Eaker et al., 2002). However, due to the insufficient number of chiasmata, the homologs (also called bivalents) can prematurely separate into univalent chromosomes during meiosis I. Unlike bivalents, univalent chromosomes fail to correctly align on the metaphase I spindle (Sakakibara et al., 2015). Incorrectly aligned chromosomes are detected by the spindle assembly checkpoint during prometaphase I and if not corrected can lead to cell elimination via apoptosis (Eaker et al.,

2001, 2002; Lane and Kauppi, 2019; Lipkin et al., 2002). Though, the spindle assembly checkpoint in mammalian oocytes is often permissible to errors during chromosome alignment and thus, may give rise to chromosome segregation errors (Webster and Schuh, 2017).

1.11.3. Aneuploid embryos can form if germ cells contain insufficient chiasmata

Chromosome segregation errors during meiosis I often arise when meiotic checkpoints fail to eliminate defective germ cells. Occasionally, defective germ cells can escape checkpoint control and proceed past prometaphase I. As described above, if bivalent chromosomes contain an insufficient number of chiasmata, they can separate into univalent chromosomes, which fail to align correctly on the metaphase I spindle (Eaker et al., 2002; Sakakibara et al., 2015). Consequently, chromosome segregation errors can arise during meiosis I. The outcome of these errors often result in an incorrect number of chromosomes in the embryo, termed aneuploidy. In turn, aneuploidy most often leads to spontaneous abortions (miscarriages), or if the embryo survives, severe developmental syndromes such as Down's syndrome (Hassold et al., 2007; Webster and Schuh, 2017).

In summary, the processes of homologous chromosome synapsis (including pairing and alignment) and recombination ensure that chiasmata are installed between homologous chromosomes during meiotic prophase. Chiasmata hold homologs together as bivalents and facilitate the correct segregation of homologous chromosomes during meiosis I. Collectively, these processes lead to the formation of male and female haploid gametes, which together can produce diploid organisms through fertilization.

Chapter 2: Actin, ARP2/3, and nm-myosin IIB facilitate homologous chromosome synapsis and recombination during mammalian meiotic prophase

2.1.0. Introduction

In the second chapter of my dissertation, I present my research uncovering the roles of actin and actin-associated factors in mammalian meiotic prophase. I begin by describing the cellular functions of actin and actin-associated factors and the current knowledge regarding the roles they perform in the nucleus of somatic cells in promoting DSB repair. Following this, I present my experimental results that reveal novel roles for actin, the ARP2/3 complex, and non-muscle myosin IIB in the nucleus of meiotic germ cells where they facilitate homologous chromosome synapsis and recombination. Finally, I discuss how my findings are contextualized by the existing literature regarding nuclear actin and meiotic prophase.

2.1.1. Actin monomers polymerize into filaments

Actin is a highly conserved and abundant protein found in eukaryotic cells (Pollard, 2016). There are three main isoforms of actin in vertebrates, namely α-actin expressed in muscle cell types and the ubiquitously expressed isoforms, β-actin and γ-actin (Perrin and Ervasti, 2010). Monomeric actin can polymerize into filamentous actin, which is a major component of the cytoskeleton. Filamentous actin is dynamically assembled for a range of cellular functions including cell motility and intra-cellular movements of vesicles and organelles (Perrin and Ervasti, 2010). The first step of actin polymerization involves the nucleation of actin monomers into actin dimers and trimers. Actin nucleation is an intrinsically unfavorable process owing to the instability of actin dimer and actin trimer structures (Cooper et al., 1983; Sept and McCammon, 2001). However, addition of a fourth actin monomer to a trimer generates a

stable actin tetrameric oligomer. Additional actin monomers are efficiently added to an oligomer leading to elongation of an actin filament. In cells, a steady state of polymerization and depolymerization is reached when exchange of actin monomers occurs without a change in the total mass of the filament (Pollard, 2016). Actin filaments are polar, containing a fast-growing barbed end and a slow-growing pointed end. ATP-actin monomers are predominately added to the barbed end. Over the lifetime of the actin filament, ATP is hydrolyzed by actin and eventually ADP-actin is disassembled from the pointed end of the filament (Pollard, 2016). The exchange of ADP for ATP leads to the generation of a new ATP-actin monomer that is then ready for further polymerization.

Actin filaments are rapidly assembled from actin monomers to facilitate dynamic cellular processes. To ensure actin polymerization occurs efficiently, the cell employs actin nucleators to assist in the first rate-limiting step of nucleating actin monomers into actin dimers and trimers. The specific functions of these actin nucleators are described in the next section.

2.1.2. ARP2/3, formins, and spire proteins promote actin nucleation to drive polymerization

The ARP2/3 complex, formins, and spire proteins are three types of actin nucleators that stabilize actin dimers and actin trimers to increase the efficiency of actin nucleation in the cell (Fig. 3A) (Goode and Eck, 2007). The ARP2/3 complex is comprised of seven subunits, including the actin-related proteins ARP2 and ARP3 and the ARP2/3 complex subunits ARPC1, ARPC2, ARPC3, ARPC4, and ARPC5 (Robinson et al., 2001). ARP2/3 is activated by members of the Wiskott–Aldrich Syndrome protein (WASP) family (Rotty et al., 2013). In particular, WASP proteins induce a conformational change in the ARP2/3 complex, bringing ARP2 and ARP3 subunits into close proximity (Goley et al., 2004; Rodal et al., 2005). Once associated, ARP2/3

binds the lateral side of a pre-existing actin filament, where the ARP2 and ARP3 subunits interact with an actin monomer to mimic the nucleation of an actin trimer (Dayel and Mullins, 2004; Egile et al., 2005; Rouiller et al., 2008; Volkmann et al., 2001). Through this process, a new actin filament is polymerized at a 70° angle to a pre-existing actin filament (Fig. 3A).

While the ARP2/3 complex promotes the formation of branched actin filaments, formins and spire proteins facilitate the formation of unbranched linear actin filaments (Pollard, 2016). Formin homodimers generate a ring-shaped structure that stabilizes the formation of an actin dimer and thus catalyzes the energetically unfavorable nucleation step (Fig. 3A) (Pring et al., 2003; Xu et al., 2004). Following nucleation, formins remain associated with the barbed end of the actin filament to facilitate further addition of actin monomers to the growing filament (Otomo et al., 2005). Spire contains four WASP homology 2 (WH2) domains that can each associate with one actin monomer (Quinlan et al., 2005; Wellington et al., 1999). Through the WH2 domains, spire proteins can simultaneously associate with four actin monomers to promote the nucleation of a stable actin oligomer (Fig. 3A) (Quinlan et al., 2005; Wellington et al., 1999).

2.1.3. Myosins motor along tracks of actin filaments

Myosins are a superfamily of motor proteins that can translocate along assembled actin filaments through domains that transiently interact with actin. Each myosin molecule is comprised of a stoichiometric arrangement of heavy chains and light chains, depending on the type of myosin (Fig. 3B). Generally, myosin heavy chains contain an amino-terminal globular head domain, a central neck domain, and a carboxy-terminal tail domain (Sellers, 2000). The light chains associate with heavy chains at the neck domain where they regulate the activity

of the myosin molecule (Sellers, 2000). The head domain of a myosin heavy chain can bind and hydrolyze ATP (Rayment et al., 1993). The head domain also interacts with actin filaments, specifically when bound to ADP and P_i (Rayment et al., 1993). The release of ADP and P_i, following actin binding, enables ATP to bind to the head domain (Houdusse and Sweeney, 2016). This induces a conformational change in the head domain, leading to dissociation of the head domain from the actin filament (Dominguez et al., 1998). The neck domain of the heavy chain acts as a lever arm which can displace the head domain along the actin filament (Uyeda et al., 1996). This movement is powered through ATP hydrolysis (Gulick and Rayment, 1997). The cycle repeats when the myosin head then binds a new position along the actin filament leading to the release of ADP and P_i (Houdusse and Sweeney, 2016). Repeated cycles of ATP hydrolysis enable specific myosin classes (e.g. myosin II) to generate tension between actin filaments, while allowing other myosin classes (e.g. myosin I, myosin V, myosin VI, and myosin X) to carry cargo along actin filaments (O'Connell et al., 2007). The specific function of myosin is influenced by the composition of the carboxy terminal tail of the heavy chain (Korn, 2000). The structure and function of tension-generating and cargo-carrying myosins are described in the next section. Experimental evidence presented later in this chapter implicates non-muscle myosin IIB— a tension-generating myosin— in homologous chromosome synapsis and recombination in mammalian germ cells.

2.1.4. Myosin II is a tension-generating myosin

Myosin II molecules are comprised of two heavy chains, two regulatory light chains, and two essential light chains (Fig. 3B) (Sellers, 2000). Each heavy chain contains a long α-helical coiled coil in the tail domain. Anti-parallel dimerization of two myosin II molecules can occur through associations of tail domains (Vicente-Manzanares et al., 2009). In myosin II dimers, the head

domains are oriented in opposing directions, enabling myosin II dimers to associate with two actin filaments simultaneously at either end of the dimer (Fig. 3B). Anti-parallel arrays of multiple myosin II molecules can also assemble through associations of tail domains, generating large bipolar filaments with multiple head domains at opposing poles (Niederman and Pollard, 1975; Svitkina et al., 1995). The essential light chains and regulatory light chains associate with the heavy chains via the neck domain and regulate the stability and activity of myosin II, respectively (Vicente-Manzanares et al., 2009). The regulatory light chains are phosphorylated on serine-19 and threonine-18 by kinases including myosin light chain kinase (Ikebe et al., 1986; Totsukawa et al., 2000). Unphosphorylated myosin II adopts a compact conformation through head-head and head-tail interactions (Burgess et al., 2007; Hyun et al., 2008; Wendt et al., 2001). This impedes the ability of the head domains to interact with actin and hydrolyze ATP. By contrast, phosphorylation of the regulatory light chains disrupts head-head and head-tail interactions, producing an open conformation of 'active' myosin II (Hyun et al., 2008; Ikebe et al., 1988). Activation enables the head domains to interact with actin and exposes the tail domains for bipolar filament assembly (Wendt et al., 2001). The ability of myosin II to form anti-parallel myosin II filaments makes this myosin well suited for generating tension between actin filaments. For example, the simultaneous actions of head domains on either side of a bipolar filament will force two actin filaments to come together. Indeed, myosin II is responsible for generating muscle contractions (Morano et al., 2000) and producing contractile rings during cytokinesis (Bao et al., 2005; Henson et al., 2017; Ma et al., 2012).

Myosin II molecules are subcategorized into muscle myosin II and non-muscle myosin II (nm-myosin II) isoforms. While muscle myosin II isoforms are expressed exclusively in muscle cell

types, nm-myosin II isoforms are expressed in muscle and non-muscle cells (Vicente-Manzanares et al., 2009). There are three mammalian isoforms of nm-myosin II, namely nm-myosin IIA, nm-myosin IIB, and nm-myosin IIC. The heavy chains (HC) of the nm-myosin II isoforms (termed NM-HC) are unique to each isoform and are encoded by different genes (NM-HCIIA encoded by *MYH9;* NM-HCIIB encoded by *MYH10;* and, NM-HCIIC encoded by *MYH14)* (Vicente-Manzanares et al., 2009). Of the different myosin II isoforms, nm-myosin IIB has the slowest rate of ATP hydrolysis and a high affinity for ADP (Kovács et al., 2003; O'Connell et al., 2007; Wang et al., 2003). These properties enable nm-myosin IIB to prolong its association with actin relative to other myosin II isoforms, making nm-myosin IIB well suited to exert tension on actin filaments for long periods of time (Wang et al., 2003).

2.1.5. Cargo-carrying myosin proteins

Other myosin classes including myosin I (Raposo et al., 1999; Salas-Cortes et al., 2005), myosin V (Roland et al., 2007; Swiatecka-Urban et al., 2007), myosin VI (Arden et al., 2007; Buss et al., 1998), and myosin X (Berg and Cheney, 2002; Tokuo and Ikebe, 2004) contain specific domains in their heavy chain tail regions that enable interactions with specific cellular cargo and organelles (Fig. 3B). Similar to other myosins, these myosin classes also contain heavy chain head and neck domains that enable association with actin filaments (Sellers, 2000). While myosin I molecules contain one heavy chain, myosin V, myosin VI, and myosin X molecules contain two heavy chains (Sellers, 2000). Through ATP hydrolysis cycles, the head domains of these myosin classes can transiently associate with actin filaments, enabling them to translocate along actin filaments to move cargo within the cell or to organize cellular structures (Hartman and Spudich, 2012).

Figure 3. Actin, actin nucleators, and myosin motor proteins. Shown on next page. (A) Actin monomers are assembled into filaments through actin polymerization. The ARP2/3 complex, formins, and spire proteins facilitate actin polymerization by nucleating actin monomers through the mechanisms depicted. Note that these processes involve the nucleation of parallel actin dimers. Nucleation of anti-parallel actin dimers into oligomeric actin structures can also occur, although the exact structure of oligomeric actin remains unclear. The ARP2/3 complex is activated by WASP proteins. Activated ARP2/3 associates with the side of a pre-existing actin filament. Association of the ARP2 and ARP3 subunits of ARP2/3 with an actin monomer mimics an actin trimer, stimulating the polymerization of a branched actin filament (at a 70° angle from the original actin filament). Formin homodimers stabilize parallel actin dimers and facilitate further polymerization at assembled actin filaments. Through the WH2 domains, spire proteins interact and organize up to four actin monomers into a stable complex where further actin polymerization can occur. In comparison to the ARP2/3 complex, formins, and spire proteins facilitate the polymerization of unbranched actin filaments. (B) Myosin proteins are comprised of heavy (blue) and light (yellow) chains. Myosin heavy chains contain a head domain, a neck domain, and tail domains. Head domains associate with actin and can hydrolyze ATP. The neck domain interacts with myosin light chains, which in turn regulate myosin activity. The tail can contain different domains that enable the myosin to bind cargo (e.g. myosin I, myosin V, myosin VI, and myosin X) or to assemble into anti-parallel dimers (e.g. myosin II) as shown. Note that anti-parallel myosin II dimers can bind two different actin filaments as depicted.

Figure 3

A

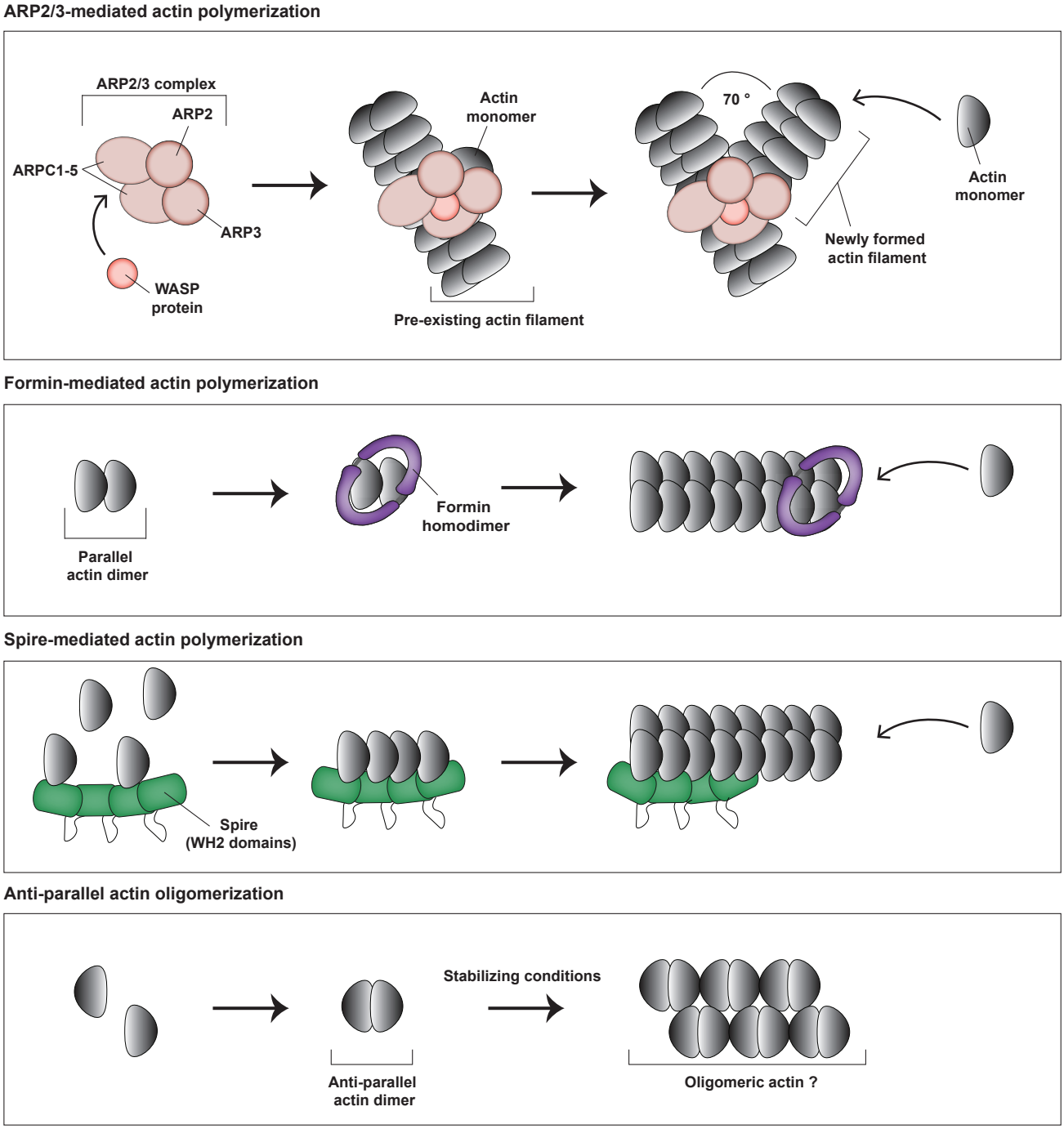
ARP2/3-mediated actin polymerization
ARP2/3 complex
ARP2
ARPC1-5
ARP3
WASP protein
Actin monomer
Pre-existing actin filament
70 °
Actin monomer
Newly formed actin filament
Formin-mediated actin polymerization
Parallel actin dimer
Formin homodimer
Spire-mediated actin polymerization
Spire (WH2 domains)
Anti-parallel actin oligomerization
Stabilizing conditions
Anti-parallel actin dimer
Oligomeric actin ?

B

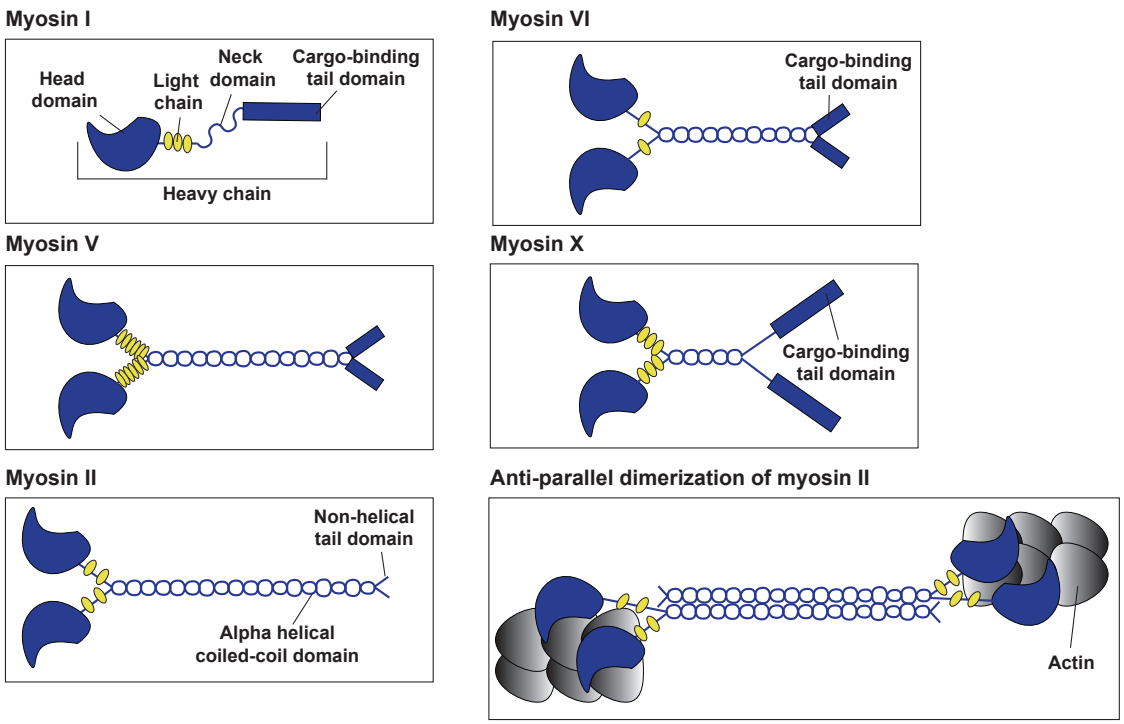
Myosin I
Head domain
Light chain
Neck domain
Cargo-binding tail domain
Heavy chain
Myosin VI
Cargo-binding tail domain
Myosin V
Myosin X
Cargo-binding tail domain
Myosin II
Non-helical tail domain
Alpha helical coiled-coil domain
Anti-parallel dimerization of myosin II
Actin

2.1.6. Actin is a component of the nucleoplasm

Actin is well-established to localize to the nucleus of numerous cell types in different species where it can perform a plethora of roles (Clark and Merriam, 1977; Clattenburg et al., 1972; Gedge et al., 2005; Gonsior et al., 1999; Jockusch et al., 1971; Kelpsch et al., 2016; Lane, 1969; Lessard, 1988; Lestourgeon et al., 1975; Maslova and Krasikova, 2012; Masurovsky et al., 1970; Miranda and Godman, 1973; Parfenov et al., 1995; Ryser, 1970; Scheer et al., 1984; Schoenenberger et al., 2005; Wineland et al., 2018). While actin does not contain nuclear localization sequences (NLS), the actin binding protein cofilin does contain an NLS (Iida et al., 1992; Matsuzaki et al., 1988; Munsie et al., 2012; Vandekerckhove and Weber, 1978). Cofilin is traditionally understood to destabilize filamentous actin to maintain the pool of monomeric actin required for further actin polymerization (Bamburg and Bernstein, 2010). However, actin monomers can also associate with cofilin for importin-9 mediated nuclear import (Dopie et al., 2012; Munsie et al., 2012). While actin isoforms (α-, β-, and γ- actin) do not contain an NLS they do contain nuclear export sequences (NES) (Wada et al., 1998). Through associating with the actin binding protein profilin, actin monomers can be exported from the nucleus via exportin-6 (Stüven et al., 2003). Nucleocytoplasmic transport of actin regulates the levels of actin that are present in the nucleus, which in turn influences the nuclear functions that actin can perform.

2.1.7. Challenges visualizing actin structures inside the nucleus

In the cytoplasm, actin monomers are dynamically assembled into filamentous actin. Cytoplasmic filamentous actin is easily visualized with fluorescently labelled phalloidin. Phalloidin is an actin-binding protein toxin derived from the death cap mushroom, *Amanita phalloides* (Wieland et al., 1978). In the nucleus, actin exists primarily as both monomers and

polymers. Approximately 80% of nuclear actin is monomeric while 20% is in a dynamic polymeric state (McDonald et al., 2006). In contrast to the cytoplasm, filamentous actin structures are typically not detected in the nucleus with fluorescently labelled phalloidin (Kelpsch and Tootle, 2018). However, phalloidin-labelled filamentous actin can be detected in the nucleus in response to cellular stress (e.g. heat-shock, DMSO treatment, and DNA damage) (Caridi et al., 2018; Kelpsch and Tootle, 2018; Sun et al., 2017). Furthermore, filamentous actin is detected in the nucleus when the balance of nucleocytoplasmic transport is altered (Klages-Mundt et al., 2018). Indeed, depolymerization of cytoplasmic actin can increase the fraction of actin monomers that are subsequently imported into the nucleus, resulting in the assembly of filamentous actin within the nucleus (Pendleton et al., 2003). Phalloidin-labelled filamentous nuclear actin structures are also detected in *X.laevis* oocytes, which lack exportin-6 (Stüven et al., 2003). However, expression of exogenous exportin-6 leads to the disassembly of nuclear filamentous actin in *X.laevis* oocytes (Bohnsack et al., 2006). Together this indicates that low levels of nuclear actin are generally prevented from polymerizing into filamentous actin in the nucleus. However, filamentous nuclear actin structures can arise in response to stress stimuli or when the levels of nucleocytoplasmic transport of actin are altered.

In the nucleus, actin polymers take on two forms consisting of oligomers and rods (Kelpsch and Tootle, 2018). The distinction between oligomers and rods currently remains qualitative, with oligomers lacking an obvious filamentous structure, while rods appearing as linear fragments that resemble short cytoplasmic actin filaments (Fukui, 1978; Jockusch et al., 1971; Kelpsch and Tootle, 2018; Lane, 1969; Somosy et al., 1976). Nuclear actin rods can assemble in response to certain stress stimuli, similar to filamentous actin (Fukui, 1978; Iida et al., 1986; Pendleton et al., 2003). However, fluorescently labelled phalloidin binds neither actin rods nor

actin oligomers (Kelpsch and Tootle, 2018; Nishida et al., 1987; Pendleton et al., 2003). Notably, nuclear actin rods are coated with cofilin, which impedes phalloidin binding (McGough et al., 1997; Nishida et al., 1987; Pendleton et al., 2003). Conversely, it is unknown whether actin oligomers bind cofilin, though they do not label with fluorescently labelled phalloidin either (Kelpsch and Tootle, 2018). Overall, it is possible that nuclear actin oligomers are distinct from cytoplasmic filamentous actin, while nuclear actin rods could have a similar structure to filamentous actin, though cofilin occludes visualization using fluorescently labelled phalloidin.

Nuclear actin oligomers (and potentially actin rods) might arise through the oligomerization of anti-parallel actin dimers. During actin polymerization, actin monomers are nucleated into parallel actin dimers before being assembled into filamentous actin (Fig. 3A). In early stages of actin polymerization, anti-parallel actin dimers arise but are rapidly converted into parallel actin dimers (Fig. 3A) (Millonig et al., 1988). However, anti-parallel actin dimers can be stabilized by actin binding proteins (Hesterkamp et al., 1993) and in stabilizing conditions, anti-parallel actin dimers are able to polymerize further into actin oligomers. Anti-parallel actin oligomerization may potentially depend on the ARP2/3 complex (Bubb et al., 2002; Fowler and Aebi, 1982; Qu et al., 2015). Interestingly, nuclear actin structures can be visualized using the monoclonal antibody anti-actin 1C7, which is raised against cross-linked anti-parallel actin dimers (Schoenenberger et al., 2005). In addition, nuclear actin structures are also visualized using the monoclonal antibody, anti-Actin 2G2, which is raised against an actin/profilin complex (Gonsior et al., 1999) but can also bind anti-parallel actin dimers (Schoenenberger et al., 2005). Curiously, anti-Actin 1C7 and anti-Actin 2G2 antibodies label distinct actin structures in the nucleus, suggesting the presence of different pools of nuclear actin

(Schoenenberger et al., 2005; Wineland et al., 2018). Another monoclonal anti-Actin antibody, C4, is raised against chicken gizzard actin and labels similar nuclear actin structures as anti-Actin 2G2 (Lessard, 1988; Schoenenberger et al., 2005). Anti-Actin C4 recognizes α-, β-, and γ-actin, and has been most widely used to visualize nuclear actin, with nuclear actin structures detected in somatic (Gedge et al., 2005; Lessard, 1988; Schoenenberger et al., 2005) and non-mammalian meiotic cells (Kelpsch et al., 2016; Lane, 1969; Maslova and Krasikova, 2012; Parfenov et al., 1995; Scheer et al., 1984; Wineland et al., 2018).

In summary, actin monomers assemble into polymeric structures in the nucleus that may differ to filamentous actin ubiquitously present within the cytoplasm of cells. The formation of polymeric actin structures in the nucleus is regulated through the nucleocytoplasmic transport of actin. Monomeric and polymeric actin in the nucleus can be labelled with anti-actin antibodies, but not with fluorescently labelled phalloidin. Visualization of nuclear actin enables its functions to be explored through microscopy and other experimental methods.

2.1.8. Myosins and nucleators of polymeric actin are present inside of the nucleus

The ARP2/3 complex, formins, and spire proteins localize to the nucleus of cells where they facilitate the formation of actin polymers (Aymard et al., 2017; Baarlink et al., 2013; Belin et al., 2015; Caridi et al., 2018; Schrank et al., 2018). Numerous myosins including myosin I, myosin II, myosin V, myosin VI, and myosin X are also present in the nucleus where they contribute in various nuclear actin functions (De Lanerolle, 2012). A specific isoform of myosin I, termed myosin Iβ, is detected in the nucleus of somatic cells (Nowak et al., 1997). Myosin Iβ has an extended amino terminal which contains NLS-like sequence motifs (Nowak et al., 1997; Pestic-Dragovich et al., 2000). Importins may facilitate the nuclear import of myosin Iβ,

however passive diffusion of myosin Iβ has also been reported (Nevzorov et al., 2018). In addition, the nucleocytoplasmic transport of the formin mDia2 is regulated by Importin-α/β and Crm1 (Miki et al., 2009). Currently, it is unclear how other myosins and actin nucleators translocate into the nucleus.

2.1.9. Actin, actin nucleators, and myosins facilitate DSB repair in somatic cells

Actin, alongside actin nucleators and myosins, are implicated in regulating transcription, chromatin organization, chromatin movement, and maintaining the nuclear structure in both somatic and non-mammalian meiotic cells (reviewed in Kelpsch and Tootle, 2018; De Lanerolle, 2012). In somatic cells (of *Drosophila*, mouse, and human) actin and actin-associated proteins also facilitate the repair of DNA DSBs (Andrin et al., 2012; Aymard et al., 2017; Belin et al., 2015; Caridi et al., 2018; Galarneau et al., 2000; Ikura et al., 2000; Kapoor et al., 2013; Schrank et al., 2018; Tosi et al., 2013). Specifically, monomeric actin is a component of several chromatin remodeling complexes that promote the repair of DNA DSBs (Klages-Mundt et al., 2018). Chromatin-remodeling complexes alter the accessibility of local DNA regions by modifying the composition of histone complexes. This in turn modulates the recruitment of proteins involved in transcription and DSB repair (Clapier and Cairns, 2009). Actin and the actin-related protein, ARP4, are both components of the NuA4 histone acetyltransferase complex (Galarneau et al., 2000; Ikura et al., 2000). Here, ARP4 associates with γH2AX and recruits NuA4 to DSBs where it can acetylate histone 4 (Bird et al., 2002; Downs et al., 2004). Histone 4 acetylation prevents the recruitment of 53BP1 and RAP80 to DSB sites, enabling DNA strand resection to occur— a preliminary step required for homologous recombination (described in further detail in chapter 1) (Hejna et al., 2008; Renaud et al., 2016). Actin and ARP4 are also components of the chromatin remodeling INO80

complex (Kapoor et al., 2013; Tosi et al., 2013). Both INO80 and NuA4 facilitate DSB repair through promoting transcription of DSB repair proteins (Park et al., 2010; Su et al., 2017). Interestingly, the expression of non-polymerizable actin or actin depolymerizing drug treatments impair DSB repair in somatic cells (Andrin et al., 2012; Schrank et al., 2018). Alongside other studies (Belin et al., 2013, 2015), these findings indicate that both monomeric and polymeric actin facilitates DSB repair in somatic cells.

Polymeric actin is assembled at DSB sites by either the ARP2/3 complex or through the combined functions of formins and spire proteins (Aymard et al., 2017; Belin et al., 2015; Caridi et al., 2018; Schrank et al., 2018). Actin polymers can facilitate DSB repair by clustering damaged chromosomal regions together, a process that is thought to locally concentrate DSB signaling and repair proteins to ensure efficient DSB repair (Aymard et al., 2017; Chiolo et al., 2013; Schrank et al., 2018). The specific actin nucleator employed to generate actin polymers can also influence how the DSB will be repaired. In somatic cells, DSBs are typically repaired through either homologous recombination or NHEJ (Hartlerode and Scully, 2009). ARP2/3 nucleated actin polymers promote repair of DSBs by homologous recombination through facilitating the process of DNA strand resection (Schrank et al., 2018). In contrast, actin polymers nucleated by formins and spire proteins promote repair of DSBs by NHEJ (Aymard et al., 2017; Belin et al., 2015), through mechanisms that currently remain unclear.

Polymeric actin can also promote DSB repair through relocating chromosomes with DSBs to the nuclear periphery where homologous recombination may proceed (Caridi et al., 2018). In particular, this process is utilized to repair DSBs at pericentromeric chromosomal regions (Caridi et al., 2018). Such chromosomal regions contain repetitive DNA sequences that are

generally conserved between different chromosomes (Miyanari et al., 2013). Through moving damaged pericentromeric DNA away from other pericentromeric chromosomal regions, invasion of the correct DNA template occurs and ensures the fidelity of chromosome repair through homologous recombination (described in further detail in chapter 1) (Caridi et al., 2018). Relocation of chromosomes with DSBs to the periphery is achieved in an ARP2/3- and myosin-dependent manner (Caridi et al., 2018). Specifically, ARP2/3 nucleates actin polymers at pericentromeric DSBs (Caridi et al., 2018). Subsequently, myosin IA, myosin IB, and myosin V interact with the DSB and translocate the damaged chromosomal region along actin polymers towards the nuclear periphery where homologous recombination events can proceed (Caridi et al., 2018).

Overall, these studies reveal that both actin monomers and polymers assist in the repair of DNA DSBs in somatic cells. Polymeric actin promotes DSB repair through facilitating events involved in either homologous recombination or NHEJ. Actin polymers nucleated by formins and spire proteins promote DNA repair through NHEJ. In contrast, ARP2/3 nucleated actin polymers promote DNA repair through homologous recombination. In particular, ARP2/3 nucleated actin polymers can promote DNA strand resection. Actin polymers nucleated by ARP2/3, with the aid of nuclear-imported myosins, can also relocate chromosomes with DSBs to the nuclear periphery where the correct DNA template is utilized for repair.

2.1.10. Aim of the study

During meiotic prophase, SPO11-induced DSBs are predominantly repaired through the homologous recombination pathway (Lam and Keeney, 2015). Homologous chromosomes are preferentially utilized as the template for DNA repair instead of sister chromatids (described

in further detail in chapter 1) (Lam and Keeney, 2015; Schwacha and Kleckner, 1997). Homologous recombination leads to the production of inter-homolog crossovers (that later mature into chiasmata), which hold maternal and paternal homologous chromosomes together as bivalents to facilitate efficient homolog segregation later in meiosis I (Hassold et al., 2007). The involvement of actin, the ARP2/3 complex, and myosins in somatic homologous recombination (Caridi et al., 2018; Schrank et al., 2018), suggests the possibility that actin-dependent mechanisms might also facilitate homologous recombination during meiotic prophase. Whether actin components are present in the nucleus during mammalian meiotic prophase remained unclear. If actin components do localize to the nucleus during meiotic prophase, I hypothesized that they may facilitate homologous recombination at homologous recombination nodules (HR nodules) located along chromosome axes. In addition, nuclear actin polymers might assist in the pairing, alignment, and synapsis of homologous chromosomes. This actin-dependent process would ensure that homologous chromosomes (and not sister chromatids) are preferentially used as a template during homologous recombination.

In this section of my dissertation, I present data that demonstrates actin, the ARP2/3 complex, and nm-myosin IIB are present within the nucleus during mammalian meiotic prophase. Following this, I examine the function that these nuclear actin components perform in facilitating homologous recombination during meiotic prophase.

2.2.0. Experimental Procedures

2.2.1. Animals

All mice were maintained in a specific pathogen-free environment according to animal ethics guidelines of the animal facility of the Max Planck Institute for Biophysical Chemistry. Animals were sacrificed by cervical dislocation with the guidelines provided by the German Animal Welfare Act (German Ministry of Agriculture, Health, and Economic Cooperation). Testes were isolated from 9 to 17 days old CD1 and B6N male pups and 21 to 56 days old CD1 male mice. Live animal experiments were approved by the Lower Saxony State Office for Consumer Protection and Food Safety (LAVES) (NTP-ID 00033336-2-0).

2.2.2. Plasmid preparation

Plasmids were isolated for electroporation using a DNA plasmid maxi kit (Qiagen, 12163) and solubilized in double-distilled water to generate 5 µg/µl DNA solutions. Testes were injected with the following plasmids: pCMV-Arpc2-mClover, pCMV-NLS-mClover-Myh10, and pCMV-Actin-chromobody-TAGGFP2-NLS (Chromotek, ACG-N). cDNA sequences for *Arpc2* (NM 029711) and *Myh10* (NM 175260) were derived from the NCBI37/mm9 mouse genome sequence. cDNA sequences were amplified from cDNA libraries produced from CD1 mouse testes (as described in table 1 and table 2). In brief, RNA was extracted from testes using TRIzol reagent (Thermofisher, 15596026) according to the manufacturer's instructions. cDNA synthesis was conducted using SuperScript IV (Thermofisher, 18091050) and Oligo d(T)s according to the manufacturer's instructions. *Arpc2* and *Myh10* cDNA were cloned into pENTR-D-TOPO plasmids using directional topoisomerase reactions (Invitrogen, K2400-20). pCMV-Arpc2-mClover and pCMV-NLS-mClover-Myh10 were produced through LR clonase II reactions (Invitrogen, 11791-020) between appropriate pENTR plasmids and Gateway-

Destination plasmids, according to the manufacturer's instructions (as described in table 1 and table 2). PCR amplifications were performed using Phusion HF polymerase (NEB, M0530S) according to manufacturer's instructions. Restriction digests and ligation reactions (NEB, M2200S) were performed according to manufacturer's instructions.

Table 1: List of plasmids generated.

Plasmid type	Plasmid name	Cloning method	Insert vector
Gateway plasmid	pCMV-NLS-mClover	PCR, restriction digest (NheI and AscI), and ligation	pSNAPf (NEB, N9183S)
Gateway plasmid	pCMV-NLS-mClover-Gateway	PCR, restriction digest (AgeI and XhoI), and ligation	pCMV-NLS-mClover
Gateway plasmid	pCMV-Gateway-mClover	PCR, restriction digest (AvrII and PacI), and ligation	pSNAPf (NEB, N9183S)
pENTR plasmid	pENTR-Myh10	PCR, TOPO reaction	pENTR D-TOPO
pENTR plasmid	pENTR-Arpc2	PCR, TOPO reaction	pENTR D-TOPO
Expression plasmid	pCMV-Arpc2-mClover	LR clonase II reaction	pCMV-Gateway-mClover
Expression plasmid	pCMV-NLS-mClover-Myh10	LR clonase II reaction	pCMV-NLS-mClover-Gateway

Table 2: List of primers. The DNA sequence amplified is highlighted in bold.

Cloning step	Forward primer	Reverse primer
pCMV-**NLS-mClover**	GACTGCTAGCCCAAAAAAGAAGAGAAAGGTAGATCCAAAGATGGTGAGCAAGGGCGAGG	GACTGGCGCGCCCTTGTACAGCTCGTCCATGCCATG
pCMV-NLS-mClover-**Gateway**	GACTACCGGTACAAGTTTGTACAAAAAA GCTGAACGAGAAACG	GACTCTCGAGACCACTTTGTACAAGAAAGCTGAACGAGAA
pCMV-**Gateway-mClover**	GACTTTAATTAAACAAGTTTGTACAAAAAA GCTGAACGAGAAACG	ACTGCCTAGGCTACTTGTACAGCTCGTCCATGCC
pENTR-**Myh10**	CACCATGGCCCAGAGAACTGGACTG	CTATTCTGATTGGGGTGGCTGTGTG
pENTR-**Arpc2**	CACCATGATCCTGCTGGAGGTGAACAACCG	GCGGGATGAAAAAGTCTTCCCCGTGA

2.2.3. Electroporation of mouse testes

DNA injection and electroporation of mouse testes was conducted according to the protocol by Shibuya and Watanabe (2018) with minor modifications. 12 or 16 days old B6N male pups were anesthetized using Isoflurane gas (CP-Pharma, 1214) and a subcutaneous injection of 0.05 mg/kg buprenovet (Bayer). The testes of anesthetized mice were pulled out of the abdominal cavity and 5 µl of DNA solution (4.5 µl of 5 µg/µl plasmid and 0.5 µl of 0.1% (w/v) FastGREEN (Sigma; F7258)) was injected into the rete testis using a glass capillary (Clark electromedical instruments, GC120-15) controlled by mouth pipette. Glass capillaries were pulled (Narishige, PC-10 puller) and manually cut to obtain a sharpness of 0.05 to 0.1 mm. One hour after DNA injection, testes were electroporated using tweezer-type electrodes (BEX, LF650P3). Electric pulses were applied four times in one direction and four times in the reverse direction at 30 V for 50 ms with 950 ms intervals per pulse using an electroporator (BEX, CUY 21 EDIT-TYPE). Testes were returned to the abdominal cavity and abdominal wall and skin was sutured closed. 24 hours after electroporation, mice were sacrificed by cervical dislocation and immunostaining was performed.

2.2.4. Preparation and culture of mouse testes

Testes were prepared and cultured according to Sato et al. (2013). In brief, testes were cultured in MEMα (Thermofisher, 22571-020) supplemented with 10% (v/v) Knockout serum replacement (Thermofisher, 10828010) and 1% penicillin-streptomycin (Gibco, 15140122). Testes from 11 days old CD1 pups were decapsulated and each testis was cut into 2 pieces using forceps. Testis pieces were cultured on beds made of agarose. To make agarose beds, 1.5% (w/v) agarose was dissolved in distilled water and the solution was poured into 10 cm dishes. Solid agarose gels were cut into squares (approximately 10 mm x 10 mm) and were

soaked in culture media at 37°C overnight to replace the water with media. Three agarose beds were placed in a 35 mm culture plate. Each agarose bed was loaded with two testis pieces. Media was added to plates until it reached half the height of the agarose beds. Testes were cultured at 34°C with 5% carbon dioxide in air. Testes from 11 days old CD1 male pups were cultured for one day to obtain zygotene cells, three days to obtain early pachytene cells, and five or six days to obtain late pachytene cells. Culture media was changed every two days. All drugs were reconstituted in DMSO (Sigma, D2650). Cytochalasin-D (10 µM final concentration. Sigma, C8273) was added to culture media to inhibit actin polymerization. CK-666 (200 µM final concentration. Calbiochem, 182515) was added to inhibit the activity of the ARP2/3 complex. ML-7 (30 µM final concentration. Merck, 475880) was added to inhibit the activation of nm-myosin IIB. For control experiments, a volume of DMSO equal to the volume of drug was added to the culture media. To induce progression of spermatocytes to metaphase I, testes from 11 day old CD1 pups were cultured for 6 days in the presence of Cytochalasin-D, CK-666, ML-7, or, DMSO. On day 6, testis tubules were minced and single cell suspensions were produced using 35 µm cell strainers (Corning, 352235). Cells were centrifuged at 500 × *g* for 10 minutes at room temperature and re-suspended in culture media (MEMα media, 10% knockout serum replacement and 1% penicillin-streptomycin) supplemented with 5 µM Okadaic acid (Tocris, 1136). Cells were cultured for 5 hours at 34°C with 5% carbon dioxide in air before chromosome spreads were produced.

2.2.5. Preparation and immunofluorescence of fixed intact spermatocytes

Testes were decapsulated and isolated tubules were minced in 1 × phosphate-buffered saline (PBS) to produce a cell suspension. Cells were passed through a 35 µm strainer (Corning, 352235) before centrifugation at 500 × *g* for 10 minutes at 4*°C.* Pelleted cells were re-

suspended in 1 × PBS and added to glass-bottom dishes (Thermofisher, 155411) coated with 0.01% (v/v) poly-L-lysine (Sigma, P8920) and incubated for 5 minutes at room temperature. Cells were fixed in fixative solution at 37°C for 30 minutes. Fixative solution contained 100 mM HEPES (pH 7.0), 50 mM EGTA (pH 7.0), 10 mM magnesium sulfate, 2% (v/v) methanol-free formaldehyde (Polysciences, 04018-1), and 0.2% (v/v) triton X-100 (Sigma, 93443) in distilled water. Fixed cells were permeabilized in 0.1% (v/v) triton X-100 in 1 × PBS (PBT) overnight at 4°C. To block unreacted aldehydes (contribute to background fluorescence) cells were incubated with a quenching solution (75 mM glycine and 50 mM ammonium chloride in 1 × PBS) for 15 minutes at room temperature. Cells were washed with 1 × PBS and blocked for 30 minutes at room temperature in 5% (w/v) milk / PBT. For labelling phosphorylated antigens, 5% (w/v) BSA / PBT was used. Primary and secondary antibody solutions were prepared in blocking buffer and centrifuged at 16,000 × *g* for 30 minutes at 4°C to remove antibody aggregates (contribute to background fluorescence). Cells were incubated with the primary antibody solution for 1 hour at room temperature. Cells were washed in PBT three times and re-blocked in appropriate blocking solution for 30 minutes at room temperature. Cells were incubated with secondary antibody solution for 1 hour at room temperature and then with Hoechst solution (1:333 final concentration. Thermofisher, 62249) for 15 minutes at room temperature. Where indicated, Alexa Fluor-488 Phalloidin (1:20 final concentration. Thermofisher, A12379) was added to the secondary antibody incubation step. Cells were washed in PBT three times. 50% (v/v) glycerol in distilled water was added to cells as a mounting medium for imaging.

2.2.6. Preparation and immunofluorescence of spread spermatocytes

Prophase spermatocyte spreads were prepared according to de Boer et al. (2009). Testes were decapsulated and isolated tubules were cut into pieces in 1 × PBS before being placed in hypotonic buffer for 30 minutes on ice. Hypotonic buffer contained 30 mM Tris-HCL, 17 mM trisodium citrate, 5 mM EDTA, 50 mM sucrose and 5 mM DTT in distilled water (pH 8.2). Tubules were minced in 100 mM sucrose solution and fixed onto slides (Thermofisher, J4800AMNZ) in 1% (v/v) methanol-free formaldehyde solution containing 0.15% (v/v) triton X-100 over a period of three hours in a humidified chamber. Metaphase I spermatocyte spreads were prepared from cell suspensions according to de Boer et al. (2009). Cell suspensions were re-suspended in 1 × PBS to obtain no more than 3 x 10^7 cells/ml. An equal volume of hypotonic buffer (30 mM Tris-HCL, 17 mM trisodium citrate, 5 mM EDTA, 50 mM sucrose and 5 mM DTT in distilled water, pH 8.2) was added and cells were incubated for 30 minutes at room temperature. 100 mM sucrose solution was added (equal to the total volume) and cells were fixed onto slides (Thermofisher, J4800AMNZ) in 1% (v/v) methanol-free formaldehyde solution containing 0.15% (v/v) triton X-100 over a period of three hours in a humidified chamber. For immunostaining, prophase and metaphase I slides were washed in distilled water and then in 0.4% (v/v) photoflo (Kodak, 1464510). Slides were blocked for 30 minutes at room temperature in 5% (w/v) milk / 1 × PBS. Primary and secondary antibody solutions were prepared in blocking buffer and centrifuged at 16,000 × *g* for 30 minutes at 4°C to remove antibody aggregates. Slides were incubated with primary antibody solution for 1 hour at room temperature. Slides were washed in 1 × PBS three times and re-blocked for 30 minutes at room temperature. Slides were incubated with secondary antibody solution for 30 minutes at room temperature and then with Hoechst solution (1:333 final concentration. Thermofisher, 62249) for 15 minutes at room temperature. Slides were washed in 1 × PBS

three times. 50% (v/v) glycerol in distilled water was added to slides before addition of coverslips (#1.5, VWR, 15165452).

2.2.7. Antibodies

Primary antibodies (listed in table 3) and secondary antibodies (listed in table 4) were used in immunofluorescence experiments using fixed and spread spermatocytes.

Table 3: List of primary antibodies used in immunofluorescence studies.

Antibody	Host specie	Antibody dilution	Source
Anti-SYCP3	Guinea pig	1:300	-Kindly provided by Ricardo Benavente -Produced by Cambridge Research Biochemicals using peptide sequence: GGRKHSGKSGKP
Anti-SYCP3	Rabbit	1:300	Novus; N300-231
Anti-SYCP3	Mouse	1:300	Abcam; Ab97672
Anti-SYCP1	Rabbit	1:200	Abcam; Ab15090
Anti-γH2AX	Mouse	1:100	Millipore; 05-636
Anti-RAD51	Rabbit	1:100	Millipore; PC130
Anti-DMC1	Mouse	1:100	Abcam; Ab11054
Anti-RPA32	Rat	1:100	Cell signaling; 2208S
Anti-MLH1	Mouse	1:100	BD Bioscience; 51-1327GR
Anti-MSH4	Rabbit	1:100	Abcam; Ab58666
Anti-KU70	Rabbit	1:100	Abcam; Ab92450
Anti-Polymerase θ	Mouse	1:100	Novus; H00010721-M09
Anti-BLM	Rabbit	1:100	Abcam; Ab2179
Anti-ERCC1	Rabbit	1:100	Abcam; Ab129267
Anti-MUS81	Mouse	1:100	Abcam; Ab14387
Anti-XPA	Mouse	1:100	Santa-Cruz; Sc-28353
Anti-ARPC2	Rabbit	1:100	Millipore; 07-227
Anti-Actin C4	Mouse	1:100	Millipore; MAB1501
Anti-Actin 2G2	Mouse	1:50	Millipore; MABT826
Anti-Actin 1C7	Mouse	1:100	BS Antibody Facility; 1C7
Anti-MYH10	Rabbit	1:100	Covance/Biolegend; PRB-445P
Anti-MYH9	Rabbit	1:100	Covance/Biolegend; PRB-440P
Anti-Myosin Iβ	Rabbit	1:100	Sigma; M3567
Anti-Myosin VI	Rabbit	1:100	Merck; ABT42
Anti-Myosin VA	Rabbit	1:100	Cell signaling; 3402
Anti-Myosin VB	Rabbit	1:100	Abcam; Ab58766

Anti-Myosin X	Goat	1:100	Santa-Cruz; Sc-23137
Anti-Rec8	Rabbit	1:150	Produced by Cambridge Research Biochemicals using Rec8 N-terminal peptide (aa1-263)
Anti-GFP	Rabbit	1:100	Abcam; Ab6556
Anti-mCherry	Goat	1:100	OriGene; AB0081-200

Table 4: List of secondary antibodies used in immunofluorescence studies.

Antibody	Host specie	Antibody dilution	Source
Donkey anti-Rabbit Alexa Fluor 488	Donkey	1:400 (intact cells); 1:250 (spreads)	Invitrogen; A21206
Donkey anti-Rabbit Alexa Fluor 568	Donkey	1:400 (intact cells); 1:250 (spreads)	Invitrogen; A10042
Donkey anti-Rabbit Alexa Fluor 647	Donkey	1:400 (intact cells); 1:250 (spreads)	Invitrogen; A31573
Donkey anti-Mouse Alexa Fluor 488	Donkey	1:400 (intact cells); 1:250 (spreads)	Invitrogen; A21202
Donkey anti-Mouse Alexa Fluor 568	Donkey	1:400 (intact cells); 1:250 (spreads)	Invitrogen; A10037
Donkey anti-Mouse Alexa Fluor 647	Donkey	1:400 (intact cells); 1:250 (spreads)	Invitrogen; A31571
Donkey anti-Rat Alexa Fluor 488	Donkey	1:400 (intact cells); 1:250 (spreads)	Invitrogen; A21208
Goat anti-Guinea pig Alexa Fluor 568	Goat	1:400 (intact cells); 1:250 (spreads)	Invitrogen; A11075
Donkey anti-Goat Alexa Fluor 488	Donkey	1:400 (intact cells); 1:250 (spreads)	Invitrogen; A11055
Donkey anti-Goat Alexa Fluor 568	Donkey	1:400 (intact cells)	Invitrogen; A11057
Chicken anti-Rat Alexa Fluor 647	Chicken	1:400 (intact cells)	Invitrogen; A21472

2.2.8. Microscopy

Images were acquired with LSM 880, LSM 800, and LSM 900 confocal laser scanning microscopes (Zeiss) with a 63 × Plan-Apochromat 1.4 N/A oil-immersion objective. Images of control and experimental groups were acquired under identical imaging conditions on the same microscope. Airyscan images were acquired using the Airyscan module on the LSM800, LSM880, and LSM900 confocal laser scanning microscopes (Zeiss) and processed in ZEN (Zeiss) after acquisition. Care was taken that the imaging conditions (laser power, pixel-dwell time,

and detector gain) did not cause photobleaching or saturation. Intact cells were imaged using Z-stacks at 0.3 µm distance to image entire spermatocyte nuclei (approximately 55 slices).

2.2.9. Definition of meiotic stages

The stage of meiosis was determined by the morphology of the chromosome axes (visualized using either anti-SYCP3 or anti-SYCP1 antibodies) as described in Moens et al. (2002). Leptotene stage was defined by short chromosomal axes that were SYCP3 positive and SYCP1 negative. Zygotene stage was defined by longer chromosome axes that were either single (unaligned), forked (partially aligned) or double (fully aligned). Here, the chromosome axes were SYCP3 positive and at aligned regions of chromosome axes, SYCP1 positive. Pachytene stage was defined by long fully synapsed chromosomal axes that were both SYCP3 and SYCP1 positive. Here, the X and Y chromosomes were fully synapsed with SYCP1 detected at the PAR of the sex chromosomes. Late pachytene stage was defined if the XY body was detected (visualized as a dense Hoechst stained region around the sex chromosomes). Diplotene stage was defined when chromosome axes were separated (SYCP3 positive and segmentally SYCP1 positive) and the XY body was visible. Diakinesis stage was defined when the chromosome axes were further separated (segmentally both SYCP3 and SYCP1 positive). Metaphase I stage was defined by fully condensed homologous chromosome sets and the presence of the synaptonemal complex at the centromere region only.

2.2.10. Measurements of foci number and association along chromosome axes

Quantifications of both the number of foci and association of foci along chromosome axes were collected using Imaris (Bitplane) software. Chromosome axes were segmented using the surface function of Imaris and all channels were masked to specifically analyze foci along the

chromosome axes. Imaging channels that were used to visualize actin components (actin, the ARP2/3 complex, or nm-myosin IIB) or proteins involved in DSB repair were then segmented using the surface function. Quantifications of the number of surfaces along chromosome axes were collected for further analysis. Association was defined when a focus was either engulfed by another focus or when two foci were partially overlapping together. Quantifications of foci association were collected by manually counting the number of associations along chromosome axes.

2.2.11. Measurements of foci association at different axis morphologies

The association of actin components (actin, the ARP2/3 complex, or nm-myosin IIB) with RPA at single, forked or double chromosome axes was analyzed in zygotene spermatocytes using Fiji (Image J). The morphology of the chromosome axis was visualized using anti-SYCP3. Careful manual analysis was conducted to categorize the axis as single (unaligned chromosome axis), forked (the point where the homologous chromosome axes are aligning) or double (aligned homologous chromosome axes). The morphology of the chromosome axis was recorded where an actin component (actin, the ARP2/3 complex, or nm-myosin IIB) associated with an RPA focus (either engulfed by an RPA focus or partially overlapping with an RPA focus). These quantifications were manually recorded either across a single Z position for chromosome spreads or multiple Z positions for intact spermatocytes (approximately 55 Z positions per spermatocyte).

2.2.12. Statistical analysis

Statistical analyzes were performed using OriginPro or GraphPad. Statistical significance was based on either unpaired, two-tailed Student’s t test or two-tailed Fisher’s exact test.

2.3.0. Results

2.3.1. Actin and the ARP2/3 complex localize to chromosome axes during meiotic prophase

I first investigated whether actin and the ARP2/3 complex are present in the nucleus during mammalian meiosis. To this end, fixed murine spermatocytes were labelled with antibodies specific for actin and ARP2/3. Interestingly, foci of both actin and ARP2/3 are detected in the nucleus during meiotic prophase (Fig. 4A, 4B). In accordance with previous studies (Nishida et al., 1987; Pendleton et al., 2003), nuclear actin structures are not detected with fluorescently labelled phalloidin (Fig. 5D). Instead nuclear actin is detected only when labelled with antibodies specific for monomeric and polymeric actin structures, namely, anti-Actin C4 (Fig. 5A), anti-Actin 2G2 (Fig. 5B), and anti-Actin 1C7 (Fig. 5C). From here on, the anti-Actin C4 antibody was utilized to visualize nuclear actin in spermatocytes.

During meiosis, DSBs are relocated to chromosome axes for repair via homologous recombination (Lam and Keeney, 2015). My results indicate that foci of both actin and ARP2/3 are identified along chromosome axes marked by SYCP3 (Fig. 4A, 4B). This suggests that actin and ARP2/3 localize to the same nuclear regions where homologous recombination occurs. Actin and ARP2/3 differ in the number of foci detected along chromosome axes during different stages of prophase (Fig. 4D). While a mean of 123.5 actin foci per cell are detected between leptotene and diplotene, the number of ARP2/3 foci fluctuates during prophase, starting from 60.8 foci in leptotene, and rising to 112.8 during pachytene before declining to 34.8 foci per cell in diplotene (Fig. 4D). This reveals that actin associates with chromosome axes for a large duration of meiotic prophase, while ARP2/3 is only transiently associated with chromosome axes.

Figure 4: Actin, ARP2/3, and nm-myosin IIB localize with RPA foci. Shown on next page. (A-C) Representative images of actin (A), ARP2/3 (B), and nm-myosin IIB (C) with RPA during different stages of meiotic prophase. Central Z positions of spermatocytes are shown. Circles highlight spermatocyte nuclei. Scale bars, 2 µm. (D) Quantification of actin, ARP2/3, and nm-myosin IIB foci number along chromosome axes per cell during different meiotic prophase stages. Mean (square), median (line), 25^{th} and 75^{th} quartiles (boxes) are shown along with the standard deviation for two experimental replicates. The approximate (approx.) trends in mean foci number of actin, ARP2/3, and nm-myosin IIB along chromosome axes during meiotic prophase are depicted in the bottom panel. E) Quantification of the amount of actin components associated with RPA foci along chromosome axes per cell during meiotic prophase. Two experimental replicates are shown. (F) Quantification of the amount of RPA foci associated with actin components along chromosome axes per cell during meiotic prophase. Two experimental replicates are shown. (G) Quantification of the amount of RPA foci associated with exogenously expressed (ex) fluorescently labelled actin components along chromosome axes per cell during meiotic prophase. One experimental replicate is shown. (H-I) Quantifications of the amount of actin foci associated with either ARP2/3 (H) or nm-myosin IIB (I) along chromosome axes per cell during meiotic prophase. Two experimental replicates are shown. Mean and median lines are shown along with the standard deviation for graphs (E-I). All P-values are calculated using two-sided Student's t-test. n.s., not significant. n is the number of spermatocytes analyzed. Chr. is an abbreviation of chromosome.

Figure 4

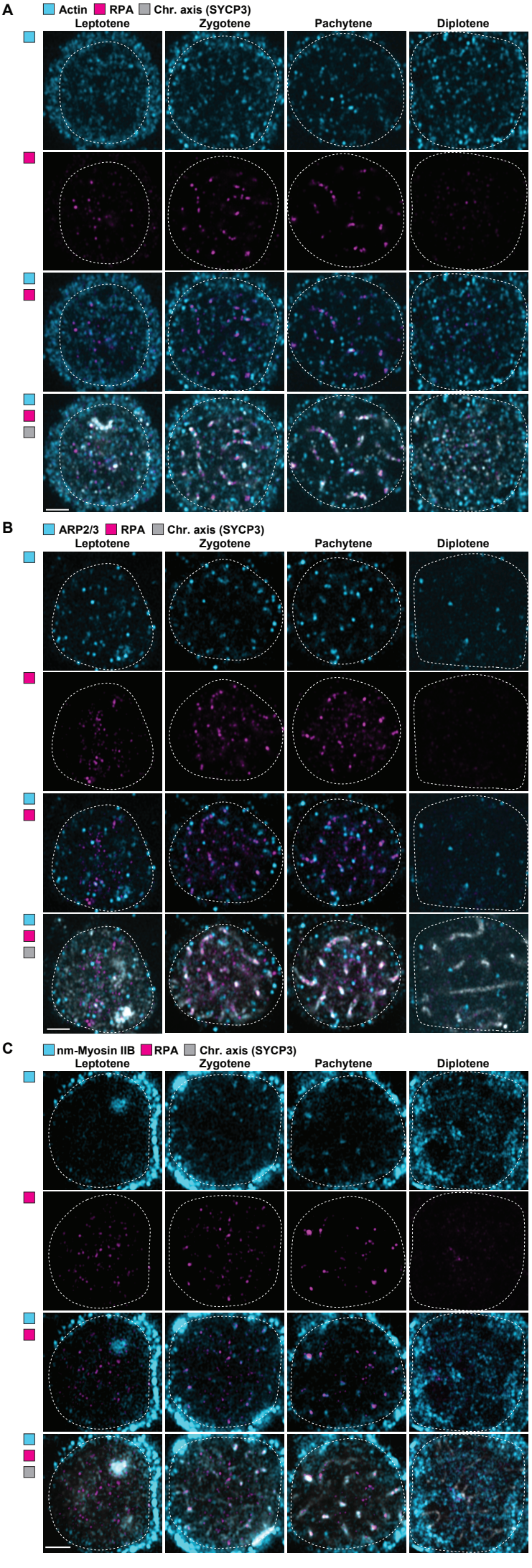
A
Actin
RPA
Chr. axis (SYCP3)
Leptotene
Zygotene
Pachytene
Diplotene
B
ARP2/3
RPA
Chr. axis (SYCP3)
Leptotene
Zygotene
Pachytene
Diplotene
C
nm-Myosin IIB
RPA
Chr. axis (SYCP3)
Leptotene
Zygotene
Pachytene
Diplotene

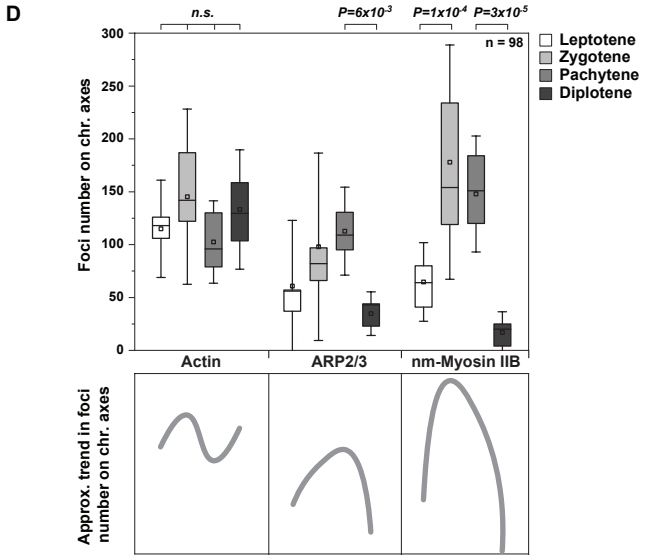
D
n.s.
P=6x10-3
P=1x10-4
P=3x10-5
n = 98
Leptotene
Zygotene
Pachytene
Diplotene
Foci number on chr. axes
Actin
ARP2/3
nm-Myosin IIB
Approx. trend in foci number on chr. axes

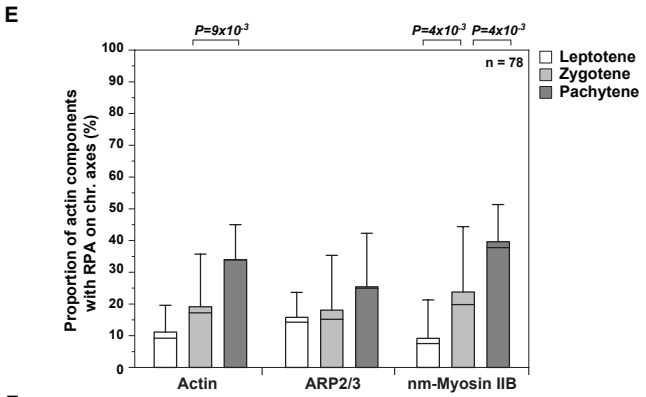
E
P=9x10-3
P=4x10-3
P=4x10-3
n = 78
Leptotene
Zygotene
Pachytene
Proportion of actin components with RPA on chr. axes (%)
Actin
ARP2/3
nm-Myosin IIB

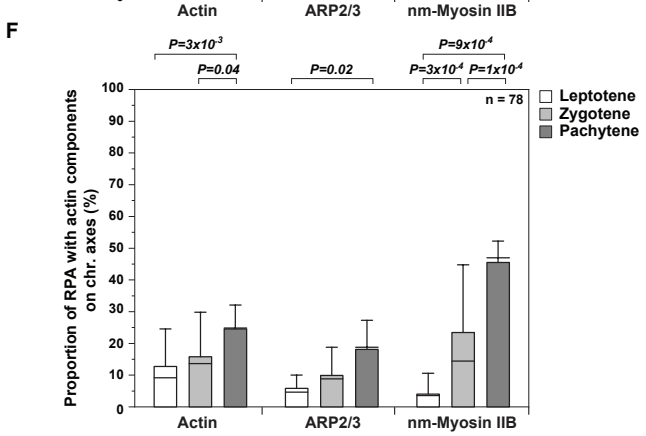
F
P=3x10-3
P=0.04
P=0.02
P=9x10-4
P=3x10-4
P=1x10-4
n = 78
Leptotene
Zygotene
Pachytene
Proportion of RPA with actin components on chr. axes (%)
Actin
ARP2/3
nm-Myosin IIB

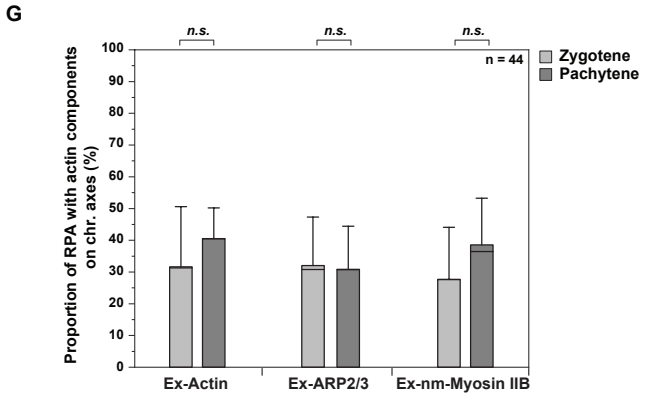
G
n.s.
n.s.
n.s.
n = 44
Zygotene
Pachytene
Proportion of RPA with actin components on chr. axes (%)
Ex-Actin
Ex-ARP2/3
Ex-nm-Myosin IIB

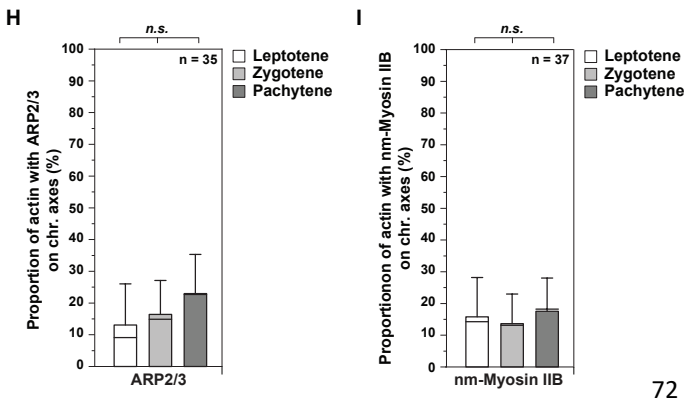
H
n.s.
n = 35
Leptotene
Zygotene
Pachytene
Proportion of actin with ARP2/3 on chr. axes (%)
ARP2/3
I
n.s.
n = 37
Leptotene
Zygotene
Pachytene
Proportionon of actin with nm-Myosin IIB on chr. axes (%)
nm-Myosin IIB

Figure 5: Nuclear actin structures are comprised of monomeric and polymeric actin but not classic filamentous actin. Shown on next page. Representative images of spermatocytes during different stages of meiotic prophase stained with anti-Actin C4 (A), anti-Actin 2G2 (B), anti-Actin 1C7 (C), and fluorescently labelled phalloidin (D). Monomeric and polymeric actin are visualized in spermatocyte nuclei (A-C) while filamentous actin is not visualized in spermatocyte nuclei (D). Central Z positions of spermatocytes are shown. Circles highlight spermatocyte nuclei. Scale bars, 2 μm. Chr. is an abbreviation of chromosome.

Figure 5

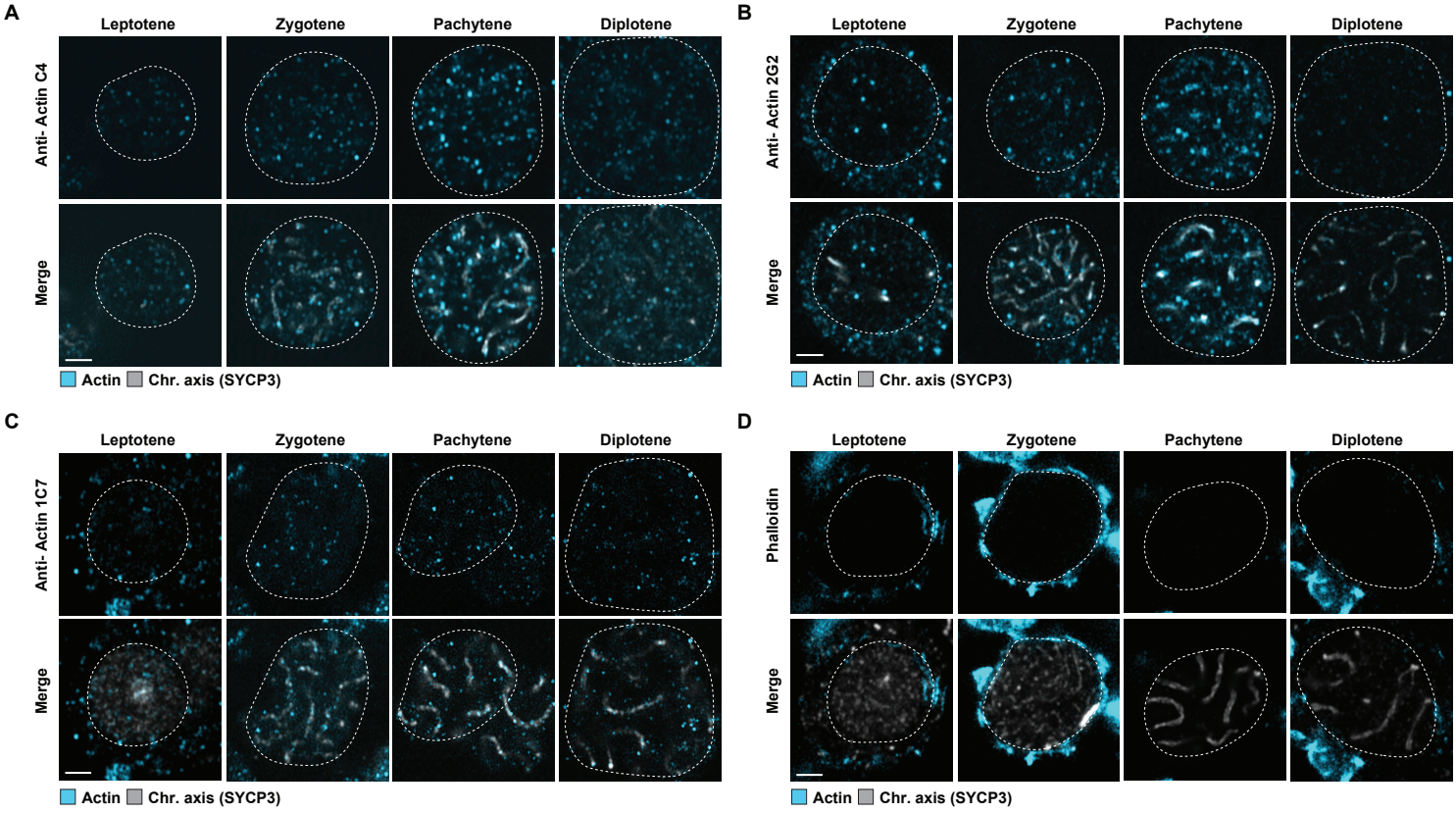
A
Leptotene
Zygotene
Pachytene
Diplotene
Anti- Actin C4
Merge
Actin
Chr. axis (SYCP3)
B
Leptotene
Zygotene
Pachytene
Diplotene
Anti- Actin 2G2
Merge
Actin
Chr. axis (SYCP3)
C
Leptotene
Zygotene
Pachytene
Diplotene
Anti- Actin 1C7
Merge
Actin
Chr. axis (SYCP3)
D
Leptotene
Zygotene
Pachytene
Diplotene
Phalloidin
Merge
Actin
Chr. axis (SYCP3)

2.3.2. nm-myosin IIB associates with RPA-containing HR nodules on chromosome axes

Myosins can motor along actin structures in the nucleus and facilitate the movement of chromosomal regions including during homologous recombination (Caridi et al., 2018; Hartman and Spudich, 2012). Therefore, I next investigated whether myosins also localize to chromosome axes during meiotic prophase. Strikingly, foci of nm-myosin IIB (Fig. 6A), nm-myosin IIA (Fig. 6B), myosin Iβ, (Fig. 6C), and myosin VI (Fig. 6D) are detected along chromosome axes during pachytene. In contrast, other nuclear myosins (myosin Va, myosin Vb, or myosin X) do not localize to chromosome axes (Fig. 6E-G). In particular, I detected that nm-myosin IIB associates with RPA foci on chromosome axes (Fig. 6A). RPA localizes to HR nodules where it protects ssDNA (described in further detail in chapter 1) (Bastin-Shanower and Brill, 2001; Bochkareva et al., 2002; Chen et al., 2013; Iftode and Borowiec, 2000). In contrast, a less clear association is observed between RPA foci and either nm-myosin IIA (Fig. 6B), myosin Iβ (Fig. 6C), or myosin VI (Fig. 6D). The foci number of nm-myosin IIB along chromosome axes fluctuates similarly to ARP2/3 as prophase progresses (Fig. 4C, 4D). Specifically, a mean of 64.7 nm-myosin IIB foci are detected per cell along chromosome axes in leptotene, 147.9 foci during pachytene, and, 17 foci during diplotene (Fig. 4D). Together this reveals that nm-myosin IIB is transiently located on chromosome axes and associates with RPA-containing HR nodules.

Figure 6: Myosins are detected along chromosome axes during pachytene. Shown on next page. Left, representative images of pachytene chromosome spreads. Boxes denote magnified chromosome axes. Right, magnified examples of chromosome axes of homologous chromosomes. Non-muscle myosin IIB (nm-Myosin IIB) (A), non-muscle myosin IIA (nm-Myosin IIA) (B), Myosin Iβ (C), and Myosin VI (D) are detected along chromosome axes with RPA foci. Myosin Va (E), Myosin Vb (F), and Myosin X (G) are not detected along chromosome axes. Scale bar, 10 μm. Chr. is an abbreviation of chromosome.

Figure 6

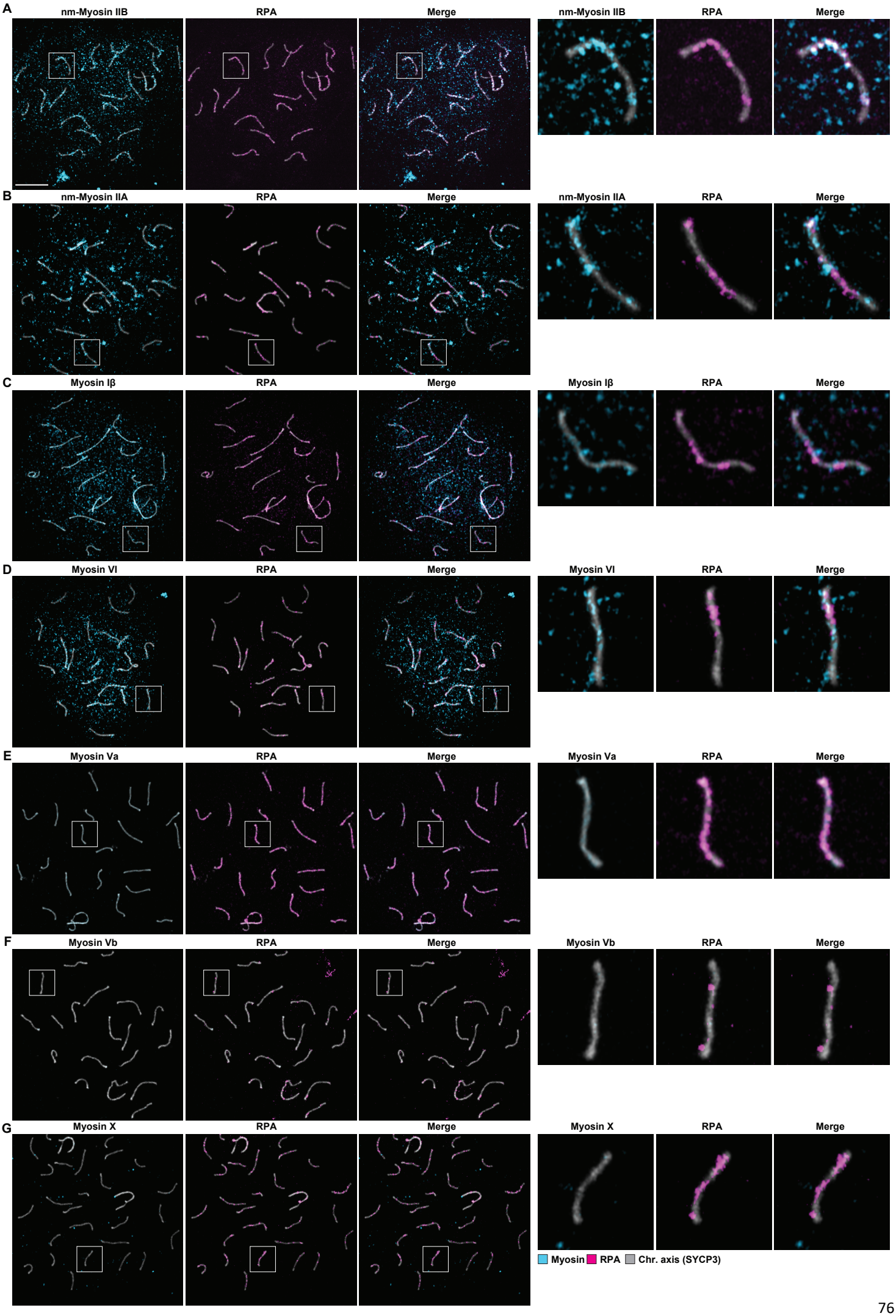
A
nm-Myosin IIB
RPA
Merge
nm-Myosin IIB
RPA
Merge
B
nm-Myosin IIA
RPA
Merge
nm-Myosin IIA
RPA
Merge
C
Myosin Iβ
RPA
Merge
Myosin Iβ
RPA
Merge
D
Myosin VI
RPA
Merge
Myosin VI
RPA
Merge
E
Myosin Va
RPA
Merge
Myosin Va
RPA
Merge
F
Myosin Vb
RPA
Merge
Myosin Vb
RPA
Merge
G
Myosin X
RPA
Merge
Myosin X
RPA
Merge
Myosin
RPA
Chr. axis (SYCP3)

2.3.3. Actin, ARP2/3, and nm-myosin IIB associate with a subset of RPA-containing HR nodules

Similar to nm-myosin IIB, actin and ARP2/3 also associate with RPA foci along chromosome axes (Fig. 4A-C). I found that only a fraction of actin, ARP2/3, and nm-myosin IIB foci on chromosome axes associate with RPA foci, increasing from a mean of 12% during leptotene to 33% during pachytene (Fig. 4E). In addition, only a subset of RPA foci associate with actin, ARP2/3, and nm-myosin IIB (referred together from here as 'actin components') (Fig. 4F). In particular, actin associates with a mean of 12.7% of RPA foci during leptotene and 24.5% of RPA foci in pachytene (Fig. 4F). ARP2/3 associates with a slightly smaller subset of RPA foci on average, specifically 5.8% of RPA foci during leptotene, and 18.1% of RPA foci during pachytene (Fig. 4F). Finally, nm-myosin IIB associates with 4% of RPA foci on average in leptotene and 45.5% of RPA foci in pachytene (Fig. 4F). Furthermore, exogenously expressed fluorescently labelled actin components also associate with a subset of RPA foci along chromosome axes (Fig. 4G), confirming my previous observations (Fig. 4E, 4F). Overall, these results reveal that a subset of both actin components and RPA-containing HR nodules associate during meiotic prophase.

I next investigated whether the actin components associate together along chromosome axes. I predicted this would enable ARP2/3 to nucleate actin structures along chromosome axes and at HR nodules that nm-myosin IIB could then bind and generate forces along. I found that a mean of 17.5% of actin foci associate with ARP2/3 (Fig. 4H), while 15.6% of actin foci associate with nm-myosin IIB (Fig. 4I). This demonstrates that actin foci indeed associate with a subset of both ARP2/3 and nm-myosin IIB along chromosome axes.

2.3.4. Actin, ARP2/3, and nm-myosin IIB associate with HR nodules during post-resection, strand invasion, and pre-resolution stages

Next, I investigated whether actin components localize to HR nodules during specific stages of homologous recombination. RPA protects ssDNA during three main stages of homologous recombination, specifically after strand resection (post-resection), during strand invasion, and before the formation of crossovers/non-crossovers (pre-resolution) (Moens et al., 2002; Oliver-Bonet et al., 2007; Plug et al., 1998). During meiotic prophase, the stage of homologous recombination can be inferred based on the morphology of chromosome axes. In particular, post-resection occurs on unaligned single chromosome axes (Moens et al., 2002; Plug et al., 1998). Strand invasion occurs at forks between aligning homologous chromosome axes, or, on aligned double homologous chromosome axes (Moens et al., 2002; Plug et al., 1998). Following this, pre-resolution occurs only on the aligned double homologous chromosome axes (Moens et al., 2002; Plug et al., 1998). To address whether the actin components are present at HR nodules during post-resection, strand invasion, or pre-resolution stages, I analyzed the morphology of chromosome axes where the actin components associate with RPA. I then inferred the stage of homologous recombination based on the morphology of the chromosome axes. Specifically, single chromosome axes indicate the post-resection stage, forked chromosome axes indicate the strand invasion stage, and double chromosome axes indicate strand invasion or pre-resolution stages (Fig. 7D). This analysis was conducted in zygotene cells since post-resection, strand invasion, and pre-resolution all occur during this meiotic stage. Using SYCP3 as a marker for chromosome axes, I found that the actin components associate with RPA foci at single, forked, and double chromosome axes (Fig 7A-C, 7E). More than 50% of actin, ARP2/3, and nm-myosin IIB foci associate with RPA on double chromosome axes, while roughly 20% of each actin component associates with RPA on either

single or forked chromosome axes (Fig. 7E). Similar fractions of either actin or ARP2/3 associate with RPA on single and forked chromosome axes (Fig. 7E). However, significantly more nm-myosin IIB associates with RPA on single axes compared to forked axes (Fig. 7E). These results indicate that actin, ARP2/3, and nm-myosin IIB are localized at HR nodules from post-resection stage and continue to accumulate at HR nodules until the pre-resolution stage of homologous recombination.

I next analyzed the association between actin and RPA foci on chromosome axes marked with SYCP1. Unlike SYCP3, which is a component of all chromosome axes, SYCP1 is only a component of synapsed (post-aligned) chromosome axes (Meuwissen et al., 1992). By analyzing the association on SYCP1-marked axes, I could distinguish more clearly the single (without SYCP1) and double (with SYCP1) chromosome axes that would otherwise appear indistinguishable when SYCP3 is used as a marker. Here, I found that a mean of 24.7% of actin foci associate with RPA on single chromosome axes (without SYCP1) while 75.3% of actin foci associate with RPA on double chromosome axes (with SYCP1) (Fig. 7F). This corroborates that a larger proportion of actin components associate with RPA foci on double chromosome axes that have already synapsed compared to single chromosome axes that have not.

To verify whether actin components associate with HR nodules during strand invasion, I analyzed the association between actin components and the strand invasion proteins, RAD51 and DMC1 (Bishop, 1994; Bishop et al., 1992). RAD51 and DMC1 generate nucleoprotein filaments along resected ssDNA, which stretch the ssDNA, a process that facilitates homology search and strand invasion (Chen et al., 2008). I detected that actin components associate with a consistent number of RAD51 or DMC1 foci between leptotene and pachytene along

chromosome axes (Fig. 7G). This indicates that the actin components are present at the HR nodules where the proteins RAD51 and DMC1 function during strand invasion. RPA remains associated with ssDNA during RAD51/DMC1-induced strand invasion (Gibb et al., 2014; Ma et al., 2017a). Indeed, in mammalian spermatocytes a subset of RPA and RAD51/DMC1 foci associate along chromosome axes (Fig. 7H) (Moens et al., 2002). Notably, actin and ARP2/3 associate with a similar number of RPA foci as RAD51 during leptotene (between 5.8% to 12.7% of RPA) and pachytene (between 18% to 24.5% of RPA) (Fig. 4F, 7H). While this is also the case for nm-myosin IIB during leptotene, nm-myosin IIB associates with 45.1% more RPA foci than RAD51 during pachytene (Fig. 4F, 7H). Taken together, these results indicate that actin components associate with RPA-containing HR nodules during post-resection, strand invasion, and pre-resolution stages of homologous recombination.

Finally, I investigated how frequently the actin components associate with HR nodules during post-resection, strand invasion, and pre-resolution. Through analysis of zygotene chromosome spreads, I detected that on average nm-myosin IIB associates with 59.7% of RPA foci on single chromosome axes, and either 85% or 91.9% of RPA foci on forked or double chromosome axes, respectively (Fig. 7I, 7J). This suggests that nm-myosin IIB frequently associates with HR nodules throughout the different homologous recombination stages. These results suggest that nm-myosin IIB could associate with an even larger subset of RPA foci than previously quantified in intact spermatocytes (Fig. 4F). Low antibody penetration or low antibody binding in intact cells versus chromosome spreads might account for these quantification differences in RPA association.

Figure 7: Actin, ARP2/3, and nm-myosin IIB associate with HR nodules during post-resection, strand invasion, and pre-resolution. Shown on next page. (A-C) Representative images of actin (A), ARP2/3 (B), and nm-myosin IIB (C) foci with RPA along chromosome axes of different morphologies. Single Z position of chromosome axes are shown. Dashed lines highlight the morphology of chromosome axes. Scale bars, 0.5 µm. (D) Schematic of the different morphologies of chromosome axes during zygotene and the associated stages of homologous recombination (HR) expected to occur. (E) Quantification of the proportions of actin components associated with RPA at single, forked, or double chromosome axes. P-values calculated using two-tailed Fisher's exact test. Two experimental replicates are shown. (F) Quantification of the proportions of actin foci associated with RPA on chromosomes axes labelled with (double axes) and without (single axis) SYCP1. (G) Quantification of the amount of RAD51 (for actin) or DMC1 (for ARP2/3 and nm-myosin IIB) foci associated with actin components along chromosome axes per cell during meiotic prophase. Mean and median lines are shown along with the standard deviation for two experimental replicates. P-values calculated using two-sided Student's t-test. (H) Quantification of the amount of RPA foci associated with RAD51 along chromosome axes per cell during meiotic prophase. Mean and median lines are shown along with the standard deviation for one experimental replicate. P-values calculated using two-sided Student's t-test. (I) Top, representative image of nm-myosin IIB and RPA foci along spread zygotene chromosome axes. Boxes denote magnified chromosome axes. Bottom, magnified examples of the chromosome axes of a pair of homologous chromosomes. Circles denote RPA foci associated with nm-myosin IIB on a single axis (SA), forked axes (FA), or double axes (DA). Scale bar, 10 µm. (J) Quantification of the amount of RPA foci associated with nm-myosin IIB at single, forked and double chromosome axes. Mean and median lines are shown along with the standard deviation for two experimental replicates. P-values calculated using two-tailed Fisher's exact test. n.s., not significant. n is the number of spermatocytes or in (E, J) the number of homologous chromosome axes analyzed. Chr. is an abbreviation of chromosome.

Figure 7

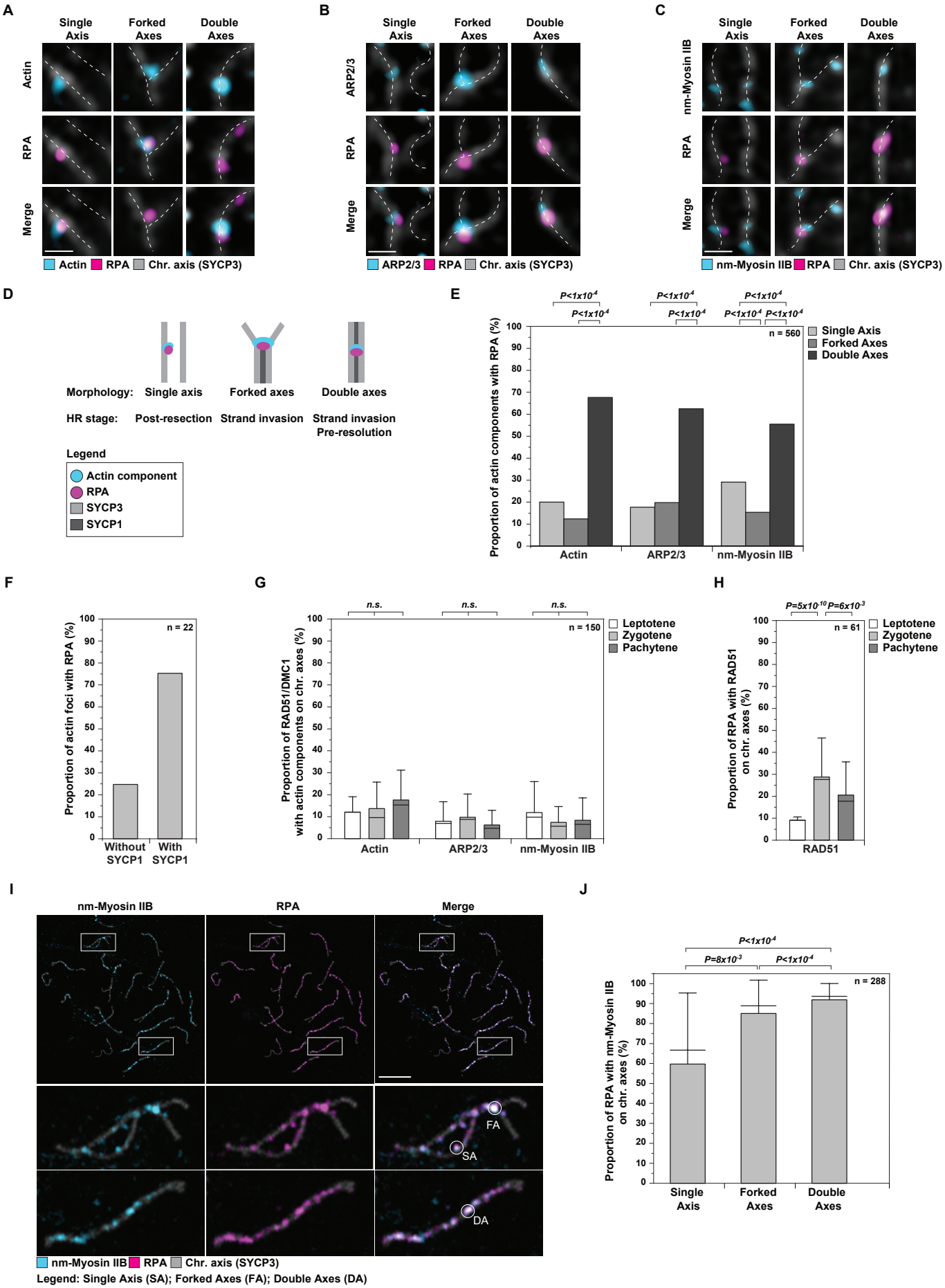
A
Single Axis
Forked Axes
Double Axes
Actin
RPA
Merge
Actin RPA Chr. axis (SYCP3)
B
ARP2/3
ARP2/3 RPA Chr. axis (SYCP3)
C
nm-Myosin IIB
nm-Myosin IIB RPA Chr. axis (SYCP3)
D
Morphology: Single axis Forked axes Double axes
HR stage: Post-resection Strand invasion Strand invasion Pre-resolution
Legend
Actin component
RPA
SYCP3
SYCP1
E
P<1x10-4
n = 560
Proportion of actin components with RPA (%)
Actin
ARP2/3
nm-Myosin IIB
F
n = 22
Proportion of actin foci with RPA (%)
Without SYCP1
With SYCP1
G
n.s.
n = 150
Proportion of RAD51/DMC1 with actin components on chr. axes (%)
Leptotene
Zygotene
Pachytene
H
P=5x10-10 P=6x10-3
n = 61
Proportion of RPA with RAD51 on chr. axes (%)
RAD51
I
nm-Myosin IIB
RPA
Merge
FA
SA
DA
nm-Myosin IIB RPA Chr. axis (SYCP3)
Legend: Single Axis (SA); Forked Axes (FA); Double Axes (DA)
J
P<1x10-4
P=8x10-3
n = 288
Proportion of RPA with nm-Myosin IIB on chr. axes (%)

2.3.5. Establishing a method to perturb actin, ARP2/3, and nm-myosin IIB during meiotic prophase

Next I aimed to investigate the functions that actin components play during meiotic prophase. To this end, I setup an *ex vivo* testis culture system, where the functions of actin components can be perturbed during specific stages of meiotic prophase (Fig. 8A). I achieved this by targeting the first wave of spermatogenesis in newborn male mice, which is the only synchronous cycle of spermatogenesis (Bellve et al., 1977; Yoshida et al., 2006). While monomeric actin can perform functions in the nucleus (Zheng et al., 2009), I anticipated that the association of ARP2/3 and actin along chromosome axes (Fig. 4H) indicates a role for polymerized actin during homologous recombination in meiosis. This is likely given that actin polymers nucleated by ARP2/3 appear to be restricted to homologous recombination, while formins and spire proteins tend to nucleate actin polymers involved in NHEJ in somatic cells (Aymard et al., 2017; Belin et al., 2015; Caridi et al., 2018; Schrank et al., 2018). To investigate whether actin and ARP2/3 are involved in meiotic homologous recombination, testes were cultured with either Cytochalasin-D (Cyt-D) to perturb general actin polymerization (Wakatsuki et al., 2001), or with the drug CK-666 to perturb ARP2/3-induced actin polymerization (Hetrick et al., 2013; Ilatovskaya et al., 2013). In addition, the role of nm-myosin IIB during prophase was investigated through culturing testes with the drug ML-7, a general myosin II inhibitor (Krakup et al., 1998; Saitoh et al., 1987). Treatment with either Cyt-D, CK-666, or ML-7 from leptotene to pachytene leads to a reduction in the number of actin components along chromosome axes (Fig. 8B-G). This indicates that actin perturbations through *ex vivo* testis cultures can impede the recruitment of actin components to chromosome axes. Furthermore, it suggests that actin foci present along chromosome axes

consist of polymerized actin structures, given that both Cyt-D and CK-666 treatments reduce the level of actin foci along chromosome axes.

Figure 8: Cyt-D, CK-666, and ML-7 treatments perturb actin components during meiotic prophase. Shown on next page. (A) Left, illustration of *ex vivo* testes culture. Right, schematic of culture period of mouse testes from 11 days post-partum (dpp) male mice to study the effect of perturbing actin components from leptotene to either zygotene (1 day culture), early pachytene (3 days culture), or late pachytene (5 days culture) stages. (B-D) Representative images of actin (B), ARP2/3 (C), and nm-myosin IIB (D) foci along chromosome axes in pachytene spermatocytes following treatments with drugs (Cyt-D, CK-666, or ML-7) or vehicle (DMSO). Central Z positions of spermatocytes are shown. Circles highlight spermatocyte nuclei. Scale bars, 2 µm. (E-G) Quantifications of actin (E), ARP2/3 (F), and nm-myosin IIB (G) foci along chromosome axes in spermatocytes following treatments with drugs (Cyt-D, CK-666, or ML-7) or vehicle (DMSO). Mean (square), median (line), 25^{th} and 75^{th} quartiles (boxes) are shown along with the standard deviation for two experimental replicates each. P-values calculated using two-sided Student's t-test. n is the number of spermatocytes analyzed. Chr. is an abbreviation of chromosome.

Figure 8

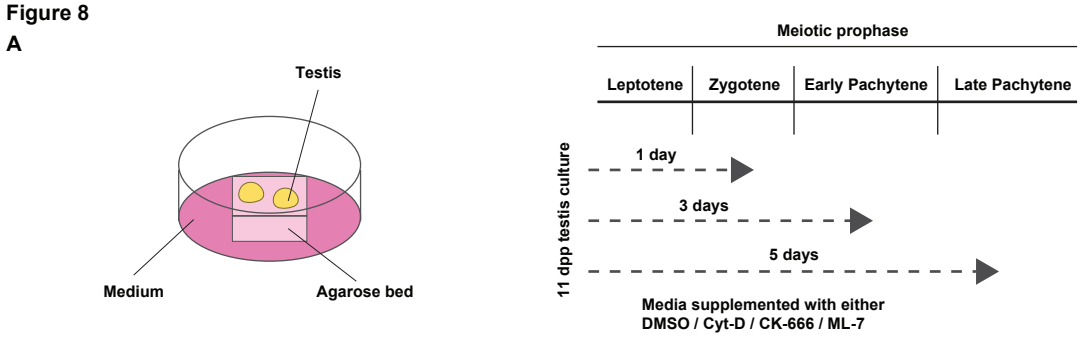
A
Testis
Medium
Agarose bed
Meiotic prophase
Leptotene
Zygotene
Early Pachytene
Late Pachytene
11 dpp testis culture
1 day
3 days
5 days
Media supplemented with either
DMSO / Cyt-D / CK-666 / ML-7

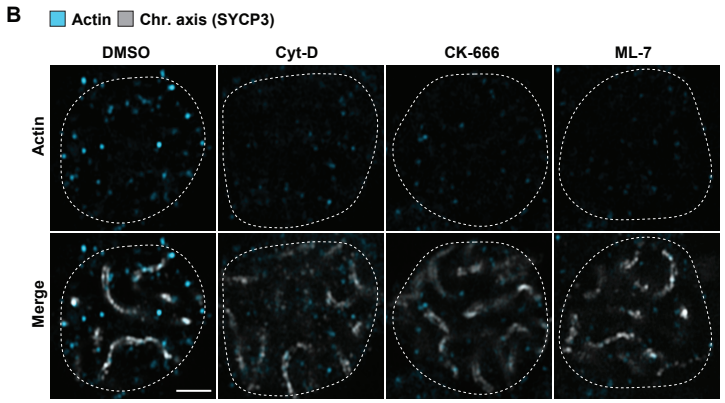
B
Actin
Chr. axis (SYCP3)
DMSO
Cyt-D
CK-666
ML-7
Actin
Merge

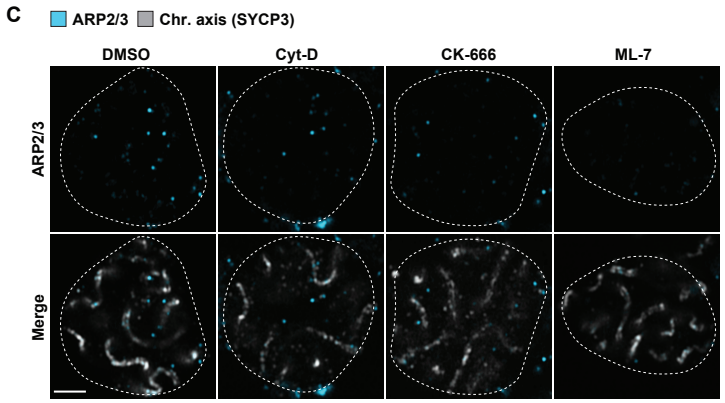
C
ARP2/3
Chr. axis (SYCP3)
DMSO
Cyt-D
CK-666
ML-7
ARP2/3
Merge

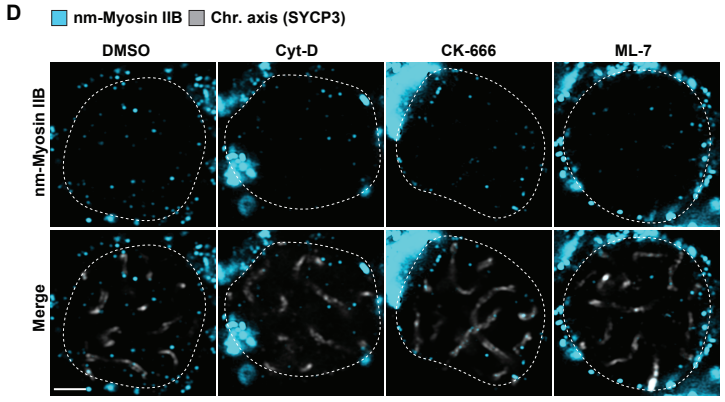
D
nm-Myosin IIB
Chr. axis (SYCP3)
DMSO
Cyt-D
CK-666
ML-7
nm-Myosin IIB
Merge

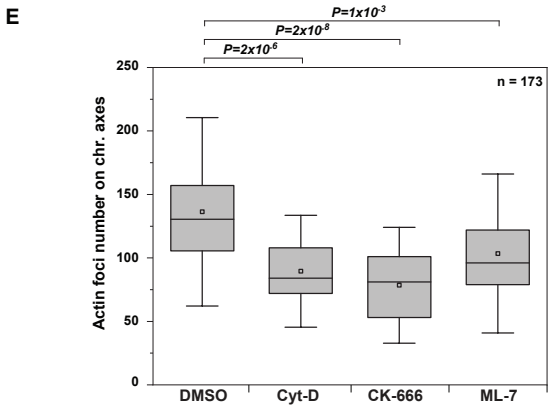
E
P=1x10-3
P=2x10-8
P=2x10-6
n = 173
Actin foci number on chr. axes
0
50
100
150
200
250
DMSO
Cyt-D
CK-666
ML-7

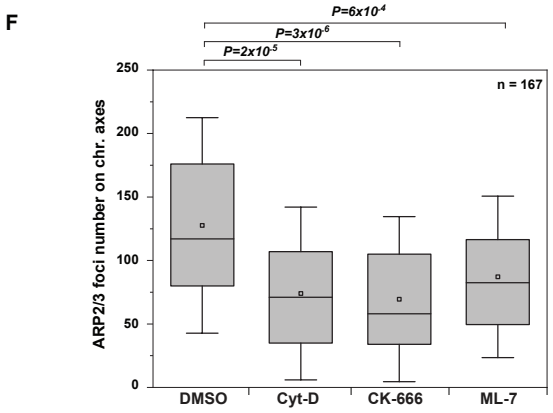
F
P=6x10-4
P=3x10-6
P=2x10-5
n = 167
ARP2/3 foci number on chr. axes
0
50
100
150
200
250
DMSO
Cyt-D
CK-666
ML-7

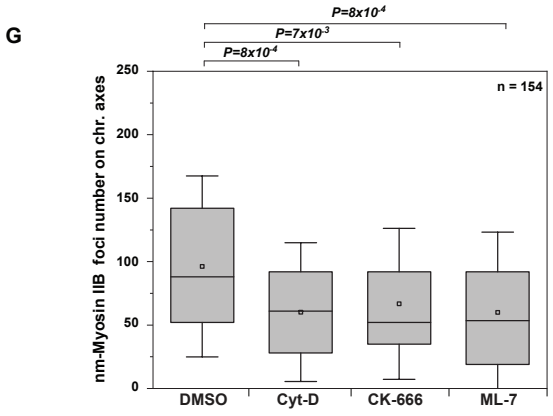
G
P=8x10-4
P=7x10-3
P=8x10-4
n = 154
nm-Myosin IIB foci number on chr. axes
0
50
100
150
200
250
DMSO
Cyt-D
CK-666
ML-7

2.3.6. Actin, ARP2/3, and nm-myosin IIB promote alignment of homologous chromosomes

Actin components localize to chromosome axes during several stages of meiotic prophase (Fig. 4D). They also localize to a subset of HR nodules throughout the different stages of homologous recombination (Fig. 7E-G). Therefore, I reasoned that actin components could perform a long-term structural function in promoting and maintaining the alignment of homologous chromosomes, which in turn could facilitate inter-homolog recombination. During zygotene, homologous chromosomes align prior to the installment of SYCP1 transverse filaments between homologous chromosome axes (De Vries et al., 2005). When nm-myosin IIB activity is inhibited from leptotene to zygotene with ML-7, I detected a small percentage of homologous chromosomes (a mean of 7.7%) that completely lack SYCP1 installment along the axes (Fig. 9A, 9B). Similarly, when either actin polymerization (with Cyt-D) or ARP2/3 activity (with CK-666) is perturbed, 1.3% and 2% of homologous chromosomes lack SYCP1 axis installment, respectively (Fig. 9A, 9B). In comparison, when spermatocytes are cultured with only DMSO from leptotene to zygotene, all homologous chromosome axes contain SYCP1 (Fig. 9A, 9B). This indicates that a fraction of homologous chromosomes fail to undergo SYCP1 installment when actin components are perturbed.

Defects in SYCP1 installment can arise when homologous chromosome alignment is impaired (Ding et al., 2007; Shibuya et al., 2014a, 2015). Therefore, I next investigated whether homologous chromosome alignment defects become apparent when actin components are perturbed. Axial forks and bubbles are two main defects that appear when homologous chromosome alignment is disrupted. During zygotene, forks in chromosome axes appear while homologs align from one end to the other (Fig. 9C). In addition, bubbles within the chromosome axes are also apparent during initiation of axis alignment, occurring at

intermittent points along homologous chromosome axes (Fig. 9C). Axial forks and bubbles point to an inability of the homologous chromosomes to find or maintain correct homology when aligning. If actin components assist in homologous chromosome alignment, then the number of forks and bubbles along homologous chromosome axes should increase when actin components are perturbed. Indeed, I observed a 56% increase in forked chromosome axes in ML-7 treated cells and approximately a 20% increase in forked axes following either Cyt-D or CK-666 treatment compared to DMSO treated cells (Fig. 9D, 9E). I next analyzed if both ends of paired homologous chromosome axes were forked or if only one end was affected. Notably, there were significantly more homologous chromosomes with forks at both ends of the axes following either ML-7, Cyt-D, or CK-666 treatments, indicating a global impairment in homologous chromosome alignment (Fig. 9F). The number of homologous chromosomes with bubbled axes also increased by approximately 72% in both ML-7 and CK-666 treated cells compared to DMSO (Fig. 9D-E, 9G). Furthermore, homologous chromosomes with both forks and bubbles in the axis were detected more frequently following Cyt-D, CK-666, and ML-7 treatments compared to DMSO (Fig. 9H). Overall, these findings reveal that homologous chromosome alignment and SYCP1 installation during zygotene is disrupted when any of the actin components are perturbed.

Figure 9: Actin, ARP2/3, and nm-myosin IIB promote homologous chromosome alignment and SYCP1 installation during zygotene. Shown on next page. (A) Representative images of zygotene chromosome spreads showing the installment of SYCP1 along SYCP3-marked homologous chromosome axes following treatments with drugs (Cyt-D, CK-666, or ML-7) or vehicle (DMSO). Boxes highlight chromosome axes that lack SYCP1 installment and are magnified in images below. Scale bar, 10 µm. (B) Quantification of the number of homologous chromosomes (homologs) with and without SYCP1 installed along chromosome axes following treatments with drugs (Cyt-D, CK-666, or ML-7) or vehicle (DMSO). (C) Schematic illustrating the different morphologies that homologous chromosome axes can adopt during zygotene. (D) Representative images of zygotene chromosome spreads and the morphology of SYCP3-marked homologous chromosome axes following treatments with drugs (Cyt-D, CK-666, or ML-7) or vehicle (DMSO). Boxes highlight examples of forked and bubbled chromosome axes and are magnified in images below. Scale bar, 10 µm. (E) Quantification of the number of homologous chromosomes (homologs) with forks or bubbles along chromosome axes following treatments with drugs (Cyt-D, CK-666, or ML-7) or vehicle (DMSO). (F-H) Quantifications of the number of homologous chromosomes (homologs) with forked axes (F), bubbled axes (G), or both forked and bubbled axes (H) following treatments with drugs (Cyt-D, CK-666, or ML-7) or vehicle (DMSO). Two experimental replicates presented in all quantifications. All P-values calculated using two-tailed Fisher's exact test. n is the number of homologous chromosome axes analyzed. Chr. is an abbreviation of chromosome.

Figure 9

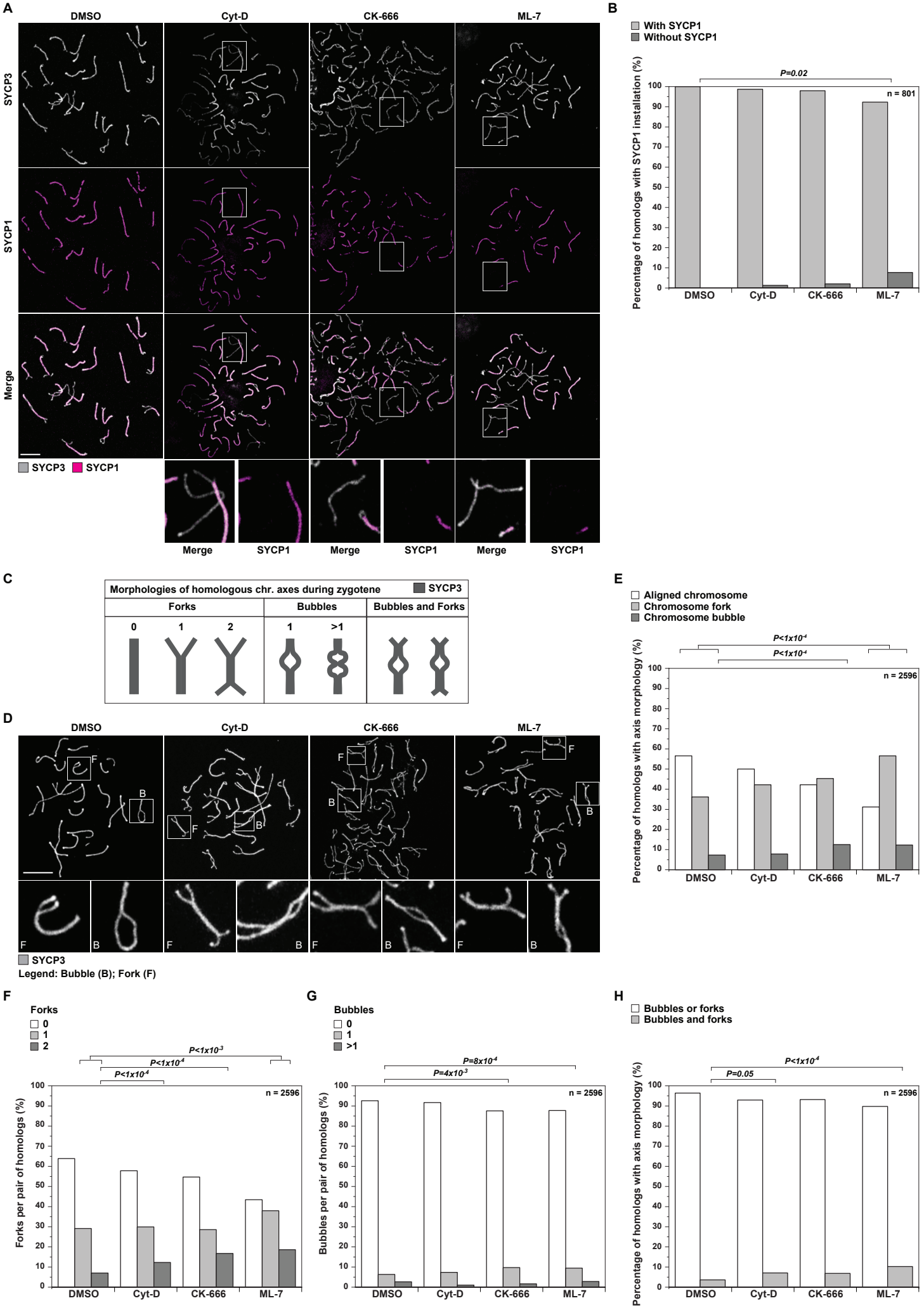
A
DMSO
Cyt-D
CK-666
ML-7
SYCP3
SYCP1
Merge
SYCP3 SYCP1
Merge
SYCP1
Merge
SYCP1
Merge
SYCP1
B
With SYCP1
Without SYCP1
P=0.02
n = 801
Percentage of homologs with SYCP1 installation (%)
DMSO
Cyt-D
CK-666
ML-7
C
Morphologies of homologous chr. axes during zygotene
SYCP3
Forks
Bubbles
Bubbles and Forks
0
1
2
1
>1
D
DMSO
Cyt-D
CK-666
ML-7
F
B
SYCP3
Legend: Bubble (B); Fork (F)
E
Aligned chromosome
Chromosome fork
Chromosome bubble
P<1x10-4
P<1x10-4
n = 2596
Percentage of homologs with axis morphology (%)
DMSO
Cyt-D
CK-666
ML-7
F
Forks
0
1
2
P<1x10-3
P<1x10-4
P<1x10-4
n = 2596
Forks per pair of homologs (%)
DMSO
Cyt-D
CK-666
ML-7
G
Bubbles
0
1
>1
P=8x10-4
P=4x10-3
n = 2596
Bubbles per pair of homologs (%)
DMSO
Cyt-D
CK-666
ML-7
H
Bubbles or forks
Bubbles and forks
P<1x10-4
P=0.05
n = 2596
Percentage of homologs with axis morphology (%)
DMSO
Cyt-D
CK-666
ML-7

2.3.7. Homologous chromosome synapsis depends on the activities of actin, ARP2/3, and nm-myosin IIB

Next, I investigated whether the defects in homologous chromosome alignment and in SYCP1 installation affect the completion of homologous chromosome synapsis when actin components are perturbed. By pachytene, synapsis of autosomal and sex chromosomes is complete (Moens et al., 2002). In spermatocytes, the sex chromosomes are the last set of homologs to synapse (Acquaviva et al., 2020). Completion of synapsis is verified by the presence of SYCP1 along the entire axis length of autosomes, and the presence of a SYCP1 fragment between the PAR of the X and Y chromosomes (Moens et al., 2002). I found that during pachytene, 10% of autosomes lack sections of SYCP1 along homologous chromosome axes in cells treated with either Cyt-D or ML-7 (Fig. 10A, 10B). Similarly, 3.7% of autosomes lack sections of SYCP1 along homologous chromosome axes following CK-666 treatment (Fig. 10A, 10B). Importantly, sex chromosomes are indeed synapsed in the drug-treated cells, confirming that spermatocytes are in the pachytene stage of meiosis. These results indicate that SYCP1 fails to extend along the entire length of autosomal axes when actin components are perturbed, hence leading to chromosome asynapsis. In addition, 2% of chromosomes exhibit small-scale (bubbled axes) and large-scale (chromosome crosses, chromosome rings) structural abnormalities in chromosome axes following either Cyt-D, CK-666, or ML-7 treatments (Fig. 10C, 10D). In comparison, no structural abnormalities are detected in pachytene chromosomes from cells treated only with DMSO (Fig. 10C, 10D). Taken together, these data reveal that when actin components are perturbed, correct alignment of homologs fails to occur, leading to structural abnormalities that include chromosome asynapsis during pachytene.

Figure 10: Actin, ARP2/3, and nm-myosin IIB are required for full synapsis of homologous chromosomes during pachytene. Shown on next page. (A) Representative images of pachytene chromosome spreads showing SYCP1 extension along SYCP3-marked homologous chromosome axes following treatments with drugs (Cyt-D, CK-666, or ML-7) or vehicle (DMSO). Boxes highlight homologous chromosome axes that lack full SYCP1 extension and are magnified in images below. Synapsed sex chromosomes are indicated (XY). Scale bar, 10 µm. (B) Quantification of the number of homologous chromosomes (homologs) that are synapsed (with complete SYCP1 extension) and asynapsed (with incomplete SYCP1 extension) during pachytene following treatments with drugs (Cyt-D, CK-666, or ML-7) or vehicle (DMSO). Two experimental replicates are presented. P-values calculated using two-tailed Fisher's exact test. (C) Images of pachytene chromosome spreads showing the abnormalities in chromosome axes that arise following treatments with drugs (Cyt-D, CK-666, or ML-7). Boxes highlight abnormal homologous chromosome morphologies (chromosome bubbles (B), crosses (C) and rings (R)) and are magnified at the bottom of the panel. Scale bar, 10 µm. (D) Quantification of the number of homologous chromosomes (homologs) with abnormal morphologies during pachytene following treatments with drugs (Cyt-D, CK-666, or ML-7) or vehicle (DMSO). A region of the graph (between 0 to 2%) is shown below to better visualize the abnormal morphology quantifications. Two experimental replicates presented. n is the number of homologous chromosome axes analyzed. Chr. is an abbreviation of chromosome.

Figure 10

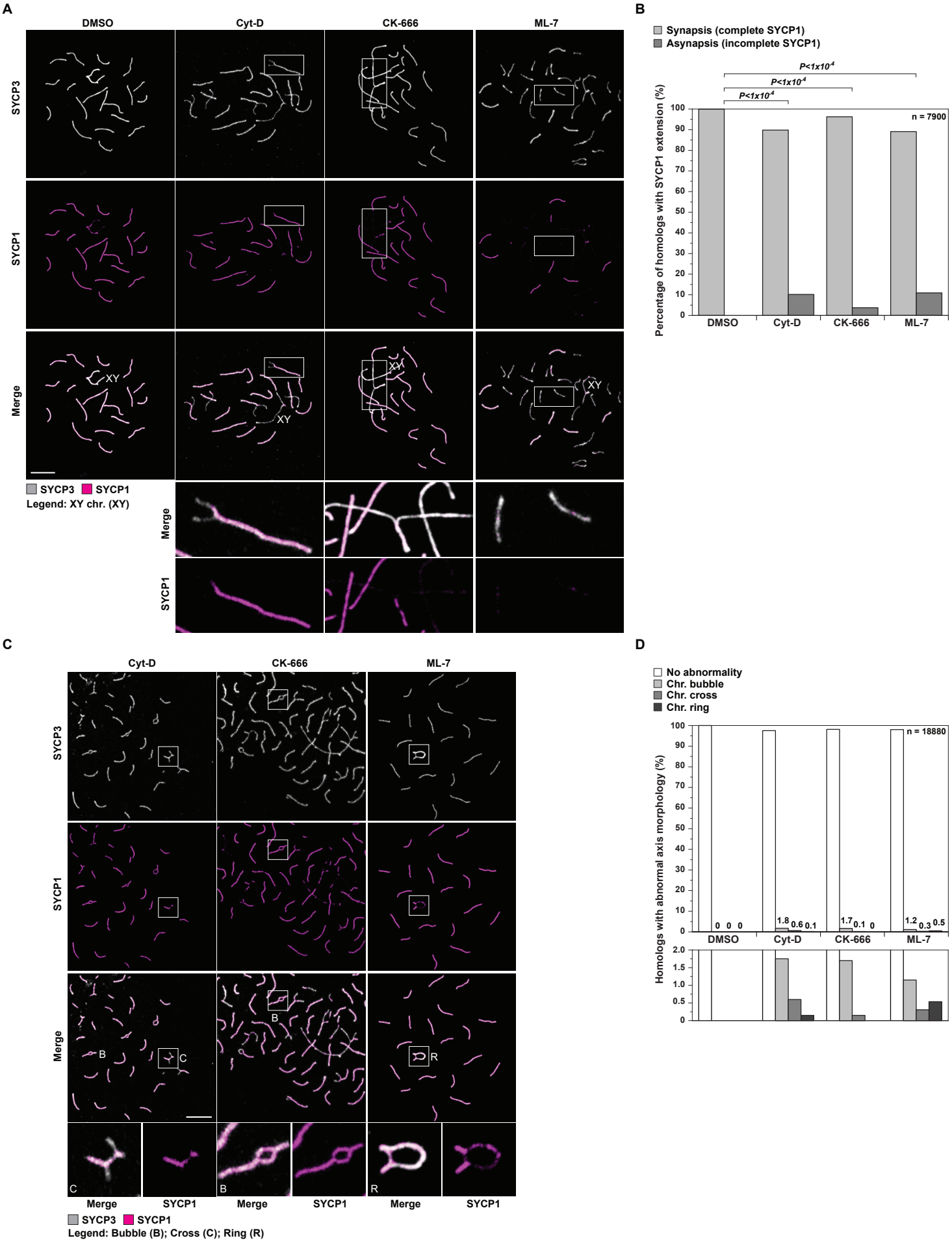
A
DMSO
Cyt-D
CK-666
ML-7
SYCP3
SYCP1
Merge
XY
SYCP3 SYCP1
Legend: XY chr. (XY)
B
Synapsis (complete SYCP1)
Asynapsis (incomplete SYCP1)
P<1x10-4
P<1x10-4
P<1x10-4
n = 7900
Percentage of homologs with SYCP1 extension (%)
DMSO
Cyt-D
CK-666
ML-7
C
Cyt-D
CK-666
ML-7
B
C
R
Merge
SYCP1
SYCP3 SYCP1
Legend: Bubble (B); Cross (C); Ring (R)
D
No abnormality
Chr. bubble
Chr. cross
Chr. ring
n = 18880
Homologs with abnormal axis morphology (%)
0 0 0
1.8 0.6 0.1
1.7 0.1 0
1.2 0.3 0.5
DMSO
Cyt-D
CK-666
ML-7

2.3.8. RPA and RAD51 chromosome axis localization depends on the activity of actin, ARP2/3, and nm-myosin IIB

The processes of homologous chromosome synapsis and homologous recombination are intimately linked. Indeed, chromosome asynapsis affects the success of inter-homolog strand invasion (Schwacha and Kleckner, 1997; De Vries et al., 2005). Therefore, I next asked whether perturbing actin components also affects proteins involved in inter-homolog strand invasion, such as RPA and RAD51 (Chen et al., 2008; Wang and Haber, 2004). Interestingly, I found that the number of RPA and RAD51 foci are reduced along chromosome axes in spermatocytes treated with Cyt-D, CK-666, and ML-7 during pachytene compared to cells treated with DMSO (Fig. 11A-D). Specifically, I detected a mean of 34.8% less RPA foci and 27.9% less RAD51 foci along chromosome axes after treatment with Cyt-D, an inhibitor of actin polymerization (Fig.11B, 11D). Cells treated with the ARP2/3 inhibitor, CK-666, also exhibit a similar reduction in RPA (28.7%) and RAD51 (18%) foci, while treatment with the myosin II inhibitor, ML-7, led to the least reduction in RPA (11.8%) and RAD51 (7.4%) foci along chromosome axes compared to DMSO (Fig. 11B, 11D). Furthermore, the associations between RPA-ARP2/3 and RPA-nm-myosin IIB are also reduced following either Cyt-D, CK-666, or ML-7 treatments relative to DMSO (Fig. 11E, 11F). Together this suggests that the localization of RPA and RAD51 along chromosome axes is dependent on the functions of actin, ARP2/3, and nm-myosin IIB.

I anticipated that the reduction in RPA and RAD51 foci may reduce the frequency of strand invasion, and thus impede DSB repair through homologous recombination. If so, this would lead to an increase in unrepaired DSBs, which are marked by γH2AX. However, I found that the number of DSBs is not significantly changed in Cyt-D or CK-666 treated cells in comparison to DMSO during late pachytene (Fig. 11G, 11H). In contrast, I detected a mean of 61% more

DSBs in cells treated with ML-7 relative to DMSO during late pachytene (Fig. 11G, 11H). This indicates that unrepaired DSBs accumulate along chromosome axes when nm-myosin IIB is perturbed but not when either actin or ARP2/3 are perturbed. Indeed, ML-7 inhibits other myosin II isoforms (Krakup et al., 1998; Saitoh et al., 1987), therefore not precluding the possibility that these unrepaired DSBs may accumulate due to unknown myosin II-related functions.

Figure 11: RPA and RAD51 localization along chromosome axes depends on actin, ARP2/3, and nm-myosin IIB activity. Shown on next page. (A, C) Representative images of RPA (A) and RAD51 (C) foci along chromosome axes in early pachytene spermatocytes following treatments with drugs (Cyt-D, CK-666, or ML-7) or vehicle (DMSO). Central Z positions of spermatocytes are shown. Circles highlight spermatocyte nuclei. Scale bars, 2 μm. (B, D) Quantifications of RPA (B) and RAD51 (D) foci along chromosome axes in early pachytene spermatocytes following treatments with drugs (Cyt-D, CK-666, or ML-7) or vehicle (DMSO). Mean (square), median (line), 25th and 75th quartiles (boxes) are shown along with the standard deviation for two experimental replicates each. (E-F) Quantifications of the amount of RPA foci associated with ARP2/3 (E) and nm-myosin IIB (F) along chromosome axes in late pachytene spermatocytes following treatments with drugs (Cyt-D, CK-666, or ML-7) or vehicle (DMSO). Mean (line) and median (line) are shown along with the standard deviation for one experimental replicate each. (G) Representative images of γH2AX foci along chromosome axes in late pachytene spermatocytes following treatments with drugs (Cyt-D, CK-666, or ML-7) or vehicle (DMSO). The sex chromosome body is annotated (XY). Central Z positions of spermatocytes are shown. Circles highlight spermatocyte nuclei. Scale bar, 2 μm. (H) Quantification of γH2AX foci along chromosome axes in late pachytene spermatocytes following treatments with drugs (Cyt-D, CK-666, or ML-7) or vehicle (DMSO). Mean (square), median (line), 25th and 75th quartiles (boxes) are shown along with the standard deviation for two experimental replicates. All P-values calculated using two-sided Student's t-test. n is the number of spermatocytes analyzed. Chr. is an abbreviation of chromosome.

Figure 11

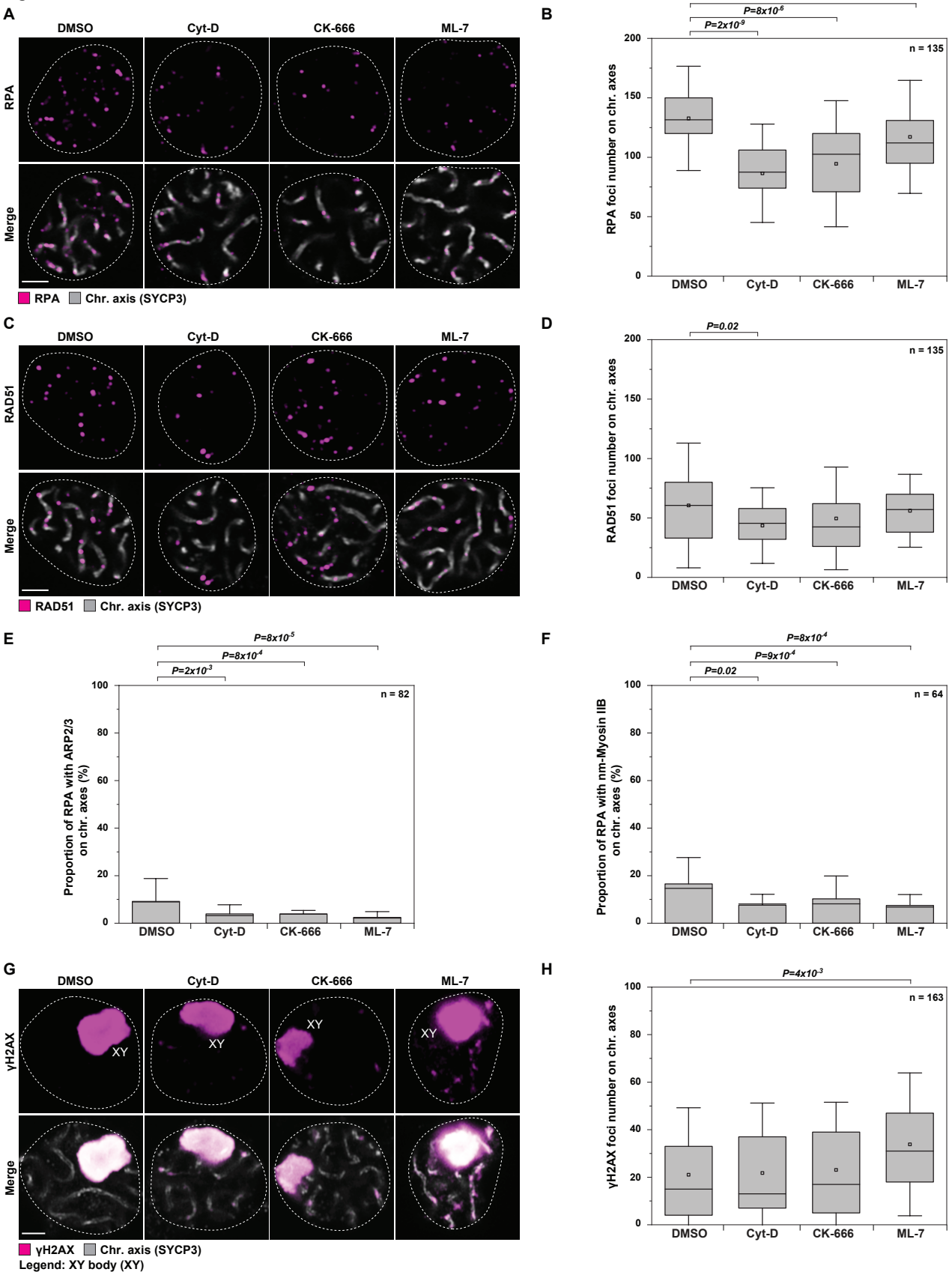
A
DMSO
Cyt-D
CK-666
ML-7
RPA
Merge
RPA Chr. axis (SYCP3)
B
P=0.05
P=8x10-6
P=2x10-9
n = 135
RPA foci number on chr. axes
C
RAD51
Merge
RAD51 Chr. axis (SYCP3)
D
P=0.02
n = 135
RAD51 foci number on chr. axes
E
P=8x10-5
P=8x10-4
P=2x10-3
n = 82
Proportion of RPA with ARP2/3 on chr. axes (%)
F
P=8x10-4
P=9x10-4
P=0.02
n = 64
Proportion of RPA with nm-Myosin IIB on chr. axes (%)
G
γH2AX
XY
γH2AX Chr. axis (SYCP3)
Legend: XY body (XY)
H
P=4x10-3
n = 163
γH2AX foci number on chr. axes

2.3.9. The localization of class I crossover proteins along chromosome axes depends on the activity of actin, ARP2/3, and nm-myosin IIB

Following strand invasion, arising D-loop structures can mature into dHJs (described in further detail in chapter 1) (Manhart and Alani, 2016). MSH-4/MSH-5 stabilize dHJs and recruit MLH-1/MLH-3, which in turn assists in the resolution of dHJs into crossovers (Rogacheva et al., 2014; Santucci-Darmanin et al., 2000; Snowden et al., 2004). MSH-4/MSH-5 and MLH-1/MLH-3 are major constituents of the class I crossover pathway, which is the dominant pathway utilized in meiosis to generate inter-homolog crossovers (described in further detail in chapter 1) (Manhart and Alani, 2016). I deduced that when actin components are perturbed, the reduction in RPA and RAD51 along chromosome axes could negatively affect D-loop and dHJ formation, leading to reduced localization of class I crossover proteins at HR nodules. Notably, the number of MSH-4 and MLH-1 foci along chromosome axes are indeed reduced following either Cyt-D, CK-666, or ML-7 treatments compared to DMSO (Fig. 12A-D). In particular, CK-666 treatment has the strongest effect on MSH-4 and MLH-1 foci number, with CK-666 treated cells found to have a mean of 42.9% less MSH-4 foci and 27.6% less MLH-1 foci along chromosome axes compared to DMSO (Fig. 12B, 12D). In comparison, Cyt-D treatment led to a mean reduction of 22.3% in MSH-4 foci and 16.5% in MLH-1 foci per cell, while ML-7 treated cells have 13% less MSH-4 foci and 13.8% less MLH-1 foci along chromosome axes (Fig. 12B, 12D). Together, this reveals that the localization of class I crossover proteins along chromosome axes is impeded when actin components are perturbed.

Figure 12: MSH-4 and MLH-1 localization along chromosome axes depends on actin, ARP2/3, and nm-myosin IIB activity. Shown on next page. (A,C) Representative images of MSH-4 (A) and MLH-1 (C) foci along chromosome axes in late pachytene spermatocytes following treatments with drugs (Cyt-D, CK-666, or ML-7) or vehicle (DMSO). Central Z positions of spermatocytes are shown. Circles highlight spermatocyte nuclei. Scale bars, 2 µm. (B,D) Quantifications of MSH-4 (B) and MLH-1 (D) foci along chromosome axes in late pachytene spermatocytes following treatments with drugs (Cyt-D, CK-666, or ML-7) or vehicle (DMSO). Mean (square), median (line), 25th and 75th quartiles (boxes) are shown along with the standard deviation for two experimental replicates each. All P-values calculated using two-sided Student's t-test. n is the number of spermatocytes analyzed. Chr. is an abbreviation of chromosome.

Figure 12

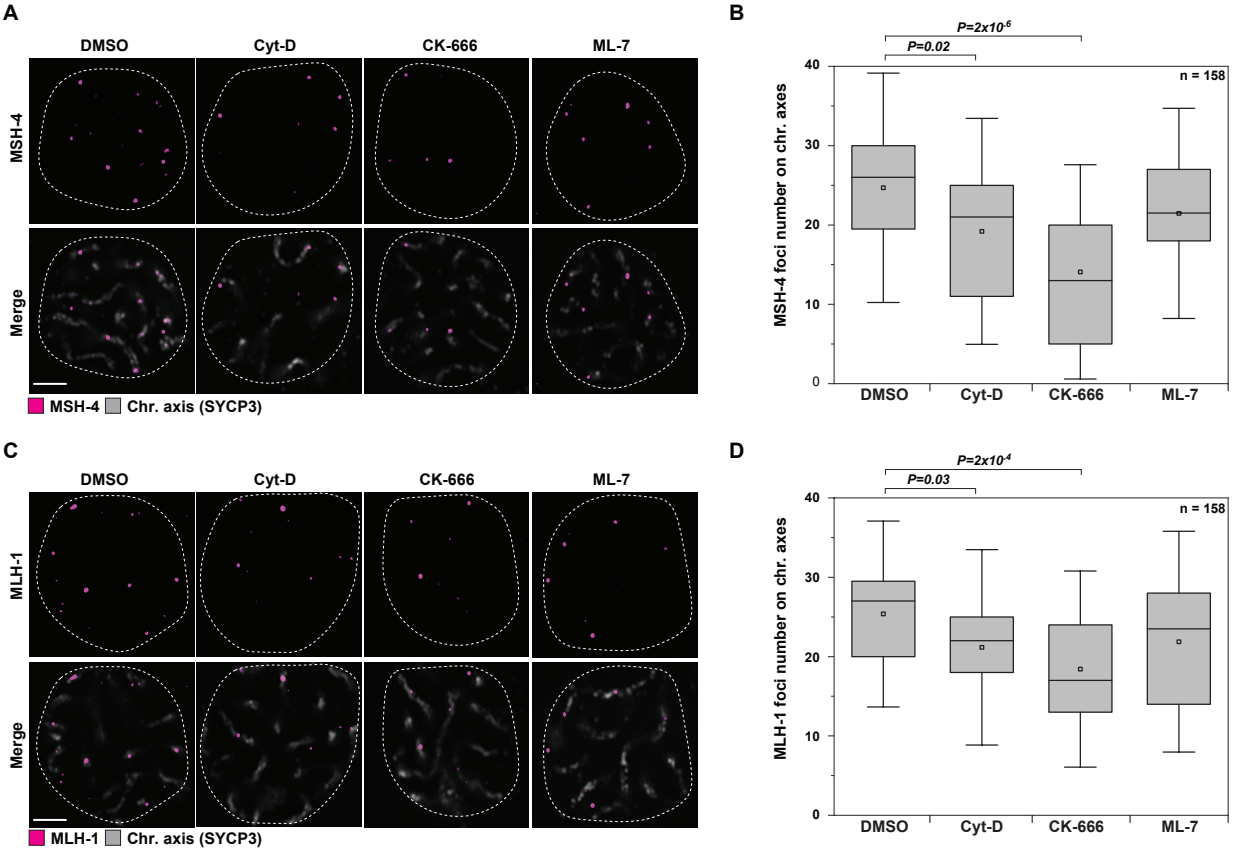
A
DMSO
Cyt-D
CK-666
ML-7
MSH-4
Merge
MSH-4 Chr. axis (SYCP3)
B
P=2x10-5
P=0.02
n = 158
MSH-4 foci number on chr. axes
0
10
20
30
40
DMSO
Cyt-D
CK-666
ML-7
C
DMSO
Cyt-D
CK-666
ML-7
MLH-1
Merge
MLH-1 Chr. axis (SYCP3)
D
P=2x10-4
P=0.03
n = 158
MLH-1 foci number on chr. axes
0
10
20
30
40
DMSO
Cyt-D
CK-666
ML-7

2.3.10. Class II crossover proteins and NHEJ proteins accumulate along chromosome axes when actin components are perturbed

While class I crossover proteins are reduced along chromosome axes following perturbations of actin components (Fig. 12), DSBs continue to be repaired effectively in Cyt-D and CK-666 treated cells (Fig. 11H). Therefore, I investigated if alternative DSB pathways compensate in repairing DSBs. The structure specific endonuclease MUS81 functions as a heterodimer with EME1 to promote the resolution of joint DNA molecules into crossovers via the class II crossover pathway (discussed in further detail in chapter 1) (Boddy et al., 2001; Higgins et al., 2008; Holloway et al., 2008; De los Santos et al., 2003). MUS81/EME1 can compensate to repair DSBs if the class I crossover pathway is perturbed (Holloway et al., 2008). Notably, I detected a significant increase in MUS81 foci along chromosome axes following Cyt-D, CK-666, or ML-7 treatments relative to DMSO (Fig. 13A, 13B). In addition, MUS81/EME1 may function in cooperation with XPF/ERCC1 (with XPF being another structure specific endonuclease) to generate crossovers (Agostinho et al., 2013; Kikuchi et al., 2013; O'Neil et al., 2013). Interestingly, I also detected a significant increase in ERCC1 foci along chromosome axes following Cyt-D, CK-666, or ML-7 treatments relative to DMSO (Fig. 13C). In some circumstances, ERCC1 cooperates with XPF to promote the resolution of joint DNA molecules or with XPA in nucleotide excision repair (Orelli et al., 2010). However, I did not detect a significant change in the number of XPA foci along chromosome axes following Cyt-D, CK-666, or ML-7 treatments relative to DMSO (Fig. 13D). Together this indicates that structure specific endonucleases MUS81 and XPF accumulate along chromosome axes when actin components are perturbed, while XPA does not. This results also suggests that XPF/ERCC1 functions during mammalian meiotic prophase with MUS81/EME1, similar to previous observations made in

somatic cells and in *C.elegans* meiotic germ cells (Agostinho et al., 2013; Kikuchi et al., 2013; O'Neil et al., 2013).

Additional DSB pathways such as the NHEJ pathway can compensate in DSB repair when the class I crossover pathway is perturbed (Macaisne et al., 2018; Smolikove et al., 2007; Yin and Smolikove, 2013). For example, Ku70 functions as a heterodimer with Ku80 to protect DNA ends from strand resection in the NHEJ pathway (Ramsden and Geliert, 1998). I found a significant increase in Ku70 foci along chromosome axes following Cyt-D, CK-666, or ML-7 treatments relative to DMSO (Fig. 13E, 13F). The largest increase in MUS81, ERCC1, or Ku70 foci number along chromosome axes was detected when either actin or ARP2/3 were perturbed compared to nm-myosin IIB (Fig. 13B, 13C, 13F). From this it can be inferred that the activity of certain DSB pathways, including the class II crossover and NHEJ pathways, are higher in Cyt-D or CK-666 treated cells compared to ML-7 treated cells. This could explain why DSBs are repaired when actin or ARP2/3 are perturbed and why unrepaired DSBs accumulate when nm-myosin IIB is perturbed. (Fig. 11H).

Finally, the SDSA pathway and the TMEJ pathway may also compensate in DSB repair when the class I crossover pathway is disrupted (Macaisne et al., 2018; Martin et al., 2005). I examined the number of BLM helicase and polymerase theta foci, active in the SDSA and TMEJ pathways, respectively, after perturbations of actin components. I found no significant change in the number of either BLM helicase (Fig. 13G) or polymerase theta (Fig. 13H) foci along chromosome axes following ML-7 treatment compared to DMSO. Together, these results indicate that proteins involved in specific DSB repair pathways, alternative to the class I crossover pathway, are increased along chromosome axes when actin components are

perturbed. Importantly, this further implicates the involvement of actin, ARP2/3, and nm-myosin IIB in the class I crossover pathway.

Figure 13: Class II crossover proteins and NHEJ proteins accumulate along chromosome axes when actin components are perturbed. Shown on next page. (A) Representative images of MUS81 foci along chromosome axes in late pachytene spermatocytes following treatments with drugs (Cyt-D, CK-666, or ML-7) or vehicle (DMSO). Central Z positions of spermatocytes are shown. Circles highlight spermatocyte nuclei. Scale bar, 2 µm. (B-D) Quantifications of MUS81 (B), ERCC1 (C) and XPA (D) foci along chromosome axes in late pachytene spermatocytes following treatments with drugs (Cyt-D, CK-666, or ML-7) or vehicle (DMSO). Two experimental replicates presented for each. (E) Representative images of Ku70 foci along chromosome axes in late pachytene spermatocytes following treatments with drugs (Cyt-D, CK-666, or ML-7) or vehicle (DMSO). The sex chromosome body is annotated (XY). Central Z positions of spermatocytes are shown. Circles highlight spermatocyte nuclei. Scale bar, 2 µm. (F) Quantification of Ku70 foci along chromosome axes in late pachytene spermatocytes following treatments with drugs (Cyt-D, CK-666, or ML-7) or vehicle (DMSO). Two experimental replicates presented. (G-H) Quantifications of BLM helicase (G) and polymerase theta (H) foci along chromosome axes in late pachytene spermatocytes following treatments with drugs (Cyt-D, CK-666, or ML-7) or vehicle (DMSO). One experimental replicate presented for each. For all quantifications, mean (square), median (line), 25^{th} and 75^{th} quartiles (boxes) are shown along with the standard deviation. All P-values calculated using two-sided Student's t-test. n.s., not significant. n is the number of spermatocytes analyzed. Chr. is an abbreviation of chromosome.

Figure 13

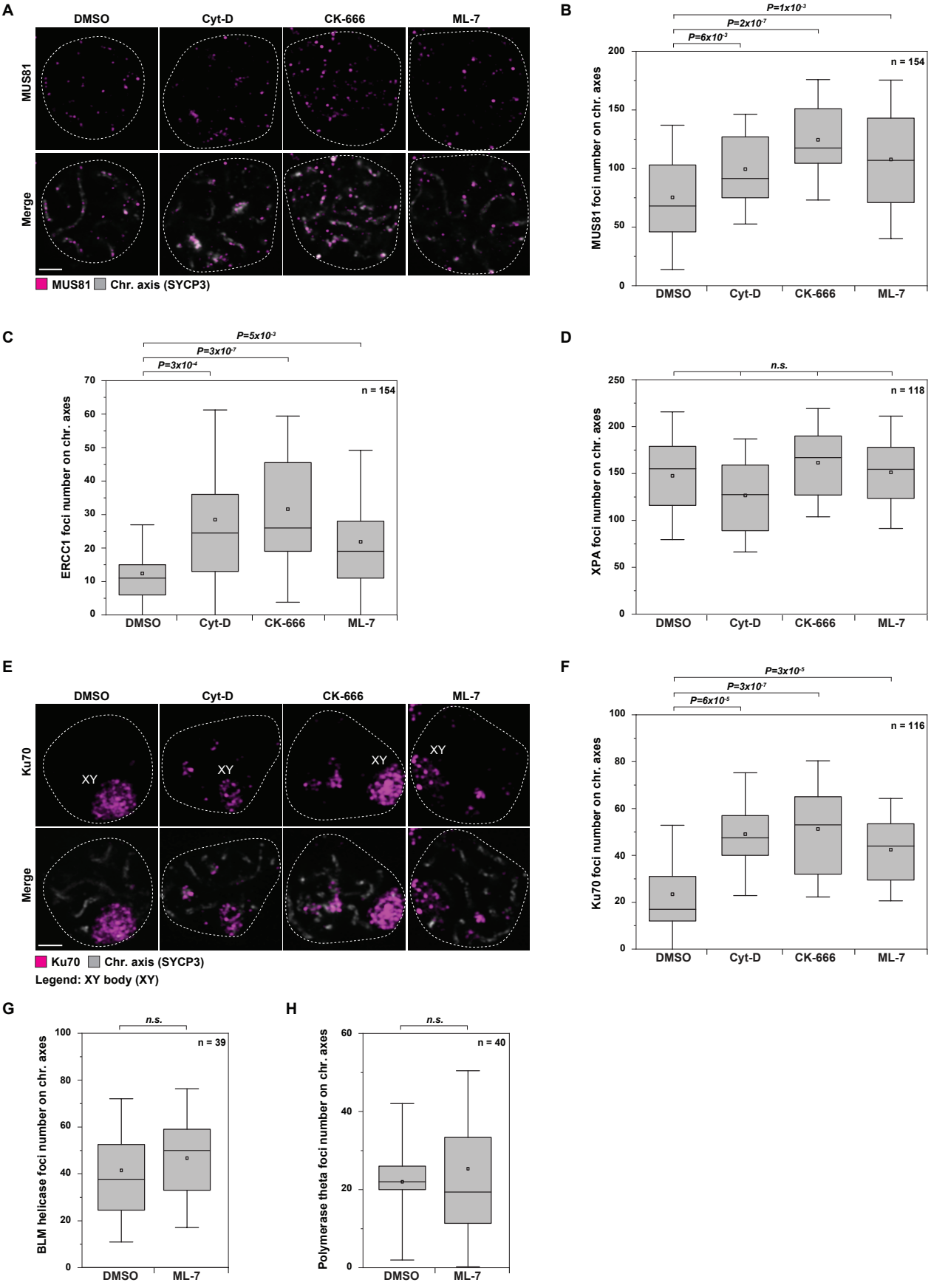
A
DMSO
Cyt-D
CK-666
ML-7
MUS81
Merge
MUS81 Chr. axis (SYCP3)
B
P=1x10-3
P=2x10-7
P=6x10-3
n = 154
MUS81 foci number on chr. axes
DMSO
Cyt-D
CK-666
ML-7
C
P=5x10-3
P=3x10-7
P=3x10-4
n = 154
ERCC1 foci number on chr. axes
D
n.s.
n = 118
XPA foci number on chr. axes
E
Ku70
XY
Merge
Ku70 Chr. axis (SYCP3)
Legend: XY body (XY)
F
P=3x10-5
P=3x10-7
P=6x10-5
n = 116
Ku70 foci number on chr. axes
G
n.s.
n = 39
BLM helicase foci number on chr. axes
H
n.s.
n = 40
Polymerase theta foci number on chr. axes

2.3.11. Actin, ARP2/3, and nm-myosin IIB are required for efficient progression from prophase to metaphase I

At least one inter-homolog crossover must be installed between each pair of homologous chromosomes during prophase (Jagielio and Fang, 1987; Polani, 1972). Defects in either homologous chromosome synapsis or recombination can lead to insufficient crossover installation (Dai et al., 2017; Kneitz et al., 2000; Pittman et al., 1998; Shi et al., 2019; De Vries et al., 2005, 1999; Yoshida et al., 1998). Such defects in synapsis or recombination can be detected by the pachytene checkpoint and if not resolved the germ cell can be eliminated through apoptosis (described in further detail in chapter 1). However, germ cells with insufficient inter-homolog crossovers can escape checkpoint control and enter metaphase I. Homologous chromosomes with insufficient crossovers can prematurely dissociate before segregation and can be detected as univalent chromosomes during metaphase I (Eaker et al., 2002; Holloway et al., 2008; Lipkin et al., 2002).

The reduction in class I crossover proteins along chromosome axes following perturbations of actin components (Fig. 12) might result in less inter-homolog crossovers being installed. On the other hand, MUS81/EME1 (Holloway et al., 2008) and XPF/ERCC1 could compensate in inter-homolog crossover formation (Fig. 13B, 13C). To investigate if perturbations of actin components affect inter-homolog crossover formation, I analyzed whether univalent chromosomes are detected following maturation of spermatocytes into metaphase I. To this end, spermatocytes were treated with either Cyt-D, CK-666, or ML-7 from leptotene to late pachytene and then induced into metaphase I through transient treatment with okadaic acid (Fig. 14A). Okadaic acid inhibits protein phosphatases 1 and 2A (PP1 and PP2A, respectively) and forces maturation of cells into metaphase I through CDK1/Cyclin B activity (Takai et al.,

1992; Wiltshire et al., 1995). Following either Cyt-D, CK-666, or ML-7 treatments, I found that spermatocytes can mature from pachytene into later stages of prophase (diplotene and diakinesis) (Fig. 14B). However, maturation into metaphase I is reduced following either CK-666 or ML-7 treatment compared to DMSO (Fig. 14B). Furthermore, maturation into metaphase I is completely abolished following either Cyt-D treatment (Fig. 14B), or after treatment with all three drugs (Cyt-D, CK-666, and ML-7) (Fig. 14C). This suggests that progression from prophase to metaphase I is impeded when actin components are perturbed.

While the number of spermatocytes entering metaphase I are reduced after treatment with either CK-666 or ML-7, no chromosomal defects could be detected. Notably, univalent chromosomes are not detected in either CK-666 or ML-7 treated cells that mature into metaphase I (Fig. 14D). This indicates that a sufficient number of inter-homolog crossovers can still be installed when either ARP2/3 or nm-myosin IIB are perturbed alone. In addition, the morphology of metaphase I chromosomes also appears normal following either CK-666 or ML-7 treatments, with SYCP3 primarily detected at the centromeres while Rec8-containing cohesin complexes are detected along both the chromosomal arms and centromeres, similar to DMSO treated cells (Fig. 14D). Together, these results reveal that when actin components are perturbed the number of cells progressing from pachytene to metaphase I are reduced, but those spermatocytes that do progress to metaphase I successfully generate inter-homolog crossovers.

Figure 14: Efficient progression from prophase to metaphase I is impeded when actin components are perturbed. Shown on next page. (A) Schematic of 11 days post-partum (dpp) mouse testes culture to study the effect of perturbing actin components from leptotene to late pachytene before maturation into metaphase I. (B) Quantification of the proportion of spermatocytes in different meiotic stages following treatments with drugs (Cyt-D, CK-666, or ML-7) or vehicle (DMSO). One experimental replicate presented. (C) Quantification of the proportion of spermatocytes in different meiotic stages following triple drug treatment (Cyt-D, CK-666, and ML-7) or vehicle treatment (DMSO). One experimental replicate presented. (D) Representative images of metaphase I chromosomes and the localization of SYCP3 and REC8 along chromosomes following treatments with drugs (CK-666, or ML-7) or vehicle (DMSO). Boxes highlight examples of bivalent chromosomes and are magnified in images below. Scale bar, 10 μm. n is the number of spermatocytes analyzed.

Figure 14

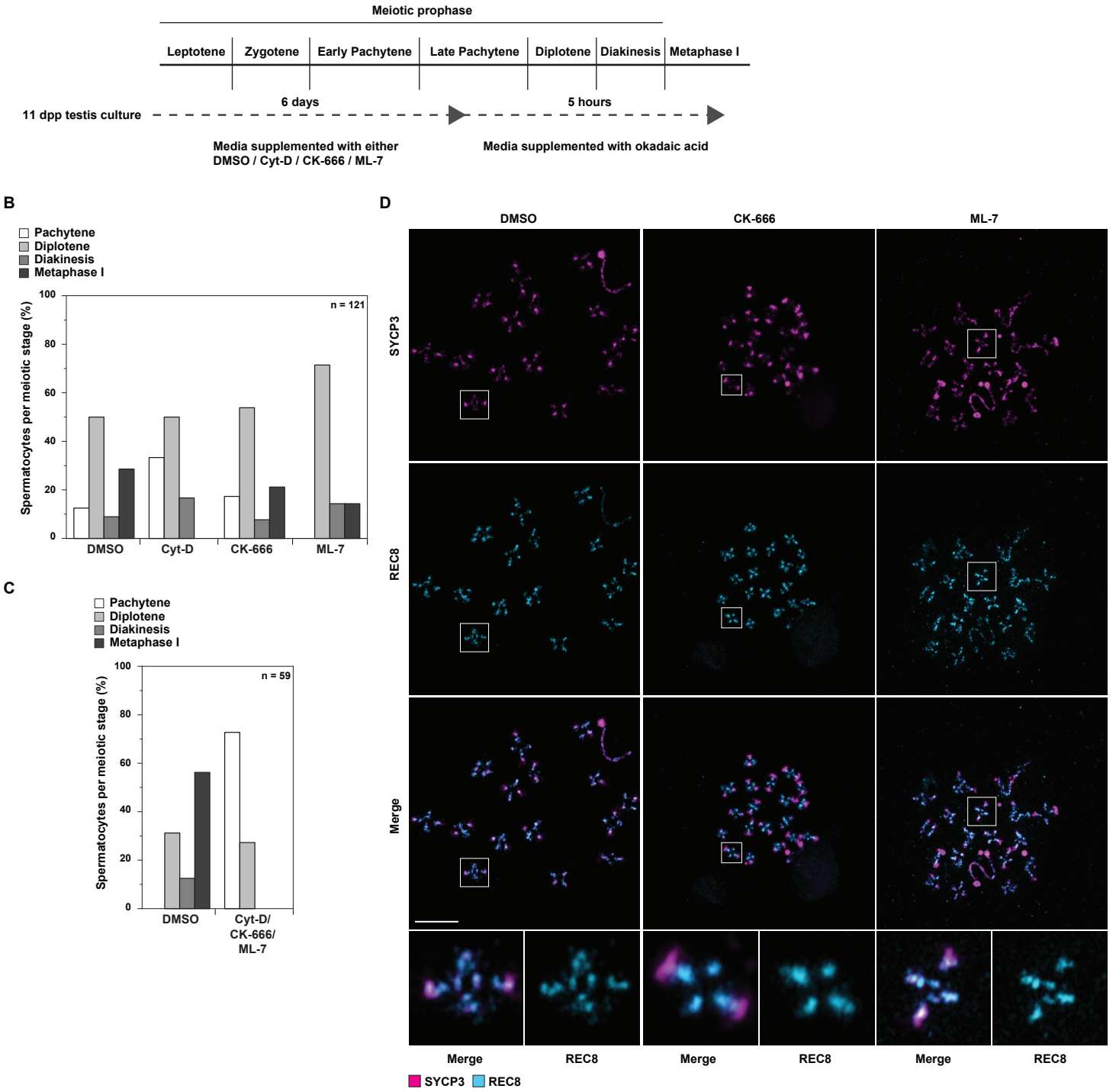
A
Meiotic prophase
Leptotene
Zygotene
Early Pachytene
Late Pachytene
Diplotene
Diakinesis
Metaphase I
6 days
5 hours
11 dpp testis culture
Media supplemented with either DMSO / Cyt-D / CK-666 / ML-7
Media supplemented with okadaic acid
B
Pachytene
Diplotene
Diakinesis
Metaphase I
Spermatocytes per meiotic stage (%)
n = 121
DMSO
Cyt-D
CK-666
ML-7
C
Pachytene
Diplotene
Diakinesis
Metaphase I
Spermatocytes per meiotic stage (%)
n = 59
DMSO
Cyt-D/ CK-666/ ML-7
D
DMSO
CK-666
ML-7
SYCP3
REC8
Merge
Merge
REC8
Merge
REC8
Merge
REC8
SYCP3
REC8

Figure 15. Graphical summary. Shown on next page. Actin, the ARP2/3 complex, and nm-myosin IIB (collectively referred to as actin components) localize along chromosome axes during mammalian meiotic prophase. Along the chromosome axes, the actin components also associate with a subset of HR nodules (represented by yellow RPA circles). The actin components facilitate in the alignment and synapsis of maternal (depicted in pink) and paternal (depicted in blue) homologous chromosomes. In addition, the actin components promote the localization of specific proteins to homologous recombination nodules, including RPA, RAD51 (not shown), and class I crossover (CO) proteins (shown as green circles). Through these two functions, actin components facilitate the repair of DNA double-strand breaks (DSBs) through the class I crossover pathway of homologous recombination. Note that the class I and class II crossover pathways can produce chiasmata. In this wild-type example, three chiasmata can be produced but only two chiasmata are depicted as the chiasmata produced by the class I and class II crossover pathways are closely situated (depicted as joint arrow). If actin components are perturbed, less actin components localize along chromosome axes and at HR nodules. In this situation, homologous chromosomes fail to align correctly, preventing the full extension of the synaptonemal complex along chromosome axes. This leads to asynapsis of homologous chromosomes. In addition, RPA, RAD51, and class I crossover proteins are reduced along chromosome axes. Consequently, a subset of DSBs cannot be repaired by the class I crossover pathway and are shunted into either the class II crossover (CO) pathway or the NHEJ pathway for repair (one example of an unrepaired DSB is shown). The SDSA pathway continues to repair DSBs even when actin components are perturbed. In asynapsed chromosomal regions, the SDSA and class II crossover pathways likely repair DSBs using the DNA template found in the sister chromatid. In synapsed chromosomal regions, the SDSA, class I crossover, and class II crossover pathways likely repair DSBs using the DNA template found in the homologous chromosome. As full homologous chromosome synapsis is impeded when actin components are perturbed, there is likely a reduced number of chiasmata installed per pair of homologs (as depicted). Chr. is an abbreviation of chromosome.

Figure 15

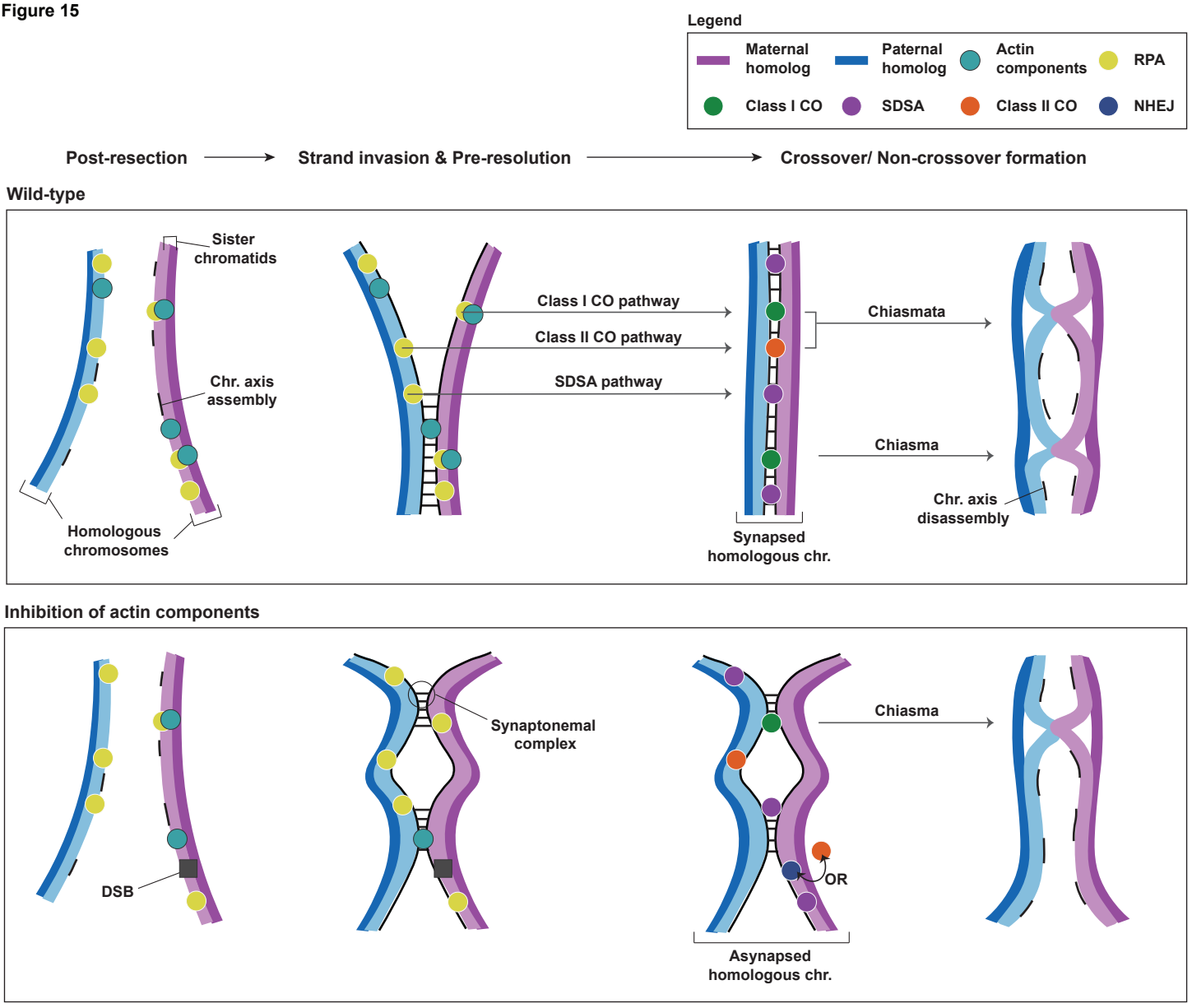
Legend
Maternal homolog
Paternal homolog
Actin components
RPA
Class I CO
SDSA
Class II CO
NHEJ
Post-resection
Strand invasion & Pre-resolution
Crossover/ Non-crossover formation
Wild-type
Sister chromatids
Chr. axis assembly
Homologous chromosomes
Class I CO pathway
Class II CO pathway
SDSA pathway
Synapsed homologous chr.
Chiasmata
Chiasma
Chr. axis disassembly
Inhibition of actin components
DSB
Synaptonemal complex
Chiasma
OR
Asynapsed homologous chr.

2.4.0. Discussion

During meiotic prophase, inter-homolog crossovers are generated between pairs of homologous chromosomes. These crossovers form chiasmata, which are necessary for chromosome segregation in the final stages of gamete maturation. Failure to form inter-homolog crossovers, leads to the production of inviable gametes (Di Giacomo et al., 2005; Hamer et al., 2008; Li and Schimenti, 2007; Pacheco et al., 2015; Rinaldi et al., 2017). Both synapsis and recombination of homologous chromosomes are required during meiotic prophase for the formation of inter-homolog crossovers. By identifying novel components involved in homologous chromosome synapsis and recombination we can better understand the factors that contribute to fertility. I find here that actin, the ARP2/3 complex, and nm-myosin IIB facilitate both homologous chromosome synapsis and recombination during mammalian meiotic prophase. These three actin components were previously not reported in the nuclei of mammalian germ cells, nor were they known to have essential functions during meiotic prophase. In addition, my data indicates that these nuclear actin components likely function in the class I crossover pathway of homologous recombination. Perturbations of actin components impair the localization of class I crossover proteins along chromosome axes (Fig. 12) and lead to an increase in factors that perform compensatory roles, including proteins involved in the class II crossover and NHEJ pathways (Fig. 13). As the majority of inter-homolog crossovers are generated through the class I crossover pathway in mammalian germ cells (Holloway et al., 2008, 2011), my findings reveal a novel and essential role for nuclear actin components in inter-homolog crossover formation.

2.4.1. Actin, ARP2/3, and nm-myosin IIB localize along chromosome axes

I identified actin, ARP2/3, and nm-myosin IIB in the nucleus during mouse male meiotic prophase where they are recruited to chromosome axes from leptotene stage. While actin associates with chromosome axes until diplotene, both ARP2/3 and nm-myosin IIB disassemble from axes during pachytene (Fig. 4D). In addition, I found that nuclear actin can be detected during meiotic prophase using antibodies that label both monomeric and polymeric actin (Fig. 5A-C). In contrast, nuclear actin is not detected with fluorescently labelled phalloidin, indicating that nuclear actin does not assemble into filamentous actin structures similar to those present in the cytoplasm (Fig. 5D). These results are in accordance with previous investigations in somatic and non-mammalian meiotic cells (Kelpsch and Tootle, 2018). Furthermore, the detection of nuclear actin with anti-Actin 2G2 and anti-Actin 1C7 antibodies (Fig. 5B, 5C) indicates that anti-parallel actin dimers are present in the nucleus during meiotic prophase, matching observations in somatic cells (Schoenenberger et al., 2005). Investigations using electron microscopy could further reveal whether polymerized actin is in the form of actin oligomers and/or actin rods in mammalian spermatocyte nuclei.

In addition to nm-myosin IIB, I also identified other myosins that localize to chromosome axes during meiotic prophase, namely nm-myosin IIA, myosin Iβ, and myosin VI (Fig. 6A-D). Further investigations are required to determine whether these myosins also function alongside actin, ARP2/3, and nm-myosin IIB during meiotic prophase.

2.4.2. Actin components facilitate homologous chromosome alignment and synapsis

I discovered that nuclear actin, ARP2/3, and nm-myosin IIB promote the alignment of homologous chromosomes during zygotene (Fig. 9E-H). I also found that these actin components facilitate the installation and extension of SYCP1 along homologous chromosome

axes (Fig. 9B, 10B). Through these functions, the actin components influence the downstream synapsis of homologous chromosomes. As ML-7 impedes the activation of all myosin II isoforms and not solely nm-myosin IIB (Krakup et al., 1998; Saitoh et al., 1987), it is possible that nm-myosin IIA (and potentially other isoforms) also assist in these actin-dependent functions.

Homologous chromosome alignment and synapsis is facilitated through the induction of rapid chromosome movements (Ding et al., 2007; Shibuya et al., 2014a, 2015). It should be noted that while cytoplasmic microtubules are involved in inducing rapid chromosome movements in mammalian germ cells, cytoplasmic actin is not required (Lee et al., 2015; Shibuya et al., 2014b). I hypothesize that rapid chromosome movements and nuclear actin components function together to promote the alignment and synapsis of homologs. Rapid chromosome movements likely bring homologous chromosomes into close proximity, which then enables ARP2/3 nucleated actin structures located on one chromosome axis to extend towards the axis of the other homologous chromosome. Following this, nm-myosin IIB can generate tension along the actin structures that bridge homologous chromosomes. I anticipate that together these molecular processes induce and maintain chromosome alignment before SYCP1 installment is complete. Epistatic analyses could be conducted in the future to determine whether actin components function downstream of rapid chromosome movements, as predicted.

2.4.3. Actin, ARP2/3, and nm-myosin IIB localize to a subset of HR nodules where they promote DSB repair through the class I crossover pathway

I found that actin components localize to a subset of HR nodules situated along chromosome axes between leptotene and pachytene. Specifically, the actin components associate with a mean of 7.5% of HR nodules during leptotene and 29.4% during pachytene (Fig. 4F). Similar observations were made in somatic cells, with 46% of HR nodules found to contain actin (Schrank et al., 2018). A central question is why actin components are recruited to only a subset of HR nodules. Perhaps these nodules are specified to a class I crossover pathway fate, while those HR nodules lacking actin components are repaired by alternative pathways (e.g. the SDSA pathway or the class II crossover pathway). Several factors may influence the recruitment of actin components to HR nodules, including the local chromatin environment, specific protein components, and/or post-translational modifications that influence the composition of HR nodules. In particular, the local environment surrounding specific DSB sites could enhance the recruitment of actin components to certain HR nodules instead of others. Indeed, proteins involved in DSB formation are selectively enriched at certain chromosome positions that contain mo-2 minisatellite DNA sequences (Acquaviva et al., 2020). Alternatively, specific components of HR nodules could assist in the recruitment of actin components. For example in somatic cells, ARP2/3 and myosins are recruited to HR nodules through MRE11, a component of the MRN complex, and SMC5/6, a cohesin complex (Caridi et al., 2018). My results indicate that actin components localize along chromosome axes before SMC5/6 (Fig. 4D), which is recruited during zygotene (Gómez et al., 2013; Hong et al., 2016; Hwang et al., 2018; Verver et al., 2014). In contrast, MRE11 is recruited to HR nodules during leptotene (Chapman and Jackson, 2008; Lukas et al., 2004; Stewart et al., 2003; Stucki et al., 2005), similar to when I detect actin components localizing to HR nodules. Therefore,

MRE11 is one candidate that could contribute in the recruitment of actin components to HR nodule. Post-translational modifications may represent a third method by which proteins can be recruited to HR nodules. ATM and ATR kinases phosphorylate numerous proteins in response to DSBs, of which many are recruited to chromosomes axes (Barchi et al., 2005; Bellani et al., 2005). Notably, the heavy chain of nm-myosin IIB (NM-HCIIB encoded by *MYH10*) is predicted to be a target for ATM/ATR phosphorylation (Matsuoka et al., 2007). Therefore, post-translational modifications of actin components might also facilitate in axis recruitment.

The question remains as to what functions the actin components perform once recruited to HR nodules. I found that actin, ARP2/3, and nm-myosin IIB localize to HR nodules during post-resection, strand invasion, and pre-resolution stages of homologous recombination (Fig. 7). In addition, I observed that actin components promote the axis localization of RPA, RAD51, and proteins specific to the class I crossover pathway, including MSH-4/MSH-5, and MLH-1/MLH-3 (Fig. 11B, 11D, 12). In contrast, the axis localization of proteins involved in either the class II crossover pathway (MUS81) or the SDSA pathway (BLM helicase) are not reduced when actin components are inhibited (Fig. 13B, 13G). As BLM helicase functions in the SDSA, class I, and class II crossover pathways (Jessop and Lichten, 2008; De Muyt et al., 2012; Rogacheva et al., 2014; Zakharyevich et al., 2012), further investigations using alternative markers (e.g. Top3) are required to verify whether actin components are involved in the SDSA pathway or not. Nevertheless, these findings do suggest that actin components facilitate the class I crossover pathway of homologous recombination.

It could be argued that the reduction in axis localization of class I crossover proteins is the result of impaired chromosomal alignment and synapsis, a phenotype previously observed in

asynaptic mutant mice (Ding et al., 2007; Shibuya et al., 2014a, 2015; De Vries et al., 2005). However, both RPA and RAD51 persist along chromosome axes in asynaptic mutant mice (Shibuya et al., 2014a; De Vries et al., 2005). I observe that when actin components are perturbed the axis localization of RPA and RAD51 is reduced (Fig. 11B, 11D). This suggests that actin components perform distinct functions in both homologous chromosome synapsis and in recombination. Potentially, actin components localizing along chromosome axes could function in two ways: first, they could promote global chromosome synapsis; and second, the subset of actin components localizing to HR nodules could facilitate recombination.

Actin components may perform several functions at HR nodules to facilitate the class I crossover pathway, such as aiding in the recruitment or stability of proteins to HR nodules, and/or performing structural functions in stabilizing intermediate DNA structures. Indeed, functions in either of these processes would explain the observed reduction in axis localization of RPA, RAD51, MSH-4/MSH-5, and MLH-1/MLH-3 when actin components are inhibited (Fig. 11B, 11D, 12). In particular, actin components may stabilize DNA structures during strand resection, strand invasion, and pre-resolution stages of homologous recombination. Indeed, in somatic cells ARP2/3 nucleated actin polymers assist in strand resection by inducing ssDNA motility (Schrank et al., 2018). During meiosis, I found that actin components associate with RPA at HR nodules after strand resection (Fig. 7E, 7F, 7J). Interestingly, RPA can recruit proteins that function with the MRN complex to induce further strand resection, generating longer ssDNA overhangs (Chen et al., 2013; Nimonkar et al., 2011). Therefore, it is possible that similar to somatic cells, actin components facilitate further strand resection during meiosis. Theoretically, actin polymers protruding from a single chromosome axis might also assist in guiding RAD51-coated ssDNA to the axis of the other homologous chromosome during strand

invasion. Live-cell imaging studies of spermatocytes could help to determine whether actin components induce ssDNA mobility during meiosis.

2.4.4. DSBs are shunted into the class II crossover pathway and the NHEJ pathway when actin components are perturbed

When the functions of either actin, the ARP2/3 complex, or nm-myosin IIB are impeded the class I crossover pathway is unable to repair a subset of DSBs (Fig. 12). In these situations, unrepaired DSBs appear to be shunted into the class II crossover pathway and the NHEJ pathway for repair, given the increased localization of factors specific to these pathways (Fig. 13B, 13F). In contrast, other DSB pathways including the SDSA pathway and the TMEJ pathway are not utilized in a compensatory DSB repair role (Fig. 13G, 13H). In addition, my results indicate that XPF/ERCC1 may function with the class II crossover heterodimer MUS81/EME1 in DSB repair through crossover formation (Fig. 13C). This is the first time that XPF/ERCC1 has been observed to function in mammalian meiotic recombination, though similar observations have been made during DSB repair in somatic cells and in *C.elegans* meiotic germ cells (Agostinho et al., 2013; Kikuchi et al., 2013; O'Neil et al., 2013).

My results indicate that increased activity of the class II crossover and the NHEJ pathways ensure that DSBs are repaired during meiotic prophase when the class I crossover pathway is impaired. This may reflect on a pre-existing compensatory role that these pathways play when class I crossover failure occurs (Holloway et al., 2008; Macaisne et al., 2018; Smolikove et al., 2007; Yin and Smolikove, 2013). I predict that MUS81/EME1 and XPF/ERCC1 cannot compensate in inter-homolog crossover formation. Instead, I anticipate that these endonucleases resolve DSBs as inter-sister crossovers. This is likely given that the localization

of RAD51 along axes is reduced when actin components are perturbed (Fig. 11D), as RAD51 is necessary for inter-homolog strand invasion but not inter-sister strand invasion (Schwacha and Kleckner, 1997). Therefore, I anticipate that inter-homolog crossovers are generated through the class I crossover pathway when actin components are perturbed, albeit at only a small number of DSB sites (Fig. 15).

I expect that defects in both chromosome synapsis and inter-homolog crossover formation are the most severe when either actin or all three actin components (actin, ARP2/3, and nm-myosin IIB) are perturbed. In these situations, defective germ cells are likely eliminated through the pachytene checkpoint or spindle assembly checkpoint (during prometaphase I), preventing entry into metaphase I (Fig. 14B, 14C). In contrast, the combined defects in chromosome synapsis and inter-homolog crossover formation are likely to be less severe when either ARP2/3 or nm-myosin IIB are inhibited alone, enabling a number of spermatocytes to progress into metaphase I (Fig. 14B).

At least one inter-homolog crossover is installed along each pair of homologs when either ARP2/3 or nm-myosin IIB are inhibited (Fig. 14D). It will be interesting to explore whether the crossover positions between chromosomes are altered following actin perturbations. Potentially, mechanisms that regulate crossover formation may alter the chromosomal positions where MLH-1/MLH-3 induce obligate crossovers when class I crossover proteins are reduced. Indeed, the chromosomal locations where MLH-1/MLH-3 are installed is not strictly set since MLH-1/MLH-3 can induce crossovers at additional DSB sites when the SDSA pathway is disrupted (Holloway et al., 2010).

2.4.5. Actin components influence meiotic progression: implications for human fertility

Finally, an interesting line of future research will be to determine whether the roles of actin components identified in male murine meiosis are conserved in female murine meiosis, and further, whether these findings translate to human meiosis. If actin, ARP2/3, and nm-myosin IIB also facilitate prophase events during human meiotic prophase, actin-targeting drugs should be used cautiously in humans as they may reduce fertility. Actin-targeting drugs are used to treat fungal infections (Usui, 2007) and have potential therapeutic uses in treating cancer (Foerster et al., 2014; Pfitzer et al., 2019) and in treating methamphetamine addictions (Young et al., 2015, 2016, 2017). Actin-targeting drugs could transiently reduce fertility in human males. However, male fertility levels should restore to normal levels when treatment with actin-targeting drugs is complete, owing to the continuous cycles of spermatogenesis (Bellve et al., 1977). In contrast, oocytes progress through a single cycle of meiotic prophase during embryogenesis (Hartshorne, 2013). Therefore, transient use of actin-targeting drugs during the first and second trimesters of pregnancy, correlates to the stage of meiotic prophase in female embryos, could permanently affect the fertility of the developing female.

2.4.6. Summary

In this chapter of my dissertation, I identify novel roles for actin, the ARP2/3 complex, and nm-myosin IIB during mammalian meiotic prophase. I discovered that these actin components are present in the nucleus during mammalian meiotic prophase where they localize along chromosome axes to facilitate the alignment and synapsis of homologous chromosomes (Fig. 15). Actin components also localize to a subset of HR nodules along chromosome axes where they promote the localization of proteins involved in the class I crossover pathway (Fig. 15). The roles of actin components in both chromosome synapsis and recombination ensure that

a subset of DSBs are repaired as inter-homolog crossovers (Fig. 15). As a consequence, efficient maturation from prophase into later stages of meiosis can be achieved. This is the first time that a role for nuclear actin, ARP2/3, and nm-myosin IIB in mammalian meiotic recombination has been identified. It will be interesting in the future to explore whether defects in actin functions contribute to unexplained infertility problems in humans.

Chapter 3: Live-cell imaging of fetal oocytes and homologous chromosome pairing

3.1.0. Introduction

In the final section of my dissertation I will present an overview of the current knowledge regarding how homologous chromosomes pair during mammalian meiosis. In addition, I describe current methods that can be utilized to image live mammalian germ cells expressing exogenous fluorescently tagged protein reporters. Finally, I present my work towards investigating chromosome pairing in female germ cells, and the development of a new method for studying female germ cells through live-cell imaging.

3.1.1. Homologous chromosome pairing

Homologous chromosome pairing is essential for successful meiosis. Indeed, the processes of homologous chromosome synapsis and recombination begin with the pairing of each duo of homologous chromosomes, and in turn promote the generation of chiasmata (described in further detail in chapter 1). Yet, how two homologous chromosomes can search the nucleoplasm to find each other while not engaging with incorrect chromosomes throughout mammalian meiosis remains unclear. Microtubule-driven forces induce rapid chromosome movements in the nucleus, while chromosomal bouquet formation can facilitate the clustering of chromosomes during meiosis (described in further detail in chapter 1) (Ding et al., 2007; Horn et al., 2013; Lee et al., 2015; Link et al., 2014; Morimoto et al., 2012; Pfeifer et al., 2001, 2003; Scherthan et al., 1996; Shibuya et al., 2015, 2014b, 2014a; Tankimanova et al., 2004). These processes bring chromosomes in close proximity and allow chromosomes to search for their homologs through transient interactions between chromosomes. However, microtubule-driven forces and chromosomal bouquet formation alone are insufficient to

initiate pairing of chromosomes (Ding et al., 2007; Shibuya et al., 2014a, 2015). Other mechanisms likely play a role in promoting homolog recognition and preventing erroneous pairing of non-homologous chromosomes. As described in detail in chapter 1, RAD51/DMC1-mediated strand invasion can promote the pairing and alignment of homologous chromosomes (Kauppi et al., 2013; Rockmill et al., 1995). However, strand invasion can occur after chromosome pairing during mammalian meiosis. Therefore, other undefined processes are likely to drive homolog recognition during mammalian meiosis.

Non-mammalian organisms utilize a variety of strategies to regulate homologous chromosome pairing. Indeed, homolog pairing is initiated by the coupling of chromosome-specific proteins (e.g. *C.elegans*), or through interactions between RNA and RNA binding proteins (e.g. *S.pombe*) with specific DNA sequences within chromosomes termed 'pairing centers'. Pairing centers are uniquely located on each homologous chromosome (Ding et al., 2012, 2019; Phillips and Dernburg, 2006; Phillips et al., 2009). In both cases DNA sequences act as 'barcodes' that enable the unique identification of homologous chromosomes and initiate pairing during meiosis. Whether similar mechanisms also operate during mammalian meiosis remains an interesting open question. To investigate this, it would first be useful to determine the chromosomal regions where mammalian chromosomes begin to pair. From here, it could then be explored whether these chromosomal regions contain conserved pairing centers.

3.1.2. Chromosome pairing proceeds differently in male and female meiosis

The process of homologous chromosome pairing proceeds at different stages for male and female meiosis in mammals. Chromosome pairing in male meiosis occurs between pre-

leptotene and zygotene stages of prophase (4.5 days in total) (Boateng et al., 2013; Ishiguro et al., 2014; Scherthan and Schönborn, 2001; Scherthan et al., 1996, 1998). In contrast, chromosome pairing occurs throughout a longer breadth of stages between leptotene and pachytene during female meiosis (6 days in total) (O'Keeffe et al., 1997; Tankimanova et al., 2004). In general, chromosome pairing occurs in an asynchronous manner, with shorter chromosomes believed to pair before longer chromosomes (Scherthan and Schönborn, 2001). However, there does not appear to be conservation between male and female meiosis in the chromosomal location where pairing is initiated between homologous chromosomes. In meiosis of mammalian males, the initial pairing between homologs tends to occur at either the proximal (closest to centromere) or distal ends of chromosomes but infrequently within intra-chromosomal (interstitial) regions (Boateng et al., 2013; Pfeifer et al., 2001; Scherthan et al., 1996). Yet, in female mammalian meiosis, homolog pairing rarely commences at the proximal chromosomal end (O'Keeffe et al., 1997). Instead, pairing in mammalian females occurs largely at the distal end or the distal interstitial region (an intra-chromosomal region closer to the distal end than the proximal end) of chromosomes (O'Keeffe et al., 1997; Pfeifer et al., 2003; Speed, 1982; Tankimanova et al., 2004). These findings indicate that chromosome pairing is not initiated at random chromosomal regions, albeit the chromosomal region can differ between male and female meiosis. These findings also highlight the possibility of several pairing centers along mammalian chromosomes, which may behave differently between male and female germ cells in the context of meiosis. However, the precise chromosomal locations where pairing commences along each chromosome still remains unknown and would be important to define to further investigate the possibility of mammalian pairing centers.

3.1.3. Investigating where pairing is initiated between specific homologous chromosomes

Pairing of homologous chromosomes can be visualized in intact germ cells through fluorescent in situ hybridization (FISH) assays (Boateng et al., 2013; Ishiguro et al., 2014; Scherthan et al., 1996, 1998; Tankimanova et al., 2004). These assays involve staining cells with fluorescent DNA probes that label specific DNA sequences found in maternal and paternal homologous chromosomes. In each cell, four signals are observed, with each signal arising from identical sequences within the four sister chromatids. Though, since each homologous chromosome is composed of two sister chromatids, there are in fact two doublet signals detected inside each cell. Prior to pairing, the two doublet signals corresponding to each homologous chromosome are randomly distributed within the nucleoplasm. When FISH signals on maternal and paternal homologous chromosomes are within 1.35 μm of each other, then homolog pairing is considered to be complete (Boateng et al., 2013; Ishiguro et al., 2014). Through this method, it is possible to determine where pairing is first initiated along a specific chromosome. This can be achieved by labelling a pair of homologs with FISH probes that associate with different chromosomal regions (e.g. proximal, interstitial, and distal regions). I will describe in section 3.3.1 my results aimed at finding pairing centers in female mouse meiosis.

3.1.4. Studying meiotic prophase through live-cell imaging

Live-cell imaging of mammalian germ cells provides a more comprehensive understanding of how dynamic events such as chromosome pairing proceed over time. Indeed, fluorescently labelled protein reporters can be tracked in live mouse spermatocytes (Lee et al., 2015; Morelli et al., 2008; Shibuya et al., 2014b, 2015; Zhang et al., 2019). These investigations have elucidated events such as rapid chromosome movements and other dynamic processes in

meiosis. Fluorescent reporters are delivered into spermatocytes through transient transfection, which involves injecting and electroporating plasmid DNA into testes by surgical methods into live animals (Shibuya and Watanabe, 2018).

As female meiotic prophase occurs during fetal development, transient transfection through surgery is technically challenging. Nevertheless, plasmid DNA can be delivered into fetal oocytes through injection and electroporation of fetal ovaries *ex vivo* (Gao et al., 2011; Wang et al., 2016). While this technique is useful to track cells in the ovarian context, it may be inappropriate to investigate subcellular events during female meiotic prophase. Notably, fetal oocytes derived from transgenic mice expressing fluorescently tagged reporter proteins can be utilized for live-cell imaging (Enguita-Marruedo et al., 2018). However, the generation of transgenic mice is time-consuming and limits the number of proteins that can be fluorescently tagged and studied experimentally. Therefore, developing a method to directly introduce fluorescent reporters into isolated fetal oocytes would make live-cell imaging of fetal oocytes more accessible. In addition, fetal oocytes can be matured *ex vivo* throughout meiotic prophase by co-culturing fetal oocytes and somatic gonadal cells. This co-culture technique was successfully utilized in previous studies (Hayashi and Saitou, 2013; Hikabe et al., 2016). I anticipate that this culture method would increase the ease of conducting live-cell imaging of fetal oocytes. Through live-cell imaging, a more comprehensive understanding of the dynamic events that occur during female meiotic prophase can be gained.

3.1.5. Objectives

In the following sections, I present two experimental approaches that I developed to investigate chromosome dynamics during the pairing stage of female mammalian meiosis.

The first is a FISH-based method applied to chemically fixed cells to determine the chromosomal location where homologous chromosome pairing is initiated during female meiotic prophase. The second is a method to image live oocytes cultured *ex vivo* that transiently express fluorescent reporter proteins.

3.2.0. Experimental procedures

3.2.1. Animals

All mice were maintained in a specific pathogen-free environment according to animal ethics guidelines of the Animal Facility of the Max Planck Institute for Biophysical Chemistry. Pregnant female mice were sacrificed by cervical dislocation with the guidelines provided by the German Animal Welfare Act (German Ministry of Agriculture, Health, and Economic Cooperation). Female embryos were isolated from sacrificed pregnant females between 13.5 to 17.5 dpc (day of copulation plug = 0.5 dpc). Female embryos from CD1 mice and the transgenic line Rec8-eGFP were utilized.

3.2.2. Generating mouse embryonic fibroblast feeder cells

Mouse embryonic fibroblasts (NIH/3T3 cells) were cultured to confluency in MEMα (Thermofisher, 22571-020) supplemented with 10% (v/v) FBS (fetal bovine serum) (Thermofisher, 26140079), and 1% (v/v) penicillin-streptomycin (Gibco, 15140122). To generate feeder cells, confluent NIH/3T3 cells were cultured in media supplemented with 10 µg/ml mitomycin C (Merck, M4287-2MG) for 2 hours at 37°C with 5% carbon dioxide in air. Following this, cells were washed with Dulbecco's PBS (Thermofisher, 14190144) and were removed from culture dishes using trypsin-EDTA (0.25%) (Thermofisher, 25200056). After

centrifugation at 500 × *g* for 5 minutes at room temperature, cells were re-suspended in culture media supplemented with 10% (v/v) DMSO. Aliquots of feeder cells were stored in liquid nitrogen. 24 hours before fetal oocyte culture, an aliquot of feeder cells was thawed and plated in an 8 well dish (Thermofisher, 155411) at a density of 1 x 10^4 cells/ml. Cells were cultured at 37°C with 5% carbon dioxide in air in culture media described above.

3.2.3. Transfection of fetal oocytes

Fetal ovaries were dissected from CD1 embryos aged between 13.5 and 16.5 dpc. Ovaries were disaggregated through gentle mincing and treatment with Accumax (Stem cell technologies, 07921) for 5 minutes at 37°C. Accumax was neutralized through addition of an equal volume of 10% FBS (v/v)/ Dulbecco's PBS. Disaggregated ovarian cells were passed through a 35 µm strainer (Corning, 352235) before centrifugation at 500 × *g* for 10 minutes at 4℃. Following this, cells were either transfected through electroporation, lipofection, or inactivated-virus delivery. For electroporation, cells were re-suspended in Neon electroporation buffer (Thermofisher) to obtain between 5 x 10^4 to 2 x 10^5 cells per 10 µl. Plasmid DNA (1.25 µg) was added to 10 µl of cells before electroporation. Electric pulses were applied two times at 950 V for 30 ms using a Neon electroporator (Thermofisher, MPK1025). Lipofection was conducted using lipofectamine 3000 (Thermofisher, L3000001). Inactivated-virus delivery was conducted using the GenomONE neo EX kit (Cosmo bio, ISK-GN-001-FZ). For lipofection or inactivated-virus delivery, cells were re-suspended in Opti-MEM (Thermofisher, 31985062) at a cell density according to manufacturer's instructions. DNA was combined with appropriate reagents and added to cells according to manufacturer's instructions.

3.2.4. Culture of transfected fetal oocytes

Transfected fetal ovarian cells were cultured in an 8 well dish (Thermofisher, 155411) at 37°C with 5% carbon dioxide in air in MEMα (Thermofisher, 22571-020) supplemented with 0.05% (w/v) ascorbic acid (TGI, G0394), and 2% (v/v) FBS (fetal bovine serum) (Thermofisher, 26140079). Expression of plasmids following various transfection techniques was analyzed through microscopy 24 hours post-transfection. After a specific transfection method was selected (electroporation with plasmids driven by the CMV promoter), optimization of cell culture was conducted. Fetal oocytes were cultured in either reconstituted ovaries or in a 2D-setup with feeder cells. Reconstituted ovaries were generated by combining 5,000 electroporated fetal ovarian cells with 50,000 non-transfected ovarian cells in a low binding U-bottom 96-well plate (Thermofisher, 174925) (similar to the method described by Hayashi and Saitou, 2013). Reconstituted ovaries were cultured in MEMα (Thermofisher, 22571-020) supplemented with 0.05% (w/v) ascorbic acid (TGI, G0394), and 2% (v/v) FBS (fetal bovine serum) (Thermofisher, 26140079). For the 2D-setup, mouse embryonic fibroblast feeder layers were seed (as described in section 3.2.2.) in an 8 well dish (Thermofisher, 155411) 24 hours before fetal oocyte transfection. Before transfection of fetal oocytes, the feeder cell culture media was changed as described below. If fetal oocytes were transfected through electroporation or inactivated-virus delivery, media was changed to MEMα (Thermofisher, 22571-020) supplemented with 0.05% (w/v) ascorbic acid (TGI, G0394), and 2% (v/v) FBS (fetal bovine serum) (Thermofisher, 26140079). If fetal oocytes were transfected through lipofection, media was changed to Opti-MEM (Thermofisher, 31985062). Reconstituted ovaries and 2D-cultures were incubated at 37°C with 5% carbon dioxide in air.

3.2.5. Plasmid preparation

Plasmids were isolated for transfection using a DNA plasmid midi kit (Qiagen, 12145) and solubilized in double-distilled water. The *Sycp3* mouse cDNA sequence was amplified from the BAC BC138509 (transomics). *Trf1* mouse cDNA sequence was amplified from pGEMHE-3EGFP-TRF1, a plasmid kindly provided by Jan Ellenberg. EF1α promoter was amplified from pVITRO1-MCS (InvivoGen, pvitro1-nmcs). The *Vasa* promoter was amplified from pVasa-Cre, a plasmid kindly provided by Diego Castrillon (addgene, 15885). The *Stra8* promoter was amplified from pStra8-eGFP, a plasmid kindly provided by Wolfgang Engel. The predicted *Meioc* promoter was amplified from a cDNA library produced from CD1 mouse testes. In brief, RNA was extracted from testes using TRIzol reagent (Thermofisher, 15596026) according to the manufacturer's instructions. cDNA synthesis was conducted using SuperScript IV (Thermofisher, 18091050) utilizing the Oligo d(T) primer according to the manufacturer's instructions. SYCP3 and TRF1 cDNA were cloned into pENTR-D-TOPO plasmids that utilize a directional Topoisomerase reaction (Invitrogen, K2400-20) (as described in table 5 and table 6). Expression plasmids were produced through LR clonase II reactions (Invitrogen, 11791-020) between appropriate pENTR plasmids and Gateway-Destination plasmids, according to the manufacturer's instructions (as described in table 5 and table 6). PCR amplifications were performed using Phusion HF polymerase (NEB, M0530S) according to manufacturer's instructions. Restriction digests and ligation reactions (NEB, M2200S) were performed according to manufacturer's instructions.

Table 5: List of plasmids generated.

Plasmid type	Plasmid name	Cloning method	Insert vector
Gateway plasmid	pCMV-mClover-Gateway	PCR, restriction digest (AvrII and PacI), and ligation	pSNAPf (NEB, N9183S)
Gateway plasmid	pEF1α-mClover-Gateway	PCR, restriction digest (NruI and PmeI), and ligation	pCMV-mClover-Gateway
Gateway plasmid	pStra8-mClover-Gateway	PCR, restriction digest (SpeI and BamHI), and ligation	pCMV-mClover-Gateway
Gateway plasmid	pMeioc-mClover-Gateway	PCR, restriction digest (SpeI and PmeI), and ligation	pCMV-mClover-Gateway
Gateway plasmid	pVasa-mClover-Gateway	PCR, restriction digest (NruI and PmeI), and ligation	pCMV-mClover-Gateway
pENTR plasmid	pENTR-SYCP3	PCR, TOPO reaction	pENTR D-TOPO
pENTR plasmid	pENTR-TRF1	PCR, TOPO reaction	pENTR D-TOPO
Expression plasmid	pCMV-mClover-SYCP3	LR clonase II reaction	pCMV-mClover-Gateway
Expression plasmid	pCMV-mClover-TRF1	LR clonase II reaction	pCMV-mClover-Gateway
Expression plasmid	pEF1α-mClover-SYCP3	LR clonase II reaction	pEF1α-mClover-Gateway
Expression plasmid	pStra8-mClover-SYCP3	LR clonase II reaction	pStra8-mClover-Gateway
Expression plasmid	pMeioc-mClover-SYCP3	LR clonase II reaction	pMeioc-mClover-Gateway
Expression plasmid	pVasa-mClover-SYCP3	LR clonase II reaction	pVasa-mClover-Gateway

Table 6: List of primers. The DNA sequence amplified is highlighted in bold.

Cloning step	Forward primer	Reverse primer
pENTR-**SYCP3**	CACCATGCTTCGAGGGTGTGGG	GAATAACATGGATTGAAGAGACTTTCGAACAT
pENTR-**TRF1**	CACCATGGCGGAGGATGTTTCCTCA	GTCTTCGCTGTCTGAGGAAATCAGTTTTAG
pCMV-**mClover-Gateway**	GACTTTAATTAAATGGTGAGCAAGGG CGAGGA	ACTGCCTAGGCTACTCGAGACCACTTTG TACAAGAAAGCTGAAC
pEF1α-mClover-Gateway	GACTTCGCGACCTGCAGGGCCTGAAA TAACC	GACTGTTTAAACTTGCTTTGAATTAGCGGTGGT TTTCAC
pStra8-mClover-Gateway	GACTACTAGTTGGAAACCCACAACGA AGGCC	GACTGGATCCGTCGCAGAATAAGAAGAGAGG CTCTTGC
pMeioc-mClover-Gateway	GACTACTAGTCTTAATCTGGTGAGGAA GGGCCCAGTGACTCTGGTCAG	GACTGTTTAAACGCCGTTACATTGCTCCCCGCG CCT
pVasa-mClover-Gateway	GACTTCGCGATGTGCCACCATGCCTGG CCCAGTTTC	GACTGTTTAAACTCTCCGCTCCAGGCTCCCCGG GCTCCT

3.2.6. FISH probe preparation

Bacterial artificial chromosomes (BACs) were purchased from BACPAC resources center (bacpacgenomics). BAC RP23-410L2 was used to label the distal interstitial region of mouse chromosome 7, while BAC RP23-101N20 was used to label the distal end of mouse chromosome 7. BACs were isolated for FISH labelling using Nucleobond BAC purification kit (Machery-Nagel, 740579). FISH probes were generated from BACs through nick translation (according to Bolland et al., 2013). FISH probes derived from BAC RP23-410L2 were labelled with Alexa Fluor-488 (Thermofisher, A20000) while those derived from BAC RP23-101N20 were labelled with Alexa Fluor-647 (Thermofisher, A20006) (according to Bolland et al., 2013).

3.2.7. Preparation of fetal oocytes for FISH labeling

Fetal ovaries were dissected from 5 to 10 CD1 mouse embryos aged between 14.5 and 17.5 dpc. Ovaries were minced in 1 × PBS to produce a cell suspension. Cells were passed through a 35 μm strainer (Corning, 352235) before centrifugation at 500 × *g* for 10 minutes at 4°C. Pelleted cells were re-suspended in 100 μl of 1 × PBS. 20 μl of the cell suspension was added to a defined region of each slide (Thermofisher, J4800AMNZ), marked using a pap pen (LS Bio, LS-J1048). Slides were incubated in a humidified chamber for 5 minutes. Following this, cells were fixed in 4% (v/v) methanol-free formaldehyde (Polysciences, 04018-1)/ 1 × PBS at room temperature for 5 minutes. Fixed cells were permeabilized in 0.1% (v/v) triton X-100/ 1 × PBS at room temperature for 10 minutes. Slides were washed twice in 1 × PBS before being transferred to 20% (v/v) glycerol/ 1 × PBS for 1 hour at room temperature. Following this, slides were stored in 50% (v/v) glycerol/ 1 × PBS at -20°C. To prepare slides for FISH labelling, slides were thawed in 20% (v/v) glycerol/ 1 × PBS for 5 minutes at room temperature followed by three rounds of freeze/thaw steps in liquid nitrogen. Slides were washed once in 1 × PBS

before incubation with 0.1 M HCL for 10 minutes at room temperature. Subsequently, slides were washed once in 1 × PBS before re-permeabilization in 0.05% (v/v) triton X-100/1 × PBS for 15 minutes at room temperature. Slides were then equilibrated in 50% (v/v) formamide/ 2 × SSC (saline-sodium citrate) for 2 hours at room temperature. Excess liquid was removed before addition of 10 µl of FISH probe mixture (containing RP23-410L2 labelled with Alexa Fluor-488 and RP23-101N20 labelled with Alexa Fluor-647). The region of the slide was then covered with a coverslip and sealed using rubber cement. Slides were incubated at 75°C for 5 minutes to denature the FISH probes and oocyte DNA. FISH probes were hybridized to oocyte DNA at 37°C overnight in a humidified chamber. Following this the coverslip was removed and slides were sequentially washed with 50% (v/v) formamide/ 2 × SSC at 45°C for 15 minutes, 0.2 × SSC at 63°C for 15 minutes, 2 × SSC at 45°C for 5 minutes, and finally with 2 × SSC for 5 minutes at room temperature.

3.2.8. Immunofluorescence of FISH-labelled fetal oocytes

Care was taken to avoid unnecessarily exposing slides to light following FISH labelling. Slides were washed in 1 × PBS and blocked for 1 hour at room temperature in 5% BSA (w/v) and 0.1% (v/v) triton X-100 in 1 × PBS (blocking buffer). Primary and secondary antibody solutions were prepared in blocking buffer. Cells were incubated with the primary antibody anti-SYCP3 (1:300. Abcam, Ab97672) at 4°C overnight. Slides were washed in 1 × PBS three times before incubation with the secondary antibody (Donkey anti-Mouse Alexa Fluor-568. 1:400. Invitrogen, A10037) and Hoechst solution (1:333 final concentration. Thermofisher, 62249) for 1 hour at room temperature. Slides were washed in 1 × PBS three times. 50% (v/v) glycerol in distilled water was added to slides before addition of coverslip (#1.5, VWR, 15165452).

3.2.9. Microscopy

Images were acquired with LSM 880 and LSM 800 confocal laser scanning microscopes (Zeiss) with a 63 × Plan-Apochromat 1.4 N/A oil-immersion objective. Airyscan images were acquired using the Airyscan module on the LSM800 and LSM880 confocal laser scanning microscopes (Zeiss) and processed in ZEN (Zeiss) after acquisition. Care was taken that the imaging conditions (laser power, pixel-dwell time, and detector gain) did not cause photobleaching or saturation. Fixed intact cells were imaged using Z-stacks at 0.3 µm distance to image entire fetal oocyte nuclei (approximately 55 slices).

3.2.10. Quantification of homologous chromosome pairing

Fetal oocyte nuclei were analyzed using the surface function of Imaris (Bitplane). FISH channels were masked to specifically analyze FISH signals. The coordinates of FISH signals within oocyte nuclei were collected using the spot function of Imaris software. The distance between two FISH signals (i.e. the two homologous chromosomes) was calculated using the equation $\sqrt{((X1-X2)^2 + (Y1-Y2)^2 + (Z1-Z2)^2)}$. FISH signals on the two homologous chromosomes and two sister chromatids could often be uniquely identified during analysis. In these situations, an average of the two coordinates of FISH signals on sister chromatids was used to measure the distance between FISH signals of homologous chromosomes. Regions along mouse chromosome 7 were considered paired when the FISH signals were ≤ 1.35 µm apart (as previously defined in mouse spermatocytes by Boateng et al., 2013; Ishiguro et al., 2014).

3.2.11. Statistical analysis

Statistical analyzes were performed using OriginPro. Statistical significance was based on unpaired, two-tailed Student's t test.

3.3.0. Results

3.3.1. Pairing of maternal and paternal chromosome 7 is initiated in the distal end

In mammalian female meiosis, pairing of homologous chromosomes is frequently initiated at either the distal interstitial region (an intra-chromosomal region close to the distal end) or the distal end of chromosomes (O'Keeffe et al., 1997; Pfeifer et al., 2003; Speed, 1982; Tankimanova et al., 2004). I aimed to narrow down the chromosomal region where pairing commences at specific chromosomes. For this purpose, I labelled maternal and paternal chromosome 7 with FISH probes that recognized the distal interstitial region (termed the interstitial region from here) and distal end of chromosome 7 (Fig. 16A). Notably, any chromosome could have been used in this study, however here chromosome 7 is used as an example.

I investigated chromosome pairing in structurally intact mouse fetal oocytes derived from 14.5 to 17.5 dpc fetal ovaries. This enabled the process of chromosome pairing to be tracked from leptotene (14.5 dpc) to pachytene (15.5 to 17.5 dpc) of meiotic prophase (Fig. 16B). These stages correspond to when pairing occurs in female meiosis (Borum, 1961; O'Keeffe et al., 1997; Pfeifer et al., 2003; Speed, 1982; Tankimanova et al., 2004). When the distance between maternal and paternal FISH probes was $\leq$ 1.35 µm, I considered the region of chromosome 7 as paired (Boateng et al., 2013; Ishiguro et al., 2014). As expected, at 14.5 dpc corresponding to leptotene, the interstitial regions and distal ends of maternal and paternal chromosome 7 are separated by a distance larger than 1.35 µm. In particular, the interstitial regions are a mean distance apart of 5.2 µm, while the distal ends are a mean distance apart of 4.1 µm (Fig. 16C, 16D). By contrast, at 16.5 dpc, the distal ends of maternal and paternal

chromosome 7 are a mean distance apart of 1.3 μm, and are thus considered as paired (Fig. 16C, 16D). While the distal ends become paired by 16.5 dpc, I found that the interstitial regions of maternal and paternal chromosome 7 are a mean of 1.86 μm apart at 16.5 dpc (Fig. 16C, 16D). The interstitial regions of chromosome 7 in some fetal oocytes may be paired at 16.5 dpc, yet the mean distance reported here reflects that most are not paired by 16.5 dpc. By 17.5 dpc, the interstitial regions are finally paired with a mean distance of 1.2 μm between the interstitial regions of maternal and paternal chromosome 7 detected (Fig. 16C, 16D). Together these results show that pairing of maternal and paternal chromosome 7 is complete by pachytene (17.5 dpc) in fetal oocytes, with the distal ends pairing before the interstitial regions.

Figure 16: Pairing of maternal and paternal chromosome 7 occurs first at the distal ends followed by the interstitial regions. Shown on next page. (A) Illustration of mouse chromosome 7 and the approximate chromosomal regions of FISH probes. (B) Schematic representation of mouse fetal oocyte progression through meiotic prophase. (C) Representative images of fetal oocytes from 14.5 to 17.5 dpc mouse fetal ovaries labelled with FISH probes specific for the interstitial regions and distal ends of maternal and paternal chromosome 7. Boxes denote the separate maternal and paternal homologous chromosomes (homologs) at 14.5 dpc. Between 15.5 and 17.5 dpc the homologs are close together. Circles highlight oocyte nuclei. Scale bar, 2 μm. (D) Quantification of the distance between FISH probes of homologous chromosomes in fetal oocytes from 14.5 to 17.5 dpc fetal ovaries. Three experimental replicates shown. For the quantification, mean (square), median (line), 25^{th} and 75^{th} quartiles (boxes) are shown along with the standard deviation. Dashed line depicts the distance between FISH probes when pairing is considered complete (1.35 μm). All P-values calculated using two-sided Student's t-test. n is the number of fetal oocytes analyzed. Chr. is an abbreviation of chromosome.

Figure 16

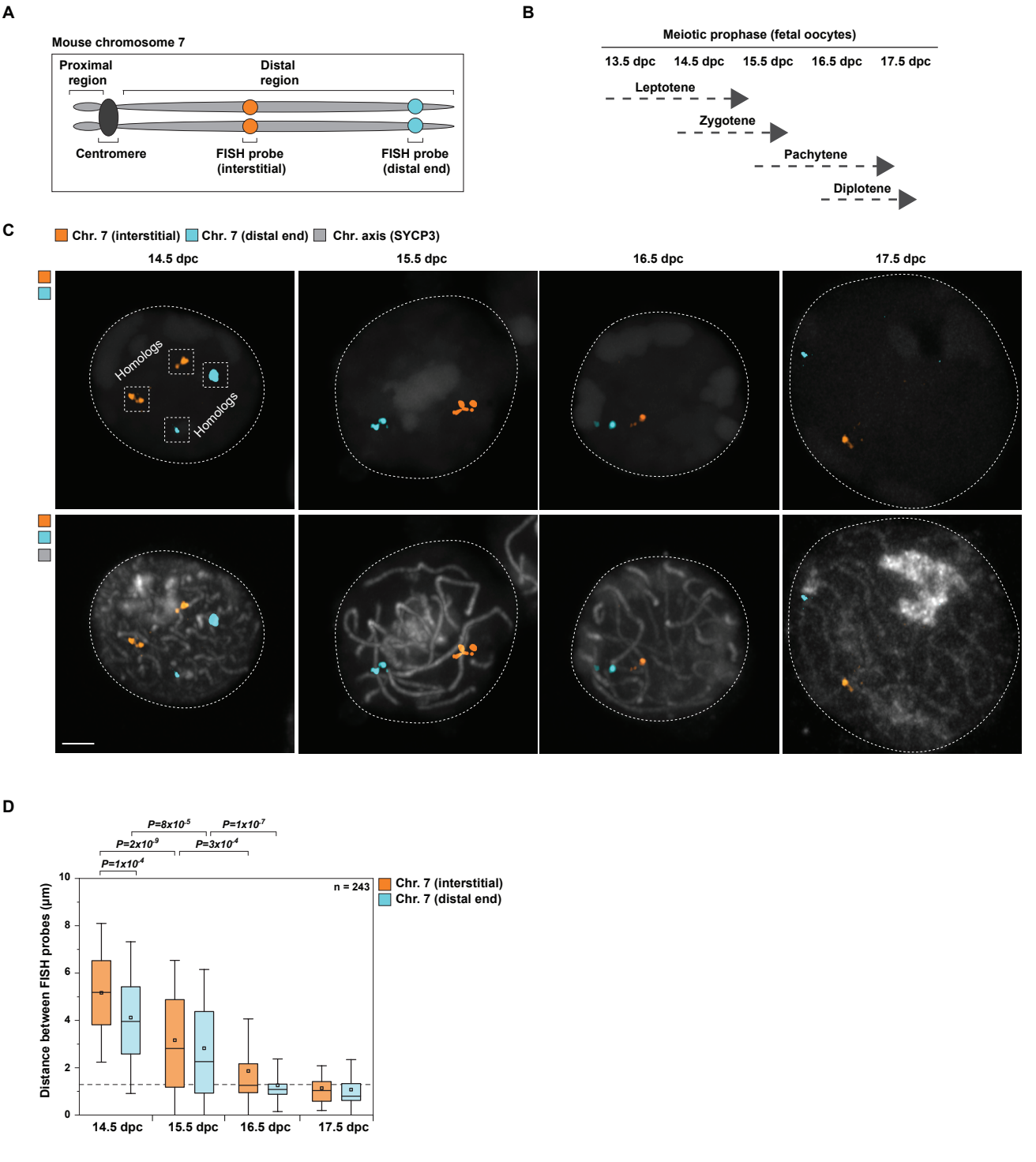
A
Mouse chromosome 7
Proximal region
Distal region
Centromere
FISH probe (interstitial)
FISH probe (distal end)
B
Meiotic prophase (fetal oocytes)
13.5 dpc
14.5 dpc
15.5 dpc
16.5 dpc
17.5 dpc
Leptotene
Zygotene
Pachytene
Diplotene
C
Chr. 7 (interstitial)
Chr. 7 (distal end)
Chr. axis (SYCP3)
14.5 dpc
15.5 dpc
16.5 dpc
17.5 dpc
Homologs
Homologs
D
P=8x10-5
P=1x10-7
P=2x10-9
P=3x10-4
P=1x10-4
n = 243
Chr. 7 (interstitial)
Chr. 7 (distal end)
Distance between FISH probes (µm)
0
2
4
6
8
10
14.5 dpc
15.5 dpc
16.5 dpc
17.5 dpc

3.3.2. Developing a method for live-cell imaging of fetal oocytes

I sought to better understand the temporal and dynamic processes involved in female meiotic prophase. To this end, I developed a simplified method where fluorescently labelled protein reporters are introduced into mouse fetal oocytes for subsequent live-cell imaging studies. This method is divided into four steps: First, chemical and mechanical disaggregation is used to generate single-cell suspensions from mouse fetal ovaries. Second, the single-cell suspensions derived from fetal ovaries are transfected with plasmid DNA encoding fluorescently labelled proteins of interest. Third, the ovarian cells transfected with plasmids are co-cultured alongside non-transfected somatic cells to promote meiotic progression of the transfected fetal oocytes. Finally, fluorescent reporters are visualized in transfected fetal oocytes through live-cell microscopy. A detailed description of the steps involved in this method are described below.

3.3.3. Fluorescent reporters are introduced into fetal oocytes through electroporation

To investigate dynamic events during female meiotic prophase, I first aimed to isolate fetal oocytes from fetal ovaries for subsequent transfection of fluorescently labelled protein reporters. I found that fetal oocytes can be isolated for transfection through chemical and mechanical disaggregation of fetal ovaries. These disaggregation processes breakdown the structure of the ovary by destroying the extracellular matrices that aggregate cells *in situ*. Next, I transfected the isolated cell population from fetal ovaries with plasmid DNA encoding fluorescently labelled proteins of interest. In particular, I utilized a CMV (Human cytomegalovirus) promoter-driven plasmid, encoding the fluorescently labelled protein reporter mClover-SYCP3. mClover is an improved variant of the eGFP (enhanced green fluorescent) protein and SYCP3 is a component of chromosome axes (described in further

detail in chapter 1). Localization of mClover-SYCP3 signals along chromosome axes indicates the successful delivery of plasmids into the ovary-derived primary cells. Indeed, I successfully detected expression of mClover-SYCP3 in fetal oocytes following transfection via electroporation (Fig. 17A), lipofection, or inactivated virus delivery methods. In brief, electroporation is a non-chemical based transfection method. Defined pulses of direct electrical current can transiently increase cell membrane permeability, enabling plasmid DNA to enter the cell (Potter and Heller, 2003). Lipofection or inactivated virus delivery are biochemical-based transfection methods. Liposomes (via lipofection) or inactivated virus envelopes (specifically the inactivated-Sendai virus) can encapsulate plasmid DNA and fuse with cell membranes, delivering plasmid DNA into cells (Felgner et al., 1987; Kaneda et al., 2002). Expression of fluorescently labelled protein reporters can be detected in fetal oocytes 24 hours post-transfection. It is important to note that the isolated ovarian cell population contains different ovarian cell types in addition to fetal oocytes. Nevertheless, transfected fetal oocytes are easily distinguished from other ovarian cell types due to the characteristic morphology of germ cells. Specifically, female and male germ cells are spherical cells, approximately 10 µm in diameter, containing a small cytoplasmic rim around a large circular nucleus (Shibuya and Watanabe, 2018). After evaluation of the three transfection procedures, I considered that electroporation is the most suitable method for plasmid delivery into fetal oocytes. Electroporation requires the shortest duration of cell manipulation and does not expose cells to toxic chemical-based transfection reagents that negatively affect cell viability. Subsequent optimization of electroporation conditions improved the efficiency of plasmid delivery into fetal oocytes while minimizing the voltage required for electroporation (table 7). Furthermore, I found that the morphology of chromosome axes in fetal oocytes expressing pCMV-mClover-SYCP3 (Fig. 17A) appeared similar to that in fetal oocytes derived from Rec8-

eGFP transgenic mice (Fig. 17C), with Rec8 being another component of chromosome axes (described in further detail in chapter 1). This indicated that transiently expressed fluorescent reporters express and localize alongside their endogenous counterparts in fetal oocytes. I additionally found that fluorescently labelled protein reporters can be successfully introduced and expressed in fetal oocytes derived from 13.5 dpc to 15.5 dpc fetal ovaries (Fig. 17).

Next, I investigated whether expression can be selectively induced for only fetal oocytes by employing a germ cell-specific promoter instead of the constitutive CMV promoter. While I found that constitutive promoters such as CMV or EF1α (promoter of human elongation factor 1α) successfully drive expression of fluorescently labelled protein reporters in fetal oocytes (Fig. 17A, 17B), I was unable to detect expression of reporters in germ cells using the germ cell-specific promoters for *Stra8*, *Vasa,* or *Meioc* (Fig. 17D-F). Together, these results indicate that electroporation is a reliable method to deliver plasmid-encoded fluorescent reporters driven by constitutive promoters into fetal oocytes during different stages of meiotic prophase.

Figure 17: Live-cell imaging of mouse fetal oocytes. Shown on next page. (A-B) Live mouse fetal oocytes expressing mClover-SYCP3 following electroporation with plasmids driven by the constitutive promoters CMV (A) or EF1α (B). Fetal oocytes derived from 15.5 dpc fetal ovaries were electroporated and imaged 24 hours later (corresponding to 16.5 dpc). Central Z positions of fetal oocytes are shown. Circles highlight oocyte nuclei. Scale bars, 5 µm. (C) Live fetal oocyte derived from a 16.5 dpc Rec8-eGFP transgenic mouse fetal ovary. Maximum intensity projection of fetal oocyte is shown. Circle highlights oocyte nucleus. Scale bar, 5 µm. (D-F) Live mouse fetal oocytes fail to express mClover-SYCP3 following electroporation with plasmids driven by the germ-cell specific promoters *Vasa* (D), *Stra8* (E), or *Meioc* (F). Fetal oocytes derived from 15.5 dpc fetal ovaries were electroporated and imaged 24 hours later (corresponding to 16.5 dpc). Scale bars, 30 µm. (G) Reconstituted ovary containing transfected fetal oocytes expressing pCMV-mClover-SYCP3. Fetal oocytes derived from 13.5 dpc fetal ovaries were electroporated and imaged 24 hours later (corresponding to 14.5 dpc). Maximum intensity projection of reconstituted ovary is shown. Circle highlights boundary of reconstituted ovary. Scale bar, 20 µm. Arrows indicate clusters of transfected cells within the reconstituted ovary. (H) Live mouse fetal oocyte expressing mClover-TRF1. Fetal oocytes derived from 13.5 dpc fetal ovaries were electroporated and imaged 24 hours later (corresponding to 14.5 dpc). Maximum intensity projection of fetal oocyte at individual time points are shown along with a time-colored projection. Scale bar, 5 µm. (I) Schematic representation of the steps involved in preparing fetal oocytes for live-cell imaging. First, fetal ovaries are dissected from mouse embryos and ovaries are disaggregated to generate a single-cell suspension of ovarian cells, including fetal oocytes. Second, the fetal ovarian cells are electroporated to deliver plasmids encoding fluorescently labelled proteins of interest into fetal oocytes. Third, transfected ovarian cells are co-cultured on a layer of pre-seeded feeder cells. Fourth, fluorescent reporters are visualized in transfected fetal oocytes through live-cell microscopy 24 hours after electroporation.

Figure 17

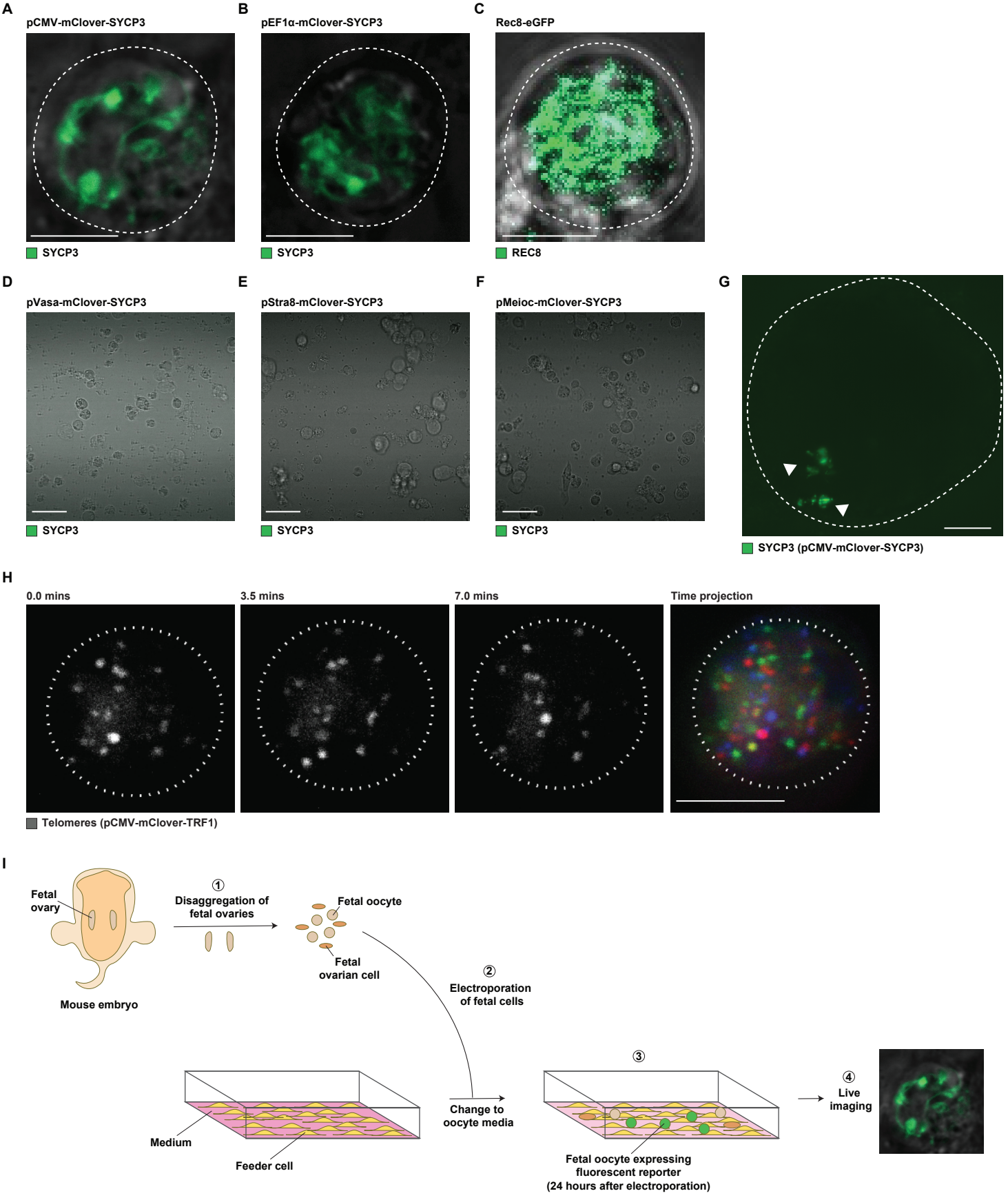
A
pCMV-mClover-SYCP3
SYCP3
B
pEF1α-mClover-SYCP3
SYCP3
C
Rec8-eGFP
REC8
D
pVasa-mClover-SYCP3
SYCP3
E
pStra8-mClover-SYCP3
SYCP3
F
pMeioc-mClover-SYCP3
SYCP3
G
SYCP3 (pCMV-mClover-SYCP3)
H
0.0 mins
3.5 mins
7.0 mins
Time projection
Telomeres (pCMV-mClover-TRF1)
I
Fetal ovary
Mouse embryo
① Disaggregation of fetal ovaries
Fetal oocyte
Fetal ovarian cell
② Electroporation of fetal cells
Change to oocyte media
Medium
Feeder cell
③
Fetal oocyte expressing fluorescent reporter (24 hours after electroporation)
④ Live imaging

Table 7: Optimization of electroporation conditions. Expression of pCMV-mClover-SYCP3 (P) following electroporation with specified conditions. Detection of expression in $\geq$ 10 fetal oocytes per well denoted as 'Yes', expression in $<$ 10 fetal oocytes per well denoted as 'Low', no expression detected in fetal oocytes denoted as 'No'. NP denotes no plasmid. The mildest voltage condition was selected for further experiments, with condition highlighted in bold.

Pulse voltage (V)	**Pulse width (ms)**	**Pulse number**	**Plasmid**	**Expression detected in $\geq$ 10 fetal oocytes per well**
0	1	1	P	No
1400	20	1	P	Yes
1500	20	1	P	Low
1600	20	1	P	Low
1700	20	1	P	Low
1100	30	1	P	Yes
1200	30	1	P	Yes
1300	30	1	P	Yes
1400	30	1	P	Yes
1000	40	1	P	Yes
1100	40	1	P	Yes
1200	40	1	P	Yes
1100	20	2	P	Yes
1200	20	2	P	Yes
1300	20	2	P	Yes
1400	20	2	P	Yes
850	30	2	P	Low
950	**30**	**2**	P	Yes
1050	30	2	P	Yes
1150	30	2	P	Yes
1300	10	3	P	Yes
1400	10	3	P	Yes
1500	10	3	P	Low
1600	10	3	P	Low
1200	30	1	NP	No

3.3.4. Transfected fetal oocytes can be cultured on a feeder layer during live-cell imaging

Fetal oocytes exhibit poor viability when cultured *ex vivo* in isolation. Previous reports demonstrate survival of fetal oocytes and progression through meiosis when co-cultured with somatic gonadal cells (Hikabe et al., 2016; Morohaku et al., 2016). In particular, fetal oocytes can be aggregated with somatic gonadal cells to generate reconstituted ovaries. This culture method is thought to recapitulate the *in vivo* ovarian environment and promote fetal oocyte maturation (Hayashi and Saitou, 2013; Hikabe et al., 2016). I surmised that generating reconstituted ovaries with transfected fetal oocytes would support *ex vivo* maturation of the fetal oocytes. However, poor subcellular resolution is obtained when imaging reconstituted ovaries due to the several layers of cells surrounding fetal oocytes (Fig. 17G). These issues are resolved when transfected fetal oocytes are cultured in a 2D-setup above a pre-seeded feeder layer of mouse embryonic fibroblasts (Fig. 17H, 17I). Using this culture method, I was able to visualize dynamic events during female meiotic prophase including rapid telomere movements using a fluorescent reporter for telomeres, mClover-TRF1 (Fig. 17H). Together these results demonstrate that fluorescent reporters can be tracked in fetal oocytes through live-cell imaging following transfection and 2D culture of fetal oocytes (Fig. 17I).

3.4.0. Discussion

3.4.1. Uncovering further detail about homologous chromosome pairing in female meiosis

Mice have in total 20 chromosomes, each with a maternal and paternal homolog per diploid cell. An outstanding question in mammalian meiosis is understanding how each of the 20 homologous pairs of chromosomes are able to pair together prior to synapsis while avoiding mismatches. The presence of pairing centers within mammalian chromosomes could explain how homolog recognition and chromosome pairing is achieved during meiotic prophase. Whether mammalian chromosomes contain pairing centers similar to non-mammalian organisms remains an open question. To explore this concept, I aimed to narrow down on the specific chromosomal locations where pairing is initiated between maternal and paternal chromosomes. Here, I found that pairing between maternal and paternal chromosome 7 is initiated closer to the distal end than the distal interstitial region of chromosome 7. Indeed, pairing of the distal ends of maternal and paternal chromosome 7 is initiated earlier in pachytene than at the distal interstitial regions of chromosome 7 (Fig. 16D). The timing of chromosome pairing corroborates with previous reports, which also show chromosome pairing is complete by pachytene in female meiosis in mammals (O'Keeffe et al., 1997; Pfeifer et al., 2003; Speed, 1982; Tankimanova et al., 2004). Further FISH experiments must be conducted to narrow down the location where chromosome pairing starts on chromosome 7 during female meiosis. Comparative FISH experiments should be conducted to determine the region of pairing initiation along other mammalian chromosomes. From here, genomic analyses are needed to identify whether these chromosomal regions contain predicted pairing DNA sequence motifs. In *C.elegans*, pairing centers on different chromosomes are comprised of unique repetitive DNA sequences (Phillips et al., 2009). Once the pairing

initiation regions are identified along mammalian chromosomes, methods such as reverse-ChIP (chromatin immunoprecipitation) (reviewed by Rusk, 2009) could be employed to determine whether a specific set of proteins localize to these chromosomal regions during meiosis. If so, I hope to investigate further whether these proteins are required to execute homolog recognition using genetic mutation methods. Together these experiments will provide a better understanding of how homolog recognition functions in mammalian meiosis.

3.4.2. Developing a live-cell imaging method for mouse fetal oocytes

The majority of our knowledge regarding mammalian meiosis is derived from fixed cell experiments. While these studies have expanded our understanding about different events during meiotic prophase, analysis of living germ cells may provide further insight into how dynamic processes such as chromosome pairing function. A live-imaging technique for mouse spermatocytes was previously developed in the laboratory of Y. Watanabe and has since been employed in several investigations of meiotic prophase (Shibuya and Watanabe, 2018; Shibuya et al., 2014b, 2015; Zhang et al., 2019). As processes during meiotic prophase can differ between the different sexes, it would be useful to also investigate female meiotic prophase through live-cell imaging. Currently, live-cell imaging of fetal oocytes has not been utilized as frequently as live-cell imaging of spermatocytes. Therefore, during my PhD, I developed a simplified method for live-cell imaging of mouse fetal oocytes. The developed method involves four key steps (Fig. 17I), which can be adapted to accommodate different transfection methods. Sub-cellular events during female meiotic prophase can be visualized with ease using confocal microscopy by culturing transfected fetal oocytes on top of a pre-seeded layer of somatic feeder cells. In addition, this culture method also supports oocyte survival in an *ex vivo* context. I anticipate this is due to the high-cell density of the feeder

layer, which provides fetal oocytes with the necessary cell-to-cell interactions required for survival *ex vivo*. This agrees with other studies that found that culturing PGCs or fetal oocytes in high-cell density can promote cell survival and maturation during cell culture (Farini et al., 2005; Hikabe et al., 2016). It would be interesting to use the method presented here to transfect fetal oocytes with fluorescently labelled chromosome-specific reporters, such as Transcription Activator Like (TAL) proteins or utilizing the CRISPR/dCAS9 systems (Ma et al., 2017b; Miyanari et al., 2013; Zhou et al., 2017). These tools would enable a specific pair of maternal and paternal chromosomes to be visualized and tracked as homologous chromosome pairing proceeds in live cells.

3.4.3. Summary

In this section of my dissertation, I have generated two methods to better understand how homologous chromosome pairing proceeds during mammalian female meiosis. I established a method to identify the homologous chromosome pairing center on mouse chromosome 7 using region-specific FISH probes. In addition, I developed a method for the isolation, transfection, and culturing of mouse fetal oocytes that is suitable for live-cell imaging studies. I plan to utilize these methods to further explore female meiotic prophase including homologous chromosome pairing.

List of References

Acquaviva, L., Boekhout, M., Karasu, M., Brick, K., Pratto, F., van Overbeek, M., Kauppi, L., Camerini-Otero, R.D., Jasin, M., and Keeney, S. (2020). Ensuring meiotic DNA break formation in the mouse pseudoautosomal region. Nature. *582*, 426–431.

Adler, I.D. (1996). Comparison of the duration of spermatogenesis between male rodents and humans. Mutat. Res. - Fundam. Mol. Mech. Mutagen. *352*, 169–172.

Agostinho, A., Meier, B., Sonneville, R., Jagut, M., Woglar, A., Blow, J., Jantsch, V., and Gartner, A. (2013). Combinatorial Regulation of Meiotic Holliday Junction Resolution in C. elegans by HIM-6 (BLM) Helicase, SLX-4, and the SLX-1, MUS-81 and XPF-1 Nucleases. PLoS Genet. *9*, e1003591.

Ahmed, E.A., van der Vaart, A., Barten, A., Kal, H.B., Chen, J., Lou, Z., Minter-Dykhouse, K., Bartkova, J., Bartek, J., de Boer, P., et al. (2007). Differences in DNA double strand breaks repair in male germ cell types: Lessons learned from a differential expression of Mdc1 and 53BP1. DNA Repair (Amst). *6*, 1243–1254.

Ahmed, E.A., Philippens, M.E.P., Kal, H.B., de Rooij, D.G., and de Boer, P. (2010). Genetic probing of homologous recombination and non-homologous end joining during meiotic prophase in irradiated mouse spermatocytes. Mutat. Res. - Fundam. Mol. Mech. Mutagen. *688*, 12–18.

Ahnesorg, P., Smith, P., and Jackson, S.P. (2006). XLF interacts with the XRCC4-DNA Ligase IV complex to promote DNA nonhomologous end-joining. Cell. *124*, 301–313.

Alani, E., Thresher, R., Griffith, J.D., and Kolodner, R.D. (1992). Characterization of DNA-binding and strand-exchange stimulation properties of y-RPA, a yeast single-strand-DNA-binding protein. J. Mol. Biol. *227*, 54–71.

Allers, T., and Lichten, M. (2001). Differential timing and control of noncrossover and crossover recombination during meiosis. Cell. *106*, 47–57.

Anderson, E.L., Baltus, A.E., Roepers-Gajadien, H.L., Hassold, T.J., De Rooij, D.G., Van Pelt, A.M.M., and Page, D.C. (2008). Stra8 and its inducer, retinoic acid, regulate meiotic initiation in both spermatogenesis and oogenesis in mice. Proc. Natl. Acad. Sci. U. S. A. *105*, 14876–14980.

Anderson, L.K., Royer, S.M.., Page, S.L., McKim, K.S., Lai, A., Lilly, M.A., and Hawley, R.S. (2005). Juxtaposition of C(2)M and the transverse filament protein C(3)G within the central region of Drosophila synaptonemal complex. Proc. Natl. Acad. Sci. U. S. A. *102*, 4482–4487.

Andrin, C., McDonald, D., Attwood, K.M., Rodrigue, A., Ghosh, S., Mirzayans, R., Masson, J.Y., Dellaire, G., and Hendzel, M.J. (2012). A requirement for polymerized actin in DNA double-strand break repair. Nucleus (United States). *3*, 384–395.

Arden, S.D., Puri, C., Au, J.S.Y., Kendrick-Jones, J., and Buss, F. (2007). Myosin VI is required for targeted membrane transport during cytokinesis. Mol. Biol. Cell. *18*, 4750–4761.

Audebert, M., Salles, B., and Calsou, P. (2004). Involvement of poly(ADP-ribose) polymerase-1 and XRCC1/DNA ligase III in an alternative route for DNA double-strand breaks rejoining. J. Biol. Chem. *279*, 55117–55126.

Aymard, F., Aguirrebengoa, M., Guillou, E., Javierre, B.M., Bugler, B., Arnould, C., Rocher, V., Iacovoni, J.S., Biernacka, A., Skrzypczak, M., et al. (2017). Genome-wide mapping of long-range contacts unveils clustering of DNA double-strand breaks at damaged active genes. Nat. Struct. Mol. Biol. *24*, 353–361.

Baarlink, C., Wang, H., and Grosse, R. (2013). Nuclear actin network assembly by formins regulates the SRF coactivator MAL. Science. *340*, 864–867.

Bailis, J.M., and Roeder, G.S. (2000). Pachytene exit controlled by reversal of Mek1-dependent phosphorylation. Cell. *101*, 211–221.

Bamburg, J.R., and Bernstein, B.W. (2010). Roles of ADF/cofilin in actin polymerization and beyond. F1000 Biol. Rep. *2*, 1–7.

Bao, J., Jana, S.S., and Adelstein, R.S. (2005). Vertebrate nonmuscle myosin II isoforms rescue small interfering RNA-induced defects in COS-7 cell cytokinesis. J. Biol. Chem. *280*, 19594–19599.

Barchi, M., Mahadevaiah, S., Di Giacomo, M., Baudat, F., de Rooij, D.G., Burgoyne, P.S., Jasin, M., and Keeney, S. (2005). Surveillance of Different Recombination Defects in Mouse Spermatocytes Yields Distinct Responses despite Elimination at an Identical Developmental Stage. Mol. Cell. Biol. *25*, 7203–7215.

Bastin-Shanower, S.A., and Brill, S.J. (2001). Functional analysis of the four DNA binding domains of replication protein A. The role of RPA2 in ssDNA binding. J. Biol. Chem. *276*, 36446–36453.

Baudat, F., and De Massy, B. (2007). Regulating double-stranded DNA break repair towards crossover or non-crossover during mammalian meiosis. Chromosom. Res. 565–577.

Baudat, F., Buard, J., Grey, C., Fledel-Alon, A., Ober, C., Przeworski, M., Coop, G., and De Massy, B. (2010). PRDM9 is a major determinant of meiotic recombination hotspots in humans and mice. Science. *327*, 836–840.

Baudat, F., Imai, Y., and De Massy, B. (2013). Meiotic recombination in mammals: Localization and regulation. Nat. Rev. Genet. 794–806.

Belin, B.J., Cimini, B.A., Blackburn, E.H., and Mullins, R.D. (2013). Visualization of actin filaments and monomers in somatic cell nuclei. Mol. Biol. Cell. *24*, 982–994.

Belin, B.J., Lee, T., and Mullins, R.D. (2015). DNA damage induces nuclear actin filament assembly by formin-2 and spire-1/2 that promotes efficient DNA repair. Elife. *4*, e07735.

Bellani, M.A., Romanienko, P.J., Cairatti, D.A., and Camerini-Otero, R.D. (2005). SPO11 is required for sex-body formation, and Spo11 heterozygosity rescues the prophase arrest of Atm-/- spermatocytes. J. Cell Sci. *118*, 3233–3245.

Bellani, M.A., Boateng, K.A., McLeod, D., and Camerini-Otero, R.D. (2010). The Expression Profile of the Major Mouse SPO11 Isoforms Indicates that SPO11β Introduces Double Strand Breaks and Suggests that SPO11α Has an Additional Role in Prophase in both Spermatocytes and Oocytes. Mol. Cell. Biol. *30*, 4391–4403.

Bellutti, L., Abby, E., Tourpin, S., Messiaen, S., Moison, D., Trautmann, E., Guerquin, M.J., Rouiller-Fabre, V., Habert, R., and Livera, G. (2019). Divergent roles of cyp26b1 and endogenous retinoic acid in mouse fetal gonads. Biomolecules. *9*, 536.

Bellve, A.R., Cavicchia, J.C., Millette, C.F., O'Brien, D.A., Bhatnagar, Y.M., and Dym, M. (1977). Spermatogenic cells of the prepuberal mouse. Isolation and morphological characterization. J. Cell Biol. *74*, 68–85.

Berchowitz, L.E., Francis, K.E., Bey, A.L., and Copenhaver, G.P. (2007). The role of AtMUS81 in interference-insensitive crossovers in A. thaliana. PLoS Genet. *3*, e132.

Berg, J.S., and Cheney, R.E. (2002). Myosin-X is an unconventional myosin that undergoes intrafilopodial motility. Nat. Cell Biol. *4*, 246–250.

Bergerat, A., De Massy, B., Gadelle, D., Varoutas, P.C., Nicolas, A., and Forterre, P. (1997). An atypical topoisomerase II from archaea with implications for meiotic recombination. Nature *386*, 414–417.

Bird, A.W., Yu, D.Y., Pray-Grant, M.G., Qiu, Q., Harmon, K.E., Megee, P.C., Grant, P.A., Smith, M.M., and Christman, M.F. (2002). Acetylation of histone H4 by Esa1 is required for DNA double-strand break repair. Nature. *419*, 411–415.

Bishop, D.K. (1994). RecA homologs Dmc1 and Rad51 interact to form multiple nuclear complexes prior to meiotic chromosome synapsis. Cell. *79*, 1081–1092.

Bishop, D.K., Park, D., Xu, L., and Kleckner, N. (1992). DMC1: A meiosis-specific yeast homolog of E. coli recA required for recombination, synaptonemal complex formation, and cell cycle progression. Cell. *69*, 439–456.

Bisig, C.G., Guiraldelli, M.F., Kouznetsova, A., Scherthan, H., Höög, C., Dawson, D.S., and Pezza, R.J. (2012). Synaptonemal complex components persist at centromeres and are required for homologous centromere pairing in mouse spermatocytes. PLoS Genet. *8*, e1002701.

Black, S.J., Kashkina, E., Kent, T., and Pomerantz, R.T. (2016). DNA polymerase θ: A unique multifunctional end-joining machine. Genes (Basel). 67.

Blackwell, L.J., and Borowiec, J.A. (1994). Human replication protein A binds single-stranded DNA in two distinct complexes. Mol. Cell. Biol. *14*, 3993–4001.

Blat, Y., Protacio, R.U., Hunter, N., and Kleckner, N. (2002). Physical and functional interactions among basic chromosome organizational features govern early steps of meiotic chiasma formation. Cell. 791–802.

Boateng, K.A., Bellani, M.A., Gregoretti, I. V., Pratto, F., and Camerini-Otero, R.D. (2013). Homologous Pairing Preceding SPO11-Mediated Double-Strand Breaks in Mice. Dev. Cell. *24*, 196–205.

Bochkareva, E., Korolev, S., Lees-Miller, S.P., and Bochkarev, A. (2002). Structure of the RPA trimerization core and its role in the multistep DNA-binding mechanism of RPA. EMBO J. *21*, 1855–1863.

Bocker, T., Barusevicius, A., Snowden, T., Rasio, D., Guerrette, S., Robbins, D., Schmidt, C., Burczak, J., Croce, C.M., Copeland, T., et al. (1999). hMSH5: A human MutS homologue that forms a novel heterodimer with hMSH4 and is expressed during spermatogenesis. Cancer Res. *59*, 816–822.

Boddy, M.N., Gaillard, P.H.L., McDonald, W.H., Shanahan, P., Yates, J.R., and Russell, P. (2001). Mus81-Eme1 are essential components of a Holliday junction resolvase. Cell. *107*, 537–548.

de Boer, E., Lhuissier, F.G.P., and Heyting, C. (2009). Cytological analysis of interference in mouse meiosis. Methods Mol. Biol. 355–382.

Bohnsack, M., Stüven, T., Kuhn, C., Cordes, V., and Görlich, D. (2006). A selective block of nuclear actin export stabilizes the giant nuclei of Xenopus oocytes. Nat. Cell Biol. *8*, 257–263.

Bolcun-Filas, E., Rinaldi, V.D., White, M.E., and Schimenti, J.C. (2014). Reversal of female infertility by Chk2 ablation reveals the oocyte DNA damage checkpoint pathway. Science. *343*, 533–536.

Bolland, D.J., King, M.R., Reik, W., Corcoran, A.E., and Krueger, C. (2013). Robust 3D DNA FISH using directly labeled probes. J. Vis. Exp. *78*, 50587.

Borum, K. (1961). Oogenesis in the mouse. A study of the meiotic prophase. Exp. Cell Res. *24*, 495–507.

Bowles, J., Knight, D., Smith, C., Wilhelm, D., Richman, J., Mamiya, S., Yashiro, K., Chawengsaksophak, K., Wilson, M.J., Rossant, J., et al. (2006). Retinoid signaling determines germ cell fate in mice. Science. *312*, 596–600.

Brick, K., Smagulova, F., Khil, P., Camerini-Otero, R.D., and Petukhova, G.V. (2012). Genetic recombination is directed away from functional genomic elements in mice. Nature. *485*, 642–645.

Brick, K., Thibault-Sennett, S., Smagulova, F., Lam, K.W.G., Pu, Y., Pratto, F., Camerini-Otero, R.D., and Petukhova, G.V. (2018). Extensive sex differences at the initiation of genetic recombination. Nature. *561*, 338–342.

Broman, K., and Weber, J.L. (2000). Characterization of human crossover interference. Am. J. Hum. Genet. *66*, 1911–1926.

Broman, K.W., Murray, J.C., Sheffield, V.C., White, R.L., and Weber, J.L. (1998). Comprehensive human genetic maps: Individual and sex-specific variation in recombination. Am. J. Hum. Genet. *63*, 861–869.

Broman, K.W., Rowe, L.B., Churchill, G.A., and Paigen, K. (2002). Crossover interference in the mouse. Genetics. *160*, 1123–1131.

Brosey, C.A., Chagot, M.E., Ehrhardt, M., Pretto, D.I., Weiner, B.E., and Chazin, W.J. (2009). NMR analysis of the architecture and functional remodeling of a modular multidomain protein, RPA. J. Am. Chem. Soc. *131*, 6346–6347.

Bubb, M.R., Govindasamy, L., Yarmola, E.G., Vorobiev, S.M., Almo, S.C., Somasundaram, T., Chapman, M.S., Agbandje-McKenna, M., and McKenna, R. (2002). Polylysine induces an antiparallel actin dimer that nucleates filament assembly: Crystal structure at 3.5-Å resolution. J. Biol. Chem. *277*, 20999–21006.

Burgess, S.A., Yu, S., Walker, M.L., Hawkins, R.J., Chalovich, J.M., and Knight, P.J. (2007). Structures of Smooth Muscle Myosin and Heavy Meromyosin in the Folded, Shutdown State. J. Mol. Biol. *372*, 1165–1178.

Buss, F., Kendrick-Jones, J., Lionne, C., Knight, A.E., Côté, G.P., and Luzio, J.P. (1998). The localization of myosin VI at the Golgi complex and leading edge of fibroblasts and its phosphorylation and recruitment into membrane ruffles of A431 cells after growth factor stimulation. J. Cell Biol. *143*, 1535–1545.

Cahoon, C.K., and Hawley, R.S. (2016). Regulating the construction and demolition of the synaptonemal complex. Nat. Struct. Mol. Biol. 369–377.

Cannavo, E., Sanchez, A., Anand, R., Ranjha, L., Hugener, J., Adam, C., Acharya, A., Weyland, N., Aran-Guiu, X., Charbonnier, J.B., et al. (2020). Regulation of the MLH1–MLH3 endonuclease in meiosis. Nature. Preprint.

Cao, L., Alani, E., and Kleckner, N. (1990). A pathway for generation and processing of double-strand breaks during meiotic recombination in S. cerevisiae. Cell. *61*, 1089–1101.

Caridi, C.P., D'agostino, C., Ryu, T., Zapotoczny, G., Delabaere, L., Li, X., Khodaverdian, V.Y., Amaral, N., Lin, E., Rau, A.R., et al. (2018). Nuclear F-actin and myosins drive relocalization of heterochromatic breaks. Nature. *559*, 54–60.

Ceccaldi, R., Liu, J.C., Amunugama, R., Hajdu, I., Primack, B., Petalcorin, M.I.R., O'Connor, K.W., Konstantinopoulos, P.A., Elledge, S.J., Boulton, S.J., et al. (2015). Homologous-recombination-deficient tumours are dependent on Polθ-mediated repair. Nature. *518*, 258–262.

Chaigne, A., Campillo, C., Voituriez, R., Gov, N.S., Sykes, C., Verlhac, M.H., and Terret, M.E. (2016). F-actin mechanics control spindle centring in the mouse zygote. Nat. Commun. *7*, 10253.

Chang, H.H.Y., Pannunzio, N.R., Adachi, N., and Lieber, M.R. (2017). Non-homologous DNA end joining and alternative pathways to double-strand break repair. Nat. Rev. Mol. Cell Biol. 495–506.

Chapman, J.R., and Jackson, S.P. (2008). Phospho-dependent interactions between NBS1 and MDC1 mediate chromatin retention of the MRN complex at sites of DNA damage. EMBO Rep. *9*, 795–801.

Chen, H., Lisby, M., and Symington, L.S. (2013). RPA Coordinates DNA End Resection and Prevents Formation of DNA Hairpins. Mol. Cell. *50*.

Chen, Z., Yang, H., and Pavletich, N.P. (2008). Mechanism of homologous recombination from the RecA-ssDNA/dsDNA structures. Nature. *453*, 489–494.

Chiolo, I., Tang, J., Georgescu, W., and Costes, S. V. (2013). Nuclear dynamics of radiation-induced foci in euchromatin and heterochromatin. Mutat. Res. - Fundam. Mol. Mech. Mutagen. 56–66.

Ciccia, A., McDonald, N., and West, S.C. (2008). Structural and functional relationships of the XPF/MUS81 family of proteins. Annu. Rev. Biochem. 259–287.

Claeys Bouuaert, C., and Keeney, S. (2017). Distinct DNA-binding surfaces in the ATPase and linker domains of MutLγ determine its substrate specificities and exert separable functions in meiotic recombination and mismatch repair. PLoS Genet. *13*, e1006722.

Clapier, C.R., and Cairns, B.R. (2009). The biology of chromatin remodeling complexes. Annu. Rev. Biochem. 273–304.

Clark, T.G., and Merriam, R.W. (1977). Diffusible and bound actin in nuclei of xenopus laevis oocytes. Cell. *12*, 883–891.

Clattenburg, R.E., Singh, R.P., and Montemurro, D.G. (1972). Intranuclear filamentous inclusions in neurons of the rabit hypothalamus. J. Ultrasructure Res. *39*, 549–555.

Clift, D., and Schuh, M. (2013). Restarting life: Fertilization and the transition from meiosis to mitosis. Nat. Rev. Mol. Cell Biol. 549–562.

Cloutier, J.M., and Turner, J.M.A. (2010). Meiotic sex chromosome inactivation. Curr. Biol. R962.

Cohen, P.E., Pollack, S.E., and Pollard, J.W. (2006). Genetic analysis of chromosome pairing, recombination, and cell cycle control during first meiotic prophase in mammals. Endocr. Rev. 398–426.

Cole, F., Kauppi, L., Lange, J., Roig, I., Wang, R., Keeney, S., and Jasin, M. (2012). Homeostatic control of recombination is implemented progressively in mouse meiosis. Nat. Cell Biol. *14*, 424–430.

Coop, G., and Przeworski, M. (2007). An evolutionary view of human recombination. Nat. Rev. Genet. 23–34.

Cooper, J.A., Buhle, E.L., Walker, S.B., Tsong, T.Y., and Pollard, T.D. (1983). Kinetic Evidence for a Monomer Activation Step in Actin Polymerization. Biochemistry. *22*, 2193–2202.

Critchlow, S.E., Bowater, R.P., and Jackson, S.P. (1997). Mammalian DNA double-strand break repair protein XRCC4 interacts with DNA ligase IV. Curr. Biol. *7*, 588–598.

Dai, J., Voloshin, O., Potapova, S., and Camerini-Otero, R.D. (2017). Meiotic Knockdown and Complementation Reveals Essential Role of RAD51 in Mouse Spermatogenesis. Cell Rep. *18*, 1383–1394.

Daniel, K., Lange, J., Hached, K., Fu, J., Anastassiadis, K., Roig, I., Cooke, H.J., Stewart, A.F., Wassmann, K., Jasin, M., et al. (2011). Meiotic homologue alignment and its quality surveillance are controlled by mouse HORMAD1. Nat. Cell Biol. *13*, 599–610.

Dayel, M.J., and Mullins, R.D. (2004). Activation of Arp2/3 complex: Addition of the first subunit of the new filament by a WASP protein triggers rapid ATP hydrolysis on Arp2. PLoS Biol. *2*, E91.

Deng, X., Habel, J.E., Kabaleeswaran, V., Snell, E.H., Wold, M.S., and Borgstahl, G.E.O. (2007). Structure of the Full-length Human RPA14/32 Complex Gives Insights into the Mechanism of DNA Binding and Complex Formation. J. Mol. Biol. *374*, 865–876.

Diaz, R.L., Alcid, A.D., Berger, J.M., and Keeney, S. (2002). Identification of Residues in Yeast Spo11p Critical for Meiotic DNA Double-Strand Break Formation. Mol. Cell. Biol. *22*, 1106–1115.

Dietrich, A.J.J., and Mulder, R.J.P. (1983). A light- and electron microscopic analysis of meiotic prophase in female mice. Chromosoma. *88*, 377–385.

Ding, D.Q., Okamasa, K., Yamane, M., Tsutsumi, C., Haraguchi, T., Yamamoto, M., and Hiraoka, Y. (2012). Meiosis-specific noncoding RNA mediates robust pairing of homologous chromosomes in meiosis. Science. *336*, 732–736.

Ding, D.Q., Okamasa, K., Katou, Y., Oya, E., Nakayama, J.I., Chikashige, Y., Shirahige, K., Haraguchi, T., and Hiraoka, Y. (2019). Chromosome-associated RNA–protein complexes promote pairing of homologous chromosomes during meiosis in Schizosaccharomyces pombe. Nat. Commun. *10*, 5598.

Ding, X., Xu, R., Yu, J., Xu, T., Zhuang, Y., and Han, M. (2007). SUN1 Is Required for Telomere Attachment to Nuclear Envelope and Gametogenesis in Mice. Dev. Cell. *12*, 863–872.

Dokshin, G.A., Baltus, A, E., Eppig, J.J., and Page, D.C. (2013). Oocyte differentiation is genetically dissociable from meiosis in mice. Nat. Genet. *45*, 877–883.

Dominguez, R., Freyzon, Y., Trybus, K.M., and Cohen, C. (1998). Crystal structure of a vertebrate smooth muscle myosin motor domain and its complex with the essential light chain: Visualization of the pre-power stroke state. Cell. *94*, 559–571.

Dopie, J., Skarp, K.P., Rajakylä, E.K., Tanhuanpää, K., and Vartiainen, M.K. (2012). Active maintenance of nuclear actin by importin 9 supports transcription. Proc. Natl. Acad. Sci. U. S. A. *109*, e544–e552.

Downs, J.A., Allard, S., Jobin-Robitaille, O., Javaheri, A., Auger, A., Bouchard, N., Kron, S.J., Jackson, S.P., and Côté, J. (2004). Binding of chromatin-modifying activities to phosphorylated histone H2A at DNA damage sites. Mol. Cell. *16*, 979–990.

Eaker, S., Pyle, A., Cobb, J., and Handel, M.A. (2001). Evidence for meiotic spindle checkpoint from analysis of spermatocytes from Robertsonian-chromosome heterozygous mice. J. Cell Sci. *114*, 2953–2965.

Eaker, S., Cobb, J., Pyle, A., and Handel, M.A. (2002). Meiotic prophase abnormalities and metaphase cell death in MLH1-deficient mouse spermatocytes: Insights into regulation of spermatogenic progress. Dev. Biol. *249*, 85–95.

Egile, C., Rouiller, I., Xu, X.P., Volkmann, N., Li, R., and Hanein, D. (2005). Mechanism of filament nucleation and branch stability revealed by the structure of the Arp2/3 complex at actin branch junctions. PLoS Biol. *3*, e383.

Enguita-Marruedo, A., Van Cappellen, W.A., Hoogerbrugge, J.W., Carofiglio, F., Wassenaar, E., Slotman, J.A., Houtsmuller, A., and Baarends, W.M. (2018). Live cell analyses of synaptonemal complex dynamics and chromosome movements in cultured mouse testis tubules and embryonic ovaries. Chromosoma. *127*, 341–359.

Enguita-Marruedo, A., Martín-Ruiz, M., García, E., Gil-Fernández, A., Parra, M.T., Viera, A., Rufas, J.S., and Page, J. (2019). Transition from a meiotic to a somatic-like DNA damage response during the pachytene stage in mouse meiosis. PLoS Genet. *15*, e1007439.

Fan, J., and Pavletich, N.P. (2012). Structure and conformational change of a replication protein A heterotrimer bound to ssDNA. Genes Dev. *26*, 2337–2347.

Farini, D., Scaldaferri, M.L., Iona, S., La Sala, G., and De Felici, M. (2005). Growth factors sustain primordial germ cell survival, proliferation and entering into meiosis in the absence of somatic cells. Dev. Biol. *285*, 49–56.

Felgner, P.L., Gadek, T.R., Holm, M., Roman, R., Chan, H.W., Wenz, M., Northrop, J.P., Ringold, G.M., and Danielsen, M. (1987). Lipofection: a highly efficient, lipid-mediated DNA-transfection procedure. Proc. Natl. Acad. Sci. U. S. A. *84*, 7413–7417.

Fernandez-Capetillo, O., Mahadevaiah, S.K., Celeste, A., Romanienko, P.J., Camerini-Otero, R.D., Bonner, W.M., Manova, K., Burgoyne, P., and Nussenzweig, A. (2003). H2AX is required for chromatin remodeling and inactivation of sex chromosomes in male mouse meiosis. Dev. Cell. *4*, 497–508.

Foerster, F., Braig, S., Moser, C., Kubisch, R., Busse, J., Wagner, E., Schmoeckel, E., Mayr, D., Schmitt, S., Huettel, S., et al. (2014). Targeting the actin cytoskeleton: Selective antitumor action via trapping PKCε. Cell Death Dis. *5*, e1398.

Fowler, W.E., and Aebi, U. (1982). Polymorphism of actin paracrystals induced by polylysine. J. Cell Biol. *93*, 452–458.

Fukui, Y. (1978). Intranuclear actin bundles induced by dimethyl sulfoxide in interphase nucleus of Dictyostelium. J. Cell Biol. *76*, 146–157.

Gaines, W.A., Godin, S.K., Kabbinavar, F.F., Rao, T., VanDemark, A.P., Sung, P., and Bernstein, K.A. (2015). Promotion of presynaptic filament assembly by the ensemble of S. cerevisiae Rad51 paralogues with Rad52. Nat. Commun. *6*, 7834.

Galarneau, L., Nourani, A., Boudreault, A.A., Zhang, Y., Héliot, L., Allard, S., Savard, J., Lane, W.S., Stillman, D.J., and Côté, J. (2000). Multiple links between the NuA4 histone acetyltransferase complex and epigenetic control of transcription. Mol. Cell. *5*, 927–937.

Gao, J., and Colaiácovo, M.P. (2018). Zipping and Unzipping: Protein Modifications Regulating Synaptonemal Complex Dynamics. Trends Genet. 232–245.

Gao, L., Kim, Y., Kim, B., Lofgren, S.M., Schultz-Norton, J.R., Nardulli, A.M., Heckert, L.L., and Jorgensen, J.S. (2011). Two regions within the proximal steroidogenic factor 1 promoter drive somatic cell-specific activity in developing gonads of the female mouse. Biol. Reprod. *84*, 422–434.

Garcia-Castro, M.I., Anderson, R., Heasman, J., and Wylie, C. (1997). Interactions between germ cells and extracellular matrix glycoproteins during migration and gonad assembly in the mouse embryo. J. Cell Biol. *138*, 471–480.

Garcia, V., Phelps, S.E.L., Gray, S., and Neale, M.J. (2011). Bidirectional resection of DNA double-strand breaks by Mre11 and Exo1. Nature. *479*, 241–244.

Gedge, L.J.E., Morrison, E.E., Blair, G.E., and Walker, J.H. (2005). Nuclear actin is partially associated with Cajal bodies in human cells in culture and relocates to the nuclear periphery after infection of cells by adenovirus 5. Exp. Cell Res. *303*, 229–239.

Di Giacomo, M., Barchi, M., Baudat, F., Edelmann, W., Keeney, S., and Jasin, M. (2005). Distinct DNA-damage-dependent and -independent responses drive the loss of oocytes in recombination-defective mouse mutants. Proc. Natl. Acad. Sci. U. S. A. *102*, 737–742.

Gibb, B., Ye, L.F., Kwon, Y., Niu, H., Sung, P., and Greene, E.C. (2014). Protein dynamics during presynaptic-complex assembly on individual single-stranded DNA molecules. Nat. Struct. Mol. Biol. *21*, 893–900.

Ginsburg, M., Snow, M.H.L., and McLaren, A. (1990). Primordial germ cells in the mouse embryo during gastrulation. Development. *110*, 5231–5238.

Goedecke, W., Eijpe, M., Offenberg, H.H., Van Aalderen, M., and Heyting, C. (1999). Mre11 and Ku70 interact in somatic cells, but are differentially expressed in early meiosis. Nat. Genet. *23*, 194–198.

Goley, E.D., Rodenbusch, S.E., Martin, A.C., and Welch, M.D. (2004). Critical conformational changes in the Arp2/3 complex are induced by nucleotide and nucleation promoting factor. Mol. Cell. *16*, 269–279.

Gómez, R., Jordan, P.W., Viera, A., Alsheimer, M., Fukuda, T., Jessberger, R., Llano, E., Pendás, A.M., Handel, M.A., and Suja, J.A. (2013). Dynamic localization of SMC5/6 complex proteins during mammalian meiosis and mitosis suggests functions in distinct chromosome processes. J. Cell Sci. *126*, 4239–4252.

Gomperts, M., Garcia-Castro, M., Wylie, C., and Heasman, J. (1994). Interactions between primordial germ cells play a role in their migration in mouse embryos. Development. *120*, 135–141.

Gonsior, S.M., Platz, S., Buchmeier, S., Scheer, U., Jockusch, B.M., and Hinssen, H. (1999). Conformational difference between nuclear and cytoplasmic actin as detected by a monoclonal antibody. J. Cell Sci. *112*, 797–809.

Goode, B.L., and Eck, M.J. (2007). Mechanism and function of formins in the control of actin assembly. Annu. Rev. Biochem. 593–627.

Gottlieb, T.M., and Jackson, S.P. (1993). The DNA-dependent protein kinase: Requirement for DNA ends and association with Ku antigen. Cell. *72*, 131–142.

Grawunder, U., Wilm, M., Wu, X., Kulesza, P., Wilson, T.E., Mann, M., and Lieber, M.R. (1997). Activity of DNA ligase IV stimulated by complex formation with XRCC4 protein in mammalian cells. Nature. *388*, 492–495.

Gray, S., and Cohen, P.E. (2016). Control of Meiotic Crossovers: From Double-Strand Break Formation to Designation. Annu. Rev. Genet. 175–210.

Grey, C., Barthès, P., Friec, G., Langa, F., Baudat, F., and de Massy, B. (2011). Mouse Prdm9 DNA-binding specificity determines sites of histone H3 lysine 4 trimethylation for initiation of meiotic recombination. PLoS Biol. *9*, e1001176.

Gulick, A.M., and Rayment, I. (1997). Structural studies on myosin II: Communication between distant protein domains. BioEssays. 561–569.

Haber, J.E. (2018). DNA Repair: The Search for Homology. BioEssays e1700229.

Hamer, G., Novak, I., Kouznetsova, A., and Höög, C. (2008). Disruption of pairing and synapsis of chromosomes causes stage-specific apoptosis of male meiotic cells. Theriogenology. *69*, 333–339.

Hartlerode, A.J., and Scully, R. (2009). Mechanisms of double-strand break repair in somatic mammalian cells. Biochem. J. 157–168.

Hartman, M.A., and Spudich, J.A. (2012). The myosin superfamily at a glance. J. Cell Sci. 1627–1632.

Hartshorne, G. (2013). Key events in early oogenesis affecting oocyte competence in women. In Textbook of Clinical Embryology, pp. 48–57.

Hassold, T., Hall, H., and Hunt, P. (2007). The origin of human aneuploidy: Where we have been, where we are going. Hum. Mol. Genet. R203–R208.

Hayashi, K., and Saitou, M. (2013). Generation of eggs from mouse embryonic stem cells and induced pluripotent stem cells. Nat. Protoc. *8*, 1513–1524.

Hejna, J., Holtorf, M., Hines, J., Mathewson, L., Hemphill, A., Al-Dhalimy, M., Olson, S.B., and Moses, R.E. (2008). Tip60 is required for DNA interstrand cross-link repair in the fanconi anemia pathway. J. Biol. Chem. *283*, 9844–9851.

Henson, J.H., Ditzler, C.E., Germain, A., Irwin, P.M., Vogt, E.T., Yang, S., Wu, X., and Shuster, C.B. (2017). The ultrastructural organization of actin and myosin II filaments in the contractile ring: New support for an old model of cytokinesis. Mol. Biol. Cell. *28*, 613–623.

Hernández-Hernández, A., Masich, S., Fukuda, T., Kouznetsova, A., Sandin, S., Daneholt, B., and Höög, C. (2016). The central element of the synaptonemal complex in mice is organized as a bilayered junction structure. J. Cell Sci. *129*, 2239–2249.

Hesterkamp, T., Weeds, A.G., and Mannherz, H.G. (1993). The actin monomers in the ternary gelsolin: 2 actin complex are in an antiparallel orientation. Eur. J. Biochem. *218*, 507–513.

Hetrick, B., Han, M.S., Helgeson, L.A., and Nolen, B.J. (2013). Small molecules CK-666 and CK-869 inhibit actin-related protein 2/3 complex by blocking an activating conformational change. Chem. Biol. *20*, 701–712.

Higgins, J.D., Buckling, E.F., Franklin, F.C.H., and Jones, G.H. (2008). Expression and functional analysis of AtMUS81 in Arabidopsis meiosis reveals a role in the second pathway of crossing-over. Plant J. *54*, 152–162.

Hikabe, O., Hamazaki, N., Nagamatsu, G., Obata, Y., Hirao, Y., Hamada, N., Shimamoto, S., Imamura, T., Nakashima, K., Saitou, M., et al. (2016). Reconstitution in vitro of the entire cycle of the mouse female germ line. Nature. *539*, 299–303.

Hollingsworth, N.M., and Brill, S.J. (2004). The Mus81 solution to resolution: Generating meiotic crossovers without Holliday junctions. Genes Dev. 117–125.

Hollingsworth, N.M., Ponte, L., and Halsey, C. (1995). MSH5, a novel MutS homolog, facilitates meiotic reciprocal recombination between homologs in Saccharomyces cerevisiae but not mismatch repair. Genes Dev. *9*, 1728–1739.

Holloway, J.K., Booth, J., Edelmann, W., McGowan, C.H., and Cohen, P.E. (2008). MUS81 generates a subset of MLH1-MLH3-independent crossovers in mammalian meiosis. PLoS Genet. *4*, e1000186.

Holloway, J.K., Morelli, M.A., Borst, P.L., and Cohen, P.E. (2010). Mammalian BLM helicase is critical for integrating multiple pathways of meiotic recombination. J. Cell Biol. *188*, 779–789.

Holloway, J.K., Mohan, S., Balmus, G., Sun, X., Modzelewski, A., Borst, P.L., Freire, R., Weiss, R.S., and Cohen, P.E. (2011). Mammalian BTBD12 (SLX4) protects against genomic instability during mammalian spermatogenesis. PLoS Genet. *6*, e1002094.

Hong, Y., Sonneville, R., Agostinho, A., Meier, B., Wang, B., Blow, J.J., and Gartner, A. (2016). The SMC-5/6 Complex and the HIM-6 (BLM) Helicase Synergistically Promote Meiotic Recombination Intermediate Processing and Chromosome Maturation during Caenorhabditis elegans Meiosis. PLoS Genet. *12*, e1005872.

Horan, C.J., and Williams, S.A. (2017). Oocyte stem cells: Fact or fantasy? Reproduction R23–R35.

Horn, H.F., Kim, D.I., Wright, G.D., Wong, E.S.M., Stewart, C.L., Burke, B., and Roux, K.J. (2013). A mammalian KASH domain protein coupling meiotic chromosomes to the cytoskeleton. J. Cell Biol. *202*, 1023–1039.

Houdusse, A., and Sweeney, H.L. (2016). How Myosin Generates Force on Actin Filaments. Trends Biochem. Sci. 989–997.

Hoyer-Fender, S. (2003). Molecular aspects of XY body formation. Cytogenet. Genome Res. 245–255.

Hsia, K.T., Millar, M.R., King, S., Selfridge, J., Redhead, N.J., Melton, D.W., and Saunders, P.T.K. (2003). DNA repair gene Ercc1 is essential for normal spermatogenesis and oogenesis and for functional integrity of germ cell DNA in the mouse. Development. 369–378.

Hu, Q., Tang, D., Wang, H., Shen, Y., Chen, X., Ji, J., Du, G., Li, Y., and Cheng, Z. (2016). The exonuclease homolog OsRAD1 promotes accurate meiotic double-strand break repair by suppressing nonhomologous end joining. Plant Physiol. *172*, 1105–1116.

Hunter, N., and Borts, R.H. (1997). Mlh1 is unique among mismatch repair proteins in its ability to promote crossing-over during meiosis. Genes Dev. *11*, 1573–1582.

Hwang, G., Verver, D.E., Handel, M.A., Hamer, G., and Jordan, P.W. (2018). Depletion of SMC5/6 sensitizes male germ cells to DNA damage. Mol. Biol. Cell. *29*, 3003–3016.

Hyun, S.J., Komatsu, S., Ikebe, M., and Craig, R. (2008). Head-head and head-tail interaction: A general mechanism for switching off myosin II activity in cells. Mol. Biol. Cell. *19*, 3234–3242.

Iftode, C., and Borowiec, J.A. (2000). 5' → 3' molecular polarity of human replication protein A (hRPA) binding to pseudo-origin DNA substrates. Biochemistry. *39*, 11970–11981.

Iida, K., Iida, H., and Yahara, I. (1986). Heat shock induction of intranuclear actin rods in cultured mammalian cells. Exp. Cell Res. *165*, 207–215.

Iida, K., Matsumoto, S., and Yahara, I. (1992). The KKRKK Sequence is Involved in Heat Shock-Induced Nuclear Translocation of the 18-kDa Actin-Binding Protein, Cofilin. Cell Struct. Funct. *17*, 39–46.

Ikebe, M., Hartshorne, D.J., and Elzinga, M. (1986). Identification, phosphorylation, and dephosphorylation of a second site for myosin light chain kinase on the 20,000-dalton light chain of smooth muscle myosin. J. Biol. Chem. *261*, 36–39.

Ikebe, M., Koretz, J., and Hartshorne, D.J. (1988). Effects of phosphorylation of light chain residues threonine 18 and serine 19 on the properties and conformation of smooth muscle myosin. J. Biol. Chem. *263*, 6432–6437.

Ikura, T., Ogryzko, V. V., Grigoriev, M., Groisman, R., Wang, J., Horikoshi, M., Scully, R., Qin, J., and Nakatani, Y. (2000). Involvement of the TIP60 histone acetylase complex in DNA repair and apoptosis. Cell. *102*, 463–473.

Ilatovskaya, D. V., Chubinskiy-Nadezhdin, V., Pavlov, T.S., Shuyskiy, L.S., Tomilin, V., Palygin, O., Staruschenko, A., and Negulyaev, Y.A. (2013). Arp2/3 complex inhibitors adversely affect actin cytoskeleton remodeling in the cultured murine kidney collecting duct M-1 cells. Cell Tissue Res. *354*, 783-792.

Ishiguro, K.I., Kim, J., Shibuya, H., Hernández-Hernández, A., Suzuki, A., Fukagawa, T., Shioi, G., Kiyonari, H., Li, X.C., Schimenti, J., et al. (2014). Meiosis-specific cohesin mediates homolog recognition in mouse spermatocytes. Genes Dev. *28*, 594–607.

Jagielio, G., and Fang, J. (1987). Observations on Chiasmata in Mouse Diplotene Oocytes and Spermatocytes. Cytologia (Tokyo). *52*, 283–292.

Jensen, R.B., Carreira, A., and Kowalczykowski, S.C. (2010). Purified human BRCA2 stimulates RAD51-mediated recombination. Nature. *467*, 678–683.

Jeong, H.C., Jeong, J.K., Jung, M.C., Jung, H.L., and Cho, Y. (2008). Crystal structure of the Mus81-Eme1 complex. Genes Dev. *22*, 1093–1106.

Jessop, L., and Lichten, M. (2008). Mus81/Mms4 Endonuclease and Sgs1 Helicase Collaborate to Ensure Proper Recombination Intermediate Metabolism during Meiosis. Mol. Cell. *31*, 313–323.

Jockusch, B.M., Brown, D.F., and Rusch, H.P. (1971). Synthesis and some properties of an actin-like nuclear protein in the slime mold Physarum polycephalum. J. Bacteriol. *108*, 705–714.

Joyce, E.F., Paul, A., Chen, K.E., Tanneti, N., and McKim, K.S. (2012). Multiple barriers to nonhomologous DNA end joining during meiosis in Drosophila. Genetics. *191*, 739–746.

Kan, F., Davidson, M.K., and Wahls, W.P. (2011). Meiotic recombination protein Rec12: Functional conservation, crossover homeostasis and early crossover/non-crossover decision. Nucleic Acids Res. *39*, 1460–1472.

Kaneda, Y., Nakajima, T., Nishikawa, T., Yamamoto, S., Ikegami, H., Suzuki, N., Nakamura, H., Morishita, R., and Kotani, H. (2002). Hemagglutinating virus of Japan (HVJ) envelope vector as a versatile gene delivery system. Mol. Ther. *6*, 219–226.

Kapoor, P., Chen, M., Winkler, D.D., Luger, K., and Shen, X. (2013). Evidence for monomeric actin function in INO80 chromatin remodeling. Nat. Struct. Mol. Biol. *20*, 426–432.

Kauppi, L., Barchi, M., Lange, J., Baudat, F., Jasin, M., and Keeney, S. (2013). Numerical constraints and feedback control of double-strand breaks in mouse meiosis. Genes Dev. *27*, 873–886.

Kaur, H., DeMuyt, A., and Lichten, M. (2015). Top3-Rmi1 DNA single-strand decatenase is integral to the formation and resolution of meiotic recombination intermediates. Mol. Cell. *57*, 583–594.

Keeney, S., and Kleckner, N. (1995). Covalent protein-DNA complexes at the 5′ strand termini of meiosis-specific double-strand breaks in yeast. Proc. Natl. Acad. Sci. U. S. A. *92*, 11274–11278.

Keeney, S., Giroux, C.N., and Kleckner, N. (1997). Meiosis-specific DNA double-strand breaks are catalyzed by Spo11, a member of a widely conserved protein family. Cell. *88*, 375–384.

Kelpsch, D.J., and Tootle, T.L. (2018). Nuclear Actin: From Discovery to Function. Anat. Rec. *301*, 1999–2013.

Kelpsch, D.J., Groen, C.M., Fagan, T.N., Sudhir, S., and Tootle, T.L. (2016). Fascin regulates nuclear actin during Drosophila oogenesis. Mol. Biol. Cell. *27*, 2965–2979.

Khalil, A.M., Boyar, F.Z., and Driscoll, D.J. (2004). Dynamic histone modifications mark sex chromosome inactivation and reactivation during mammalian spermatogenesis. Proc. Natl. Acad. Sci. U. S. A. *101*, 16583–16587.

Kikuchi, K., Narita, T., Pham, V.T., Iijima, J., Hirota, K., Keka, I.S., Mohiuddin, Okawa, K., Hori, T., Fukagawa, T., et al. (2013). Structure-specific endonucleases Xpf and Mus81 play overlapping but essential roles in DNA repair by homologous recombination. Cancer Res. *73*, 4352–4371.

Kitajima, T.S. (2018). Mechanisms of kinetochore-microtubule attachment errors in mammalian oocytes. Dev. Growth Differ. 33–43.

Kitajima, T.S., Miyazaki, Y., Yamamoto, M., and Watanabe, Y. (2003). Rec8 cleavage by separase is required for meiotic nuclear divisions in fission yeast. EMBO J. *22*, 5643–5653.

Klages-Mundt, N.L., Kumar, A., Zhang, Y., Kapoor, P., and Shen, X. (2018). The Nature of Actin-Family Proteins in Chromatin-Modifying Complexes. Front. Genet. *9*, 398.

Klein, F., Mahr, P., Galova, M., Buonomo, S.B.C., Michaelis, C., Nairz, K., and Nasmyth, K. (1999). A central role for cohesins in sister chromatid cohesion, formation of axial elements, and recombination during yeast meiosis. Cell. *98*, 91–103.

Kluin, P.M., Kramer, M.F., and de Rooij, D.G. (1982). Spermatogenesis in the immature mouse proceeds faster than in the adult. Int. J. Androl. *5*, 282–294.

Kneitz, B., Cohen, P.E., Avdievich, E., Zhu, L., Kane, M.F., Hou, H., Kolodner, R.D., Kucherlapati, R., Pollard, J.W., and Edelmann, W. (2000). MutS homolog 4 localization to meiotic chromosomes is required for chromosome pairing during meiosis in male and female mice. Genes Dev. *14*, 1085–1097.

Kogo, H., Tsutsumi, M., Ohye, T., Inagaki, H., Abe, T., and Kurahashi, H. (2012a). HORMAD1-dependent checkpoint/surveillance mechanism eliminates asynaptic oocytes. Genes Cells. *17*, 897–912.

Kogo, H., Tsutsumi, M., Inagaki, H., Ohye, T., Kiyonari, H., and Kurahashi, H. (2012b). HORMAD2 is essential for synapsis surveillance during meiotic prophase via the recruitment of ATR activity. Genes Cells. *17*, 439–454.

Kong, A., Gudbjartsson, D.F., Sainz, J., Jonsdottir, G.M., Gudjonsson, S.A., Richardsson, B., Sigurdardottir, S., Barnard, J., Hallbeck, B., Masson, G., et al. (2002). A high-resolution recombination map of the human genome. Nat. Genet. *31*, 241–247.

Kong, A., Thorleifsson, G., Gudbjartsson, D.F., Masson, G., Sigurdsson, A., Jonasdottir, A., Walters, G.B., Jonasdottir, A., Gylfason, A., Kristinsson, K.T., et al. (2010). Fine-scale recombination rate differences between sexes, populations and individuals. Nature. *467*, 1099–1103.

Korn, E.D. (2000). Coevolution of head, neck, and tail domains of myosin heavy chains. Proc. Natl. Acad. Sci. U. S. A. *97*, 12559–12564.

Koubova, J., Menke, D.B., Zhou, Q., Cape, B., Griswold, M.D., and Page, D.C. (2006). Retinoic acid regulates sex-specific timing of meiotic initiation in mice. Proc. Natl. Acad. Sci. U. S. A. *103*, 2474–2479.

Kovács, M., Wang, F., Hu, A., Zhang, Y., and Sellers, J.R. (2003). Functional divergence of human cytoplasmic myosin II. Kinetic characterization of the non-muscle IIA isoform. J. Biol. Chem. *278*, 38132–38140.

Krakup, T., Jakobsen, L.D., Jensen, B.S., and Hoffmann, E.K. (1998). Na+-K+-2Cl- cotransport in Ehrlich cells: Regulation by protein phosphatases and kinases. Am. J. Physiol. - Cell Physiol. *275*, C239-250.

Kumar, S., Chatzi, C., Brade, T., Cunningham, T.J., Zhao, X., and Duester, G. (2011). Sex-specific timing of meiotic initiation is regulated by Cyp26b1 independent of retinoic acid signalling. Nat. Commun. *2*, 151.

Kusumoto, R., Dawut, L., Marchetti, C., Jae, W.L., Vindigni, A., Ramsden, D., and Bohr, V.A. (2008). Werner protein cooperates with the XRCC4-DNA ligase IV complex in end-processing. Biochemistry. *47*, 7548–7556.

Lam, I., and Keeney, S. (2015). Mechanism and regulation of meiotic recombination initiation. Cold Spring Harb. Perspect. Biol. *7*, a016634.

Lane, N.J. (1969). Intranuclear fibrillar bodies in actinomycin D-treated oocytes. J. Cell Biol. *40*, 286–291.

Lane, S., and Kauppi, L. (2019). Meiotic spindle assembly checkpoint and aneuploidy in males versus females. Cell. Mol. Life Sci. 1135–1150.

De Lanerolle, P. (2012). Nuclear actin and myosins at a glance. J. Cell Sci. *125*, 4945–4949.
Lange, J., Pan, J., Cole, F., Thelen, M.P., Jasin, M., and Keeney, S. (2011). ATM controls meiotic double-strand-break formation. Nature. *479*, 237–240.

Lawson, K.A., and Hage, W.J. (1994). Clonal analysis of the origin of primordial germ cells in the mouse. Ciba Found. Symp. 68–84.

Lee, C.Y., Horn, H.F., Stewart, C.L., Burke, B., Bolcun-Filas, E., Schimenti, J.C., Dresser, M.E., and Pezza, R.J. (2015). Mechanism and Regulation of Rapid Telomere Prophase Movements in Mouse Meiotic Chromosomes. Cell Rep. *11*, 551–563.

Lessard, J.L. (1988). Two monoclonal antibodies to actin: one muscle selective and one generally reactive. Cell Motil. Cytoskeleton. *10*, 349–362.

Lestourgeon, W.M., Forer, A., Yang, Y.Z., Bertram, J.S., and Rusch, H.P. (1975). Contractile proteins. Major components of nuclear and chromosome non-histone proteins. BBA - Protein Struct. *379*, 529–552.

Li, B., and Comai, L. (2001). Requirements for the Nucleolytic Processing of DNA Ends by the Werner Syndrome Protein-Ku70/80 Complex. J. Biol. Chem. *276*, 9896–9902.

Li, X., and Schimenti, J.C. (2007). Mouse pachytene checkpoint 2 (Trip13) is required for completing meiotic recombination but not synapsis. PLoS Genet. *3*, e130.

Li, H., MacLean, G., Cameron, D., Clagett-Dame, M., and Petkovich, M. (2009). Cyp26b1 expression in murine sertoli cells is required to maintain male germ cells in an undifferentiated state during embryogenesis. PLoS One. *4*, e7501.

Link, J., Leubner, M., Schmitt, J., Göb, E., Benavente, R., Jeang, K.T., Xu, R., and Alsheimer, M. (2014). Analysis of Meiosis in SUN1 Deficient Mice Reveals a Distinct Role of SUN2 in Mammalian Meiotic LINC Complex Formation and Function. PLoS Genet. *10*, e1004099.

Lipkin, S.M., Moens, P.B., Wang, V., Lenzi, M., Shanmugarajah, D., Gilgeous, A., Thomas, J., Cheng, J., Touchman, J.W., Green, E.D., et al. (2002). Meiotic arrest and aneuploidy in MLH3-deficient mice. Nat. Genet. *31*, 385–390.

Liu, J., Wu, T.C., and Lichten, M. (1995). The location and structure of double-strand DNA breaks induced during yeast meiosis: Evidence for a covalently linked DNA-protein intermediate. EMBO J. *14*, 4599–4608.

De los Santos, T., Hunter, N., Lee, C., Larkin, B., Loidl, J., and Hollingsworth, N.M. (2003). The MUS81/MMS4 endonuclease acts independently of double-holliday junction resolution to promote a distinct subset of crossovers during meiosis in budding yeast. Genetics. *164*, 81–94.

Lukas, C., Melander, F., Stucki, M., Falck, J., Bekker-Jensen, S., Goldberg, M., Lerenthal, Y., Jackson, S.P., Bartek, J., and Lukas, J. (2004). Mdc1 couples DNA double-strand break recognition by Nbs1 with its H2AX-dependent chromatin retention. EMBO J. *23*, 2674–2683.

Lukaszewicz, A., Shodhan, A., and Loidl, J. (2015). Exo1 and Mre11 execute meiotic DSB end resection in the protist Tetrahymena. DNA Repair (Amst). *35*, 137–143.

Lydall, D., Nikolsky, Y., Bishop, D.K., and Weinert, T. (1996). A meiotic recombination checkpoint controlled by mitotic checkpoint genes. Nature. *383*, 840–843.

Ma, C.J., Kwon, Y., Sung, P., and Greene, E.C. (2017a). Human RAD52 interactions with replication protein a and the RAD51 presynaptic complex. J. Biol. Chem. *292*, 11702–11713.

Ma, X., Kovaćs, M., Conti, M.A., Wang, A., Zhang, Y., Sellers, J.R., and Adelstein, R.S. (2012). Nonmuscle myosin II exerts tension but does not translocate actin in vertebrate cytokinesis. Proc. Natl. Acad. Sci. U. S. A. *109*, 4509–4514.

Ma, Y., Pannicke, U., Schwarz, K., and Lieber, M.R. (2002). Hairpin opening and overhang processing by an Artemis/DNA-dependent protein kinase complex in nonhomologous end joining and V(D)J recombination. Cell. *108*, 781–794.

Ma, Y., Wang, M., Li, W., Zhang, Z., Zhang, X., Tan, T., Zhang, X.E., and Cui, Z. (2017b). Live cell imaging of single genomic loci with quantum dot-labeled TALEs. Nat. Commun. *8*, 15318.

Macaisne, N., Kessler, Z., and Yanowitz, J.L. (2018). Meiotic double-strand break proteins influence repair pathway utilization. Genetics. *210*, 843–856.

MacLean, G., Abu-Abed, S., Dolle, D., Tahayato, A., Chambon, P., and Petkovich, M. (2001). Cloning of a novel retinoic-acid metabolizing cytochrome P450, Cyp26B1, and comparative expression analysis with Cyp26A1 during early murine development. Mech. Dev. 195–201.

Manhart, C.M., and Alani, E. (2016). Roles for mismatch repair family proteins in promoting meiotic crossing over. DNA Repair (Amst). 84–93.

Martin, J.S., Winkelmann, N., Petalcorin, M.I.R., McIlwraith, M.J., and Boulton, S.J. (2005). RAD-51-Dependent and -Independent Roles of a Caenorhabditis elegans BRCA2-Related Protein during DNA Double-Strand Break Repair. Mol. Cell. Biol. *25*, 3127–3139.

Martini, E., Diaz, R.L., Hunter, N., and Keeney, S. (2006). Crossover Homeostasis in Yeast Meiosis. Cell. *126*, 285–295.

Maslova, A., and Krasikova, A. (2012). Nuclear actin depolymerisation in transcriptionally active avian and amphibian oocytes leads to collapse of intranuclear structures. Nucleus (United States). *3*, 300–311.

De Massy, B., Rocco, V., and Nicolas, A. (1995). The nucleotide mapping of DNA double-strand breaks at the CYS3 initiation site of meiotic recombination in Saccharomyces cerevisiae. EMBO J. *14*, 4589–4598.

Masurovsky, E.B., Benitez, H.H., Kim, S.U., and Murray, M.R. (1970). Origin, development, and nature of intranuclear rodlets and associated bodies in chicken sympathetic neurons. J. Cell Biol. *44*, 172–191.

Mateos-Gomez, P.A., Kent, T., Deng, S.K., Mcdevitt, S., Kashkina, E., Hoang, T.M., Pomerantz, R.T., and Sfeir, A. (2017). The helicase domain of Polθ counteracts RPA to promote alt-NHEJ. Nat. Struct. Mol. Biol. *24*, 1116–1123.

Matsuoka, S., Ballif, B.A., Smogorzewska, A., McDonald, E.R., Hurov, K.E., Luo, J., Bakalarski, C.E., Zhao, Z., Solimini, N., Lerenthal, Y., et al. (2007). ATM and ATR substrate analysis reveals extensive protein networks responsive to DNA damage. Science. *316*, 1160–1166.

Matsuzaki, F., Matsumoto, S., Yahara, I., Yonezawa, N., Nishida, E., and Sakai, H. (1988). Cloning and characterization of porcine brain cofilin cDNA. Cofilin contains the nuclear transport signal sequence. J. Biol. Chem. *263*, 11564–11568.

McDonald, D., Carrero, G., Andrin, C., De Vries, G., and Hendzel, M.J. (2006). Nucleoplasmic β-actin exists in a dynamic equilibrium between low-mobility polymeric species and rapidly diffusing populations. J. Cell Biol. *172*, 541–552.

McGough, A., Pope, B., Chiu, W., and Weeds, A. (1997). Cofilin changes the twist of F-actin: Implications for actin filament dynamics and cellular function. J. Cell Biol. *138*, 771–781.

McLaren, A. (2000). Germ and somatic cell lineages in the developing gonad. Mol. Cell. Endocrinol. *163*, 3–9.

McLaren, A., and Southee, D. (1997). Entry of mouse embryonic germ cells into meiosis. Dev. Biol. *187*, 107–113.

McLean, D.J., Friel, P.J., Johnston, D.S., and Griswold, M.D. (2003). Characterization of Spermatogonial Stem Cell Maturation and Differentiation in Neonatal Mice. Biol. Reprod. *69*, 2085–2091.

McMahill, M.S., Sham, C.W., and Bishop, D.K. (2007). Synthesis-dependent strand annealing in meiosis. PLoS Biol. *5*, e299.

McVey, M., Khodaverdian, V.Y., Meyer, D., Cerqueira, P.G., and Heyer, W.D. (2016). Eukaryotic DNA Polymerases in Homologous Recombination. Annu. Rev. Genet. 393–421.

Meuwissen, R.L.J., Offenberg, H.H., Dietrich, A.J.J., Riesewijk, A., Van Iersel, M., and Heyting, C. (1992). A coiled-coil related protein specific for synapsed regions of meiotic prophase chromosomes. EMBO J. *11*, 5091–5100.

Miki, T., Okawa, K., Sekimoto, T., Yoneda, Y., Watanabe, S., Ishizaki, T., and Narumiya, S. (2009). mDia2 shuttles between the nucleus and the cytoplasm through the importin-α/β- and CRM1-mediated nuclear transport mechanism. J. Biol. Chem. *284*, 5753–5762.

Millonig, R., Salvo, H., and Aebi, U. (1988). Probing actin polymerization by intermolecular cross-linking. J. Cell Biol. *106*, 785–796.

Miranda, A.F., and Godman, G.C. (1973). The effects of cytochalasin D on differentiating muscle in culture. Tissue Cell. *5*, 1–22.

Miyanari, Y., Ziegler-Birling, C., and Torres-Padilla, M.E. (2013). Live visualization of chromatin dynamics with fluorescent TALEs. Nat. Struct. Mol. Biol. *20*, 1321–1324.

Moens, P.B., Kolas, N.K., Tarsounas, M., Marcon, E., Cohen, P.E., and Spyropoulos, B. (2002). The time course and chromosomal localization of recombination-related proteins at meiosis in the mouse are compatible with models that can resolve the early DNA-DNA interactions without reciprocal recombination. J. Cell Sci. *115*, 1611–1622.

Morano, I., Chai, G, X., Baltas, L.G., Lamounier-Zepter, V., Lutsch, G., Kott, M., Haase, H., and Bader, M. (2000). Smooth-muscle contraction without smooth-muscle myosin. Nat. Cell Biol. *2*, 371–375.

Morelli, M.A., Werling, U., Edelmann, W., Roberson, M.S., and Cohen, P.E. (2008). Analysis of meiotic prophase I in live mouse spermatocytes. Chromosom. Res. *16*, 743–760.

Morimoto, A., Shibuya, H., Zhu, X., Kim, J., Ishiguro, K.I., Han, M., and Watanabe, Y. (2012). A conserved KASH domain protein associates with telomeres, SUN1, and dynactin during mammalian meiosis. J. Cell Biol. *198*, 165–172.

Morohaku, K., Tanimoto, R., Sasaki, K., Kawahara-Miki, R., Kono, T., Hayashi, K., Hirao, Y., and Obata, Y. (2016). Complete in vitro generation of fertile oocytes from mouse primordial germ cells. Proc. Natl. Acad. Sci. U. S. A. *113*, 9021–9026.

Munsie, L.N., Desmond, C.R., and Truant, R. (2012). Cofilin nuclear-cytoplasmic shuttling affects cofilin-actin rod formation during stress. J. Cell Sci. *125*, 3977–3988.

De Muyt, A., Jessop, L., Kolar, E., Sourirajan, A., Chen, J., Dayani, Y., and Lichten, M. (2012). BLM Helicase Ortholog Sgs1 Is a Central Regulator of Meiotic Recombination Intermediate Metabolism. Mol. Cell. *46*, 43–53.

Myers, S., Freeman, C., Auton, A., Donnelly, P., and McVean, G. (2008). A common sequence motif associated with recombination hot spots and genome instability in humans. Nat. Genet. *40*, 1124–1129.

Myers, S., Bowden, R., Tumian, A., Bontrop, R.E., Freeman, C., MacFie, T.S., McVean, G., and Donnelly, P. (2010). Drive against hotspot motifs in primates implicates the PRDM9 gene in meiotic recombination. Science. *327*, 876–879.

Nambiar, M., and Smith, G.R. (2016). Repression of harmful meiotic recombination in centromeric regions. Semin. Cell Dev. Biol. 188–197.

Nambiar, M., and Smith, G.R. (2018). Pericentromere-Specific Cohesin Complex Prevents Meiotic Pericentric DNA Double-Strand Breaks and Lethal Crossovers. Mol. Cell. *71*, 540–553.

Neale, M.J., Pan, J., and Keeney, S. (2005). Endonucleolytic processing of covalent protein-linked DNA double-strand breaks. Nature. *436*, 1053–1057.

Nevzorov, I., Sidorenko, E., Wang, W., Zhao, H., and Vartiainen, M.K. (2018). Myosin-1C uses a novel phosphoinositide-dependent pathway for nuclear localization. EMBO Rep. *19*, 290–304.

Niederman, R., and Pollard, T.D. (1975). Human platelet myosin: II. In vitro assembly and structure of myosin filaments. J. Cell Biol. *67*, 72–92.

Nimonkar, A. V., Genschel, J., Kinoshita, E., Polaczek, P., Campbell, J.L., Wyman, C., Modrich, P., and Kowalczykowski, S.C. (2011). BLM-DNA2-RPA-MRN and EXO1-BLM-RPA-MRN constitute two DNA end resection machineries for human DNA break repair. Genes Dev. *25*, 350–362.

Nishida, E., Iida, K., Yonezawa, N., Koyasu, S., Yahara, I., and Sakai, H. (1987). Cofilin is a component of intranuclear and cytoplasmic actin rods induced in cultured cells. Proc. Natl. Acad. Sci. U. S. A. *84*, 5262–5266.

Nowak, G., Pestic-Dragovich, L., Hozák, P., Philimonenko, A., Simerly, C., Schatten, G., and De Lanerolle, P. (1997). Evidence for the presence of myosin I in the nucleus. J. Biol. Chem. *272*, 17176–17181.

O'Connell, C.B., Tyska, M.J., and Mooseker, M.S. (2007). Myosin at work: Motor adaptations for a variety of cellular functions. Biochim. Biophys. Acta - Mol. Cell Res. 615–630.

O'Keeffe, C., Hultén, M.A., and Tease, C. (1997). Analysis of proximal X chromosome pairing in early female mouse meiosis. Chromosoma. *106*, 276–283.

O'Neil, N.J., Martin, J.S., Youds, J.L., Ward, J.D., Petalcorin, M.I.R., Rose, A.M., and Boulton, S.J. (2013). Joint Molecule Resolution Requires the Redundant Activities of MUS-81 and XPF-1 during Caenorhabditis elegans Meiosis. PLoS Genet. *9*, e1003582.

Oh, S.D., Lao, J.P., Hwang, P.Y.H., Taylor, A.F., Smith, G.R., and Hunter, N. (2007). BLM Ortholog, Sgs1, Prevents Aberrant Crossing-over by Suppressing Formation of Multichromatid Joint Molecules. Cell. *130*, 258–272.

Oliver-Bonet, M., Campillo, M., Turek, P.J., Ko, E., and Martin, R.H. (2007). Analysis of replication protein A (RPA) in human spermatogenesis. Mol. Hum. Reprod. *13*, 837–844.

Orelli, B., McClendon, T.B., Tsodikov, O. V., Ellenberger, T., Niedernhofer, L.J., and Schärer, O.D. (2010). The XPA-binding domain of ERCC1 is required for nucleotide excision repair but not other DNA repair pathways. J. Biol. Chem. *285*, 3705–3712.

Osman, F., Dixon, J., Doe, C.L., and Whitby, M.C. (2003). Generating crossovers by resolution of nicked Holliday junctions: A role for Mus81-Eme1 in meiosis. Mol. Cell. *12*, 761–774.

Otomo, T., Tomchick, D.R., Otomo, C., Panchal, S.C., Machius, M., and Rosen, M.K. (2005). Structural basis of actin filament nucleation and processive capping by a formin homology 2 domain. Nature. *433*, 488–494.

Pacheco, S., Marcet-Ortega, M., Lange, J., Jasin, M., Keeney, S., and Roig, I. (2015). The ATM Signaling Cascade Promotes Recombination-Dependent Pachytene Arrest in Mouse Spermatocytes. PLoS Genet. *11*, e1005017.

Page, S.L., and Hawley, R.S. (2003). Chromosome choreography: The meiotic ballet. Science. 785–789.

Parfenov, V.., Davis, D.., Pochukalina, G.., Sample, C.., Bugaeva, E.., and Murti, K.. (1995). Nuclear actin filaments and their topological changes in frog oocytes. Exp. Cell Res. *217*, 385–394.

Park, E.J., Hur, S.K., and Kwon, J. (2010). Human INO80 chromatin-remodelling complex contributes to DNA double-strand break repair via the expression of Rad54B and XRCC3 genes. Biochem. J. *431*, 179–187.

Pendleton, A., Pope, B., Weeds, A., and Koffer, A. (2003). Latrunculin B or ATP depletion induces cofilin-dependent translocation of actin into nuclei of mast cells. J. Biol. Chem. *278*, 14394–14400.

Perrin, B.J., and Ervasti, J.M. (2010). The actin gene family: Function follows isoform. Cytoskeleton. *67*, 630–634.

Pestic-Dragovich, L., Stojiljkovic, L., Philimonenko, A.A., Nowak, G., Ke, Y., Settlage, R.E., Shabanowitz, J., Hunt, D.F., Hozak, P., and De Lanerolle, P. (2000). A myosin I isoform in the nucleus. Science. *290*, 337–341.

Pfeifer, C., Thomsen, P.D., and Scherthan, H. (2001). Centromere and telomere redistribution precedes homologue pairing and terminal synapsis initiation during prophase I of cattle spermatogenesis. Cytogenet. Cell Genet. *93*, 304–314.

Pfeifer, C., Scherthan, H., and Thomsen, P.D. (2003). Sex-specific telomere redistribution and synapsis initiation in cattle oogenesis. Dev. Biol. *255*, 206–215.

Pfitzer, L., Moser, C., Gegenfurtner, F., Arner, A., Foerster, F., Atzberger, C., Zisis, T., Kubisch-Dohmen, R., Busse, J., Smith, R., et al. (2019). Targeting actin inhibits repair of doxorubicin-induced DNA damage: a novel therapeutic approach for combination therapy. Cell Death Dis. *10*, 302.

Phillips, C.M., and Dernburg, A.F. (2006). A Family of Zinc-Finger Proteins Is Required for Chromosome-Specific Pairing and Synapsis during Meiosis in C. elegans. Dev. Cell. *11*, 817–829.

Phillips, C.M., Meng, X., Zhang, L., Chretien, J.H., Urnov, F.D., and Dernburg, A.F. (2009). Identification of chromosome sequence motifs that mediate meiotic pairing and synapsis in C. elegans. Nat. Cell Biol. *11*, 934–942.

Pittman, D.L., Cobb, J., Schimenti, K.J., Wilson, L.A., Cooper, D.M., Brignull, E., Handel, M.A., and Schimenti, J.C. (1998). Meiotic prophase arrest with failure of chromosome synapsis in mice deficient for Dmc1, a germline-specific RecA homolog. Mol. Cell. *1*, 697–705.

Plug, A.W., Peters, A.H.F.M., Keegan, K.S., Hoekstra, M.F., De Boer, P., and Ashley, T. (1998). Changes in protein composition of meiotic nodules during mammalian meiosis. J. Cell Sci. *111*, 413–423.

Polani, P.E. (1972). Centromere localization at meiosis and the position of chiasmata in the male and female mouse. Chromosoma. *36*, 343–374.

Pollard, T.D. (2016). Actin and actin-binding proteins. Cold Spring Harb. Perspect. Biol. *8*, a018226.

Pollard, T.D., Earnshaw, W.C., Lippincott-Schwartz, J., and Johnson, G.T. (2017). Cell Biology: Third Edition.

Potter, H., and Heller, R. (2003). Transfection by electroporation. Curr. Protoc. Mol. Biol. 9.3.

Prakash, K., Fournier, D., Redl, S., Best, G., Borsos, M., Tiwari, V.K., Tachibana-Konwalski, K., Ketting, R.F., Parekh, S.H., Cremer, C., et al. (2015). Superresolution imaging reveals structurally distinct periodic patterns of chromatin along pachytene chromosomes. Proc. Natl. Acad. Sci. U. S. A. *112*, 14635–14640.

Pring, M., Evangelista, M., Boone, C., Yang, C., and Zigmond, S.H. (2003). Mechanism of formin-induced nucleation of actin filaments. Biochemistry. *42*, 486–496.

Qu, Z., Silvan, U., Jockusch, B.M., Aebi, U., Schoenenberger, C.A., and Mannherz, H.G. (2015). Distinct actin oligomers modulate differently the activity of actin nucleators. FEBS J. *282*, 3824–2840.

Quinlan, M.E., Heuser, J.E., Kerkhoff, E., and Mullins, R.D. (2005). Drosophila Spire is an actin nucleation factor. Nature. *433*, 382–388.

Ragunathan, K., Liu, C., and Ha, T. (2012). RecA filament sliding on DNA facilitates homology search. Elife. *1*, e00067.

Ramsden, D.A. (2011). Polymerases in nonhomologous end joining: Building a bridge over broken chromosomes. Antioxidants Redox Signal. 2509–2519.

Ramsden, D.A., and Geliert, M. (1998). Ku protein stimulates DNA end joining by mammalian DNA ligases: A direct role for Ku in repair of DNA double-strand breaks. EMBO J. *17*, 609–614.

Ranjha, L., Anand, R., and Cejka, P. (2014). The Saccharomyces cerevisiae Mlh1-Mlh3 heterodimer is an endonuclease that preferentially binds to holliday junctions. J. Biol. Chem. *289*, 5674–5686.

Raposo, G., Cordonnier, M.N., Tenza, D., Menichi, B., Dürrbach, A., Louvard, D., and Coudrier, E. (1999). Association of myosin I alpha with endosomes and lysosomes in mammalian cells. Mol. Biol. Cell. *10*, 1477–1494.

Rasmussen, S.W., and Holm, P.B. (1984). The synaptonemal complex, recombination nodules and chiasmata in human spermatocytes. Symp. Soc. Exp. Biol. *38*, 271–292.

Rass, E., Grabarz, A., Plo, I., Gautier, J., Bertrand, P., and Lopez, B.S. (2009). Role of Mre11 in chromosomal nonhomologous end joining in mammalian cells. Nat. Struct. Mol. Biol. *16*, 818–824.

Rayment, I., Rypniewski, W.R., Schmidt-Bäse, K., Smith, R., Tomchick, D.R., Benning, M.M., Winkelmann, D.A., Wesenberg, G., and Holden, H.M. (1993). Three-dimensional structure of myosin subfragment-1: A molecular motor. Science. *261*, 50–58.

Raynard, S., Bussen, W., and Sung, P. (2006). A double holliday junction dissolvasome comprising BLM, topoisomerase IIIα, and BLAP75. J. Biol. Chem. *281*, 13861–13864.

Renaud, E., Barascu, A., and Rosselli, F. (2016). Impaired TIP60-mediated H4K16 acetylation accounts for the aberrant chromatin accumulation of 53BP1 and RAP80 in Fanconi anemia pathway-deficient cells. Nucleic Acids Res. *44*, 648–656.

Renkawitz, J., Lademann, C.A., Kalocsay, M., and Jentsch, S. (2013). Monitoring Homology Search during DNA Double-Strand Break Repair In Vivo. Mol. Cell. *50*, 261–272.

Rinaldi, V.D., Bolcun-Filas, E., Kogo, H., Kurahashi, H., and Schimenti, J.C. (2017). The DNA Damage Checkpoint Eliminates Mouse Oocytes with Chromosome Synapsis Failure. Mol. Cell. *67*, 1026-1036.e2.

Rinaldi, V.D., Bloom, J.C., and Schimenti, J.C. (2020). Oocyte elimination through DNA damage signaling from CHK1/CHK2 to p53 and p63. Genetics. *215*, 373–378.

Robinson, R.C., Turbedsky, K., Kaiser, D.A., Marchand, J.B., Higgs, H.N., Choe, S., and Pollard, T.D. (2001). Crystal structure of Arp2/3 complex. Science. *294*, 1679–1684.

Rockmill, B., Sym, M., Scherthan, H., and Shirleen Roeder, G. (1995). Roles for two RecA homologs in promoting meiotic chromosome synapsis. Genes Dev. *9*, 2684–2695.

Rodal, A.A., Sokolova, O., Robins, D.B., Daugherty, K.M., Hippenmeyer, S., Riezman, H., Grigorieff, N., and Goode, B.L. (2005). Conformational changes in the Arp2/3 complex leading to actin nucleation. Nat. Struct. Mol. Biol. *12*, 26–31.

Rodgers, K., and Mcvey, M. (2016). Error-Prone Repair of DNA Double-Strand Breaks. J. Cell. Physiol. 15–24.

Roeder, G.S., and Bailis, J.M. (2000). The pachytene checkpoint. Trends Genet. 395–403.

Rogacheva, M. V., Manhart, C.M., Chen, G., Guarne, A., Surtees, J., and Alani, E. (2014). Mlh1-Mlh3, a meiotic crossover and DNA mismatch repair factor, is a Msh2-Msh3-stimulated endonuclease. J. Biol. Chem. *289*, 5664–5673.

Rogakou, E.P., Pilch, D.R., Orr, A.H., Ivanova, V.S., and Bonner, W.M. (1998). DNA double-stranded breaks induce histone H2AX phosphorylation on serine 139. J. Biol. Chem. *273*, 5858.

Roig, I., Dowdle, J.A., Toth, A., de Rooij, D.G., Jasin, M., and Keeney, S. (2010). Mouse TRIP13/PCH2 is required for recombination and normal higher-order chromosome structure during meiosis. PLoS Genet. *6*, e1001062.

Roland, J.T., Kenworthy, A.K., Peranen, J., Caplan, S., and Goldenring, J.R. (2007). Myosin Vb interacts with Rab8a on a tubular network containing EHD1 and EHD3. Mol. Biol. Cell. *18*, 2828–2837.

Romanienko, P.J., and Camerini-Otero, R.D. (2000). The mouse Spo11 gene is required for meiotic chromosome synapsis. Mol. Cell. *6*, 975–987.

de Rooij, D.G. (2001). Proliferation and differentiation of spermatogonial stem cells. Reproduction. 347–354.

Ross-Macdonald, P., and Roeder, G.S. (1994). Mutation of a meiosis-specific MutS homolog decreases crossing over but not mismatch correction. Cell. *79*, 1069–1080.

Rotty, J.D., Wu, C., and Bear, J.E. (2013). New insights into the regulation and cellular functions of the ARP2/3 complex. Nat. Rev. Mol. Cell Biol. *14*, 7–12.

Rouiller, I., Xu, X.P., Amann, K.J., Egile, C., Nickell, S., Nicastro, D., Li, R., Pollard, T.D., Volkmann, N., and Hanein, D. (2008). The structural basis of actin filament branching by the Arp2/3 complex. J. Cell Biol. *180*, 887–895.

Royo, H., Polikiewicz, G., Mahadevaiah, S.K., Prosser, H., Mitchell, M., Bradley, A., De Rooij, D.G., Burgoyne, P.S., and Turner, J.M.A. (2010). Evidence that meiotic sex chromosome inactivation is essential for male fertility. Curr. Biol. *20*, 2117–2123.

Rusk, N. (2009). Reverse ChIP. Nat. Methods. *6*, 187.

Ryser, U. (1970). The ultrastructure of mitotic nuclei in plasmodia of Physarum polycephalum. Zeitschrift Für Zellforsch. Und Mikroskopische Anat. *110*, 108–130.

Saitoh, M., Ishikawa, T., Matsushima, S., Naka, M., and Hidaka, H. (1987). Selective inhibition of catalytic activity of smooth muscle myosin light chain kinase. J. Biol. Chem. *262*, 7796–7801.

Sakakibara, Y., Hashimoto, S., Nakaoka, Y., Kouznetsova, A., Höög, C., and Kitajima, T.S. (2015). Bivalent separation into univalents precedes age-related meiosis i errors in oocytes. Nat. Commun. *6*, 7550.

Salas-Cortes, L., Ye, F., Tenza, D., Wilhelm, C., Theos, A., Louvard, D., Raposo, G., and Coudrier, E. (2005). Myosin lb modulates the morphology and the protein transport within multi-vesicular sorting endosomes. J. Cell Sci. *118*, 4823–4832.

San-Segundo, P.A., and Shirleen Roeder, G. (1999). Pch2 links chromatin silencing to meiotic checkpoint control. Cell. *97*, 313–324.

Sandhu, R., Monge Neria, F., Monge Neria, J., Chen, X., Hollingsworth, N.M., and Börner, G. V. (2020). DNA Helicase Mph1FANCM Ensures Meiotic Recombination between Parental Chromosomes by Dissociating Precocious Displacement Loops. Dev. Cell. *53*, 458-472.e5.

Santucci-Darmanin, S., Walpita, D., Lespinasse, F., Desnuelle, C., Ashley, T., and Paquis-Flucklinger, V. (2000). MSH4 acts in conjunction with MLH1 during mammalian meiosis. FASEB J. *14*, 1539–1547.

Sasanuma, H., Murakami, H., Fukuda, T., Shibata, T., Nicolas, A., and Ohta, K. (2007). Meiotic association between Spo11 regulated by Rec102, Rec104 and Rec114. Nucleic Acids Res. *35*, 1119–1133.

Sato, T., Katagiri, K., Kubota, Y., and Ogawa, T. (2013). In vitro sperm production from mouse spermatogonial stem cell lines using an organ culture method. Nat. Protoc. *8*, 2098–2104.

Scheer, U., Hinssen, H., Franke, W.W., and Jockusch, B.M. (1984). Microinjection of actin-binding proteins and actin antibodies demonstrates involvement of nuclear actin in transcription of lampbrush chromosomes. Cell. *39*, 111–122.

Scherthan, H., and Schönborn, I. (2001). Asynchronous chromosome pairing in male meiosis of the rat (Rattus norvegicus). Chromosom. Res. *9*, 273–282.

Scherthan, H., Weich, S., Schwegler, H., Heyting, C., Härle, M., and Cremer, T. (1996). Centromere and telomere movements during early meiotic prophase of mouse and man are associated with the onset of chromosome pairing. J. Cell Biol. *134*, 1109–1125.

Scherthan, H., Eils, R., Trelles-Sticken, E., Dietzel, S., Cremer, T., Walt, H., and Jauch, A. (1998). Aspects of three-dimensional chromosome reorganization during the onset of human male meiotic prophase. J. Cell Sci. *111*, 2337–2351.

Schild-Prüfert, K., Saito, T.T., Smolikov, S., Gu, Y., Hincapie, M., Hill, D.E., Vidal, M., McDonald, K., and Colaiácovo, M.P. (2011). Organization of the synaptonemal complex during meiosis in Caenorhabditis elegans. Genetics. *189*, 411–421.

Schoenenberger, C.A., Buchmeier, S., Boerries, M., Sütterlin, R., Aebi, U., and Jockusch, B.M. (2005). Conformation-specific antibodies reveal distinct actin structures in the nucleus and the cytoplasm. J. Struct. Biol. *152*, 157–168.

Schoenmakers, S., Wassenaar, E., van Cappellen, W.A., Derijck, A.A., de Boer, P., Laven, J.S.E., Grootegoed, J.A., and Baarends, W.M. (2008). Increased frequency of asynapsis and associated meiotic silencing of heterologous chromatin in the presence of irradiation-induced extra DNA double strand breaks. Dev. Biol. *317*, 270–281.

Schrank, B.R., Aparicio, T., Li, Y., Chang, W., Chait, B.T., Gundersen, G., Gottesman, M.E., and Gautier, J. (2018). Nuclear ARP2/3 drives DNA break clustering for homology-directed repair. Nature. *559*, 61–66.

Schücker, K., Holm, T., Franke, C., Sauer, M., and Benavente, R. (2015). Elucidation of synaptonemal complex organization by super-resolution imaging with isotropic resolution. Proc. Natl. Acad. Sci. U. S. A. *112*, 2029–2033.

Schwacha, A., and Kleckner, N. (1997). Interhomolog bias during meiotic recombination: Meiotic functions promote a highly differentiated interhomolog-only pathway. Cell. *90*, 1123–1135.

Sellers, J.R. (2000). Myosins: A diverse superfamily. Biochim. Biophys. Acta - Mol. Cell Res. 3–22.

Sept, D., and McCammon, J.A. (2001). Thermodynamics and kinetics of actin filament nucleation. Biophys. J. *81*, 667–674.

Shannon, M., Lamerdin, J.E., Richardson, L., McCutchen-Maloney, S.L., Hwang, M.H., Handel, M.A., Stubbs, L., and Thelen, M.P. (1999). Characterization of the mouse Xpf DNA repair gene and differential expression during spermatogenesis. Genomics. *62*, 427–435.

Shi, B., Xue, J., Yin, H., Guo, R., Luo, M., Ye, L., Shi, Q., Huang, X., Liu, M., Sha, J., et al. (2019). Dual functions for the ssDNA-binding protein RPA in meiotic recombination. PLoS Genet. *15*, e1007952.

Shibuya, H., and Watanabe, Y. (2018). Live-cell microscopy of meiosis in spermatocytes. In Methods in Cell Biology, pp. 269–277.

Shibuya, H., Ishiguro, K.I., and Watanabe, Y. (2014a). The TRF1-binding protein TERB1 promotes chromosome movement and telomere rigidity in meiosis. Nat. Cell Biol. *16*, 145–156.

Shibuya, H., Morimoto, A., and Watanabe, Y. (2014b). The Dissection of Meiotic Chromosome Movement in Mice Using an In Vivo Electroporation Technique. PLoS Genet. *10*, e1004821.

Shibuya, H., Hernández-Hernández, A., Morimoto, A., Negishi, L., Höög, C., and Watanabe, Y. (2015). MAJIN Links Telomeric DNA to the Nuclear Membrane by Exchanging Telomere Cap. Cell. *163*, 1252–1266.

Shingu, Y., Mikawa, T., Onuma, M., Hirayama, T., and Shibata, T. (2010). A DNA-binding surface of SPO11-1, an Arabidopsis SPO11 orthologue required for normal meiosis. FEBS J. *277*, 2360–2374.

Shinohara, T., Orwig, K.E., Avarbock, M.R., and Brinster, R.L. (2000). Spermatogonial stem cell enrichment by multiparameter selection of mouse testis cells. Proc. Natl. Acad. Sci. U. S. A. *97*, 8346–8351.

Shroff, R., Arbel-Eden, A., Pilch, D., Ira, G., Bonner, W.M., Petrini, J.H., Haber, J.E., and Lichten, M. (2004). Distribution and dynamics of chromatin modification induced by a defined DNA double-strand break. Curr. Biol. *14*, 1703–1711.

Smith, A. V, and Roeder, G.S. (1997). The yeast Red1 protein localizes to the cores of meiotic chromosomes. J. Cell Biol. *136*, 957–967.

Smolikove, S., Eizinger, A., Hurlburt, A., Rogers, E., Villeneuve, A.M., and Colaiácovo, M.P. (2007). Synapsis-defective mutants reveal a correlation between chromosome conformation and the mode of double-strand break repair during Caenorhabditis elegans meiosis. Genetics. *176*, 2027–2033.

Snowden, T., Acharya, S., Butz, C., Berardini, M., and Fishel, R. (2004). hMSH4-hMSH5 recognizes holliday junctions and forms a meiosis-specific sliding clamp that embraces homologous chromosomes. Mol. Cell. *15*, 437–451.

Somosy, Z., Csuka, O., and Sugar, J. (1976). Electron microscopic examination of nuclear inclusions occurring as an effect of derivatives of Vinca alkaloids (Hungarian). Exp. Cell Res. *101*, 429–434.

Speed, R.M. (1982). Meiosis in the foetal mouse ovary - I. An analysis at the light microscope level using surface-spreading. Chromosoma. *85*, 427–437.

Sriraman, K., Bhartiya, D., Anand, S., and Bhutda, S. (2015). Mouse ovarian very small embryonic-like stem cells resist chemotherapy and retain ability to initiate oocyte-specific differentiation. Reprod. Sci. *22*, 884–903.

Stewart, G.S., Wang, B., Bigneli, C.R., Taylor, A.M.R., and Elledge, S.J. (2003). MDC1 is a mediator of the mammalian DNA damage checkpoint. Nature. *421*, 961–966.

Stucki, M., Clapperton, J.A., Mohammad, D., Yaffe, M.B., Smerdon, S.J., and Jackson, S.P. (2005). MDC1 directly binds phosphorylated histone H2AX to regulate cellular responses to DNA double-strand breaks. Cell. *123*, 1213–1226.

Stüven, T., Hartmann, E., and Görlich, D. (2003). Exportin 6: A novel nuclear export receptor that is specific for profilin-actin complexes. EMBO J. *22*, 5928–5940.

Su, W.P., Ho, Y.C., Wu, C.K., Hsu, S.H., Shiu, J.L., Huang, J.C., Chang, S.B., Chiu, W.T., Hung, J.J., Liu, T.L., et al. (2017). Chronic treatment with cisplatin induces chemoresistance through the TIP60-mediated Fanconi anemia and homologous recombination repair pathways. Sci. Rep. *7*, 3879.

Sugiyama, T., Kantake, N., Wu, Y., and Kowalczykowski, S.C. (2006). Rad52-mediated DNA annealing after Rad51-mediated DNA strand exchange promotes second ssDNA capture. EMBO J. *25*, 5539–5548.

Sun, H., Treco, D., and Szostak, J.W. (1991). Extensive 3’-overhanging, single-stranded DNA associated with the meiosis-specific double-strand breaks at the ARG4 recombination initiation site. Cell. *64*, 1155–1161.

Sun, M.H., Yang, M., Xie, F.Y., Wang, W., Zhang, L., Shen, W., Yin, S., and Ma, J.Y. (2017). DNA double-strand breaks induce the nuclear actin filaments formation in cumulus-enclosed oocytes but not in denuded oocytes. PLoS One. *12*, e0170308.

Sung, P. (1997). Function of yeast Rad52 protein as a mediator between replication protein A and the Rad51 recombinase. J. Biol. Chem. *272*, 28194–28197.

Svitkina, T.M., Verkhovsky, A.B., and Borisy, G.G. (1995). Improved procedures for electron microscopic visualization of the cytoskeleton of cultured cells. J. Struct. Biol. *115*, 290–303.

Swiatecka-Urban, A., Talebian, L., Kanno, E., Moreau-Marquis, S., Coutermarsh, B., Hansen, K., Karlson, K.H., Barnaby, R., Cheney, R.E., Langford, G.M., et al. (2007). Myosin Vb is required for trafficking of the cystic fibrosis transmembrane conductance regulator in Rab11a-specific apical recycling endosomes in polarized human airway epithelial cells. J. Biol. Chem. *282*, 23725–23736.

Sym, M., and Roeder, G.S. (1994). Crossover interference is abolished in the absence of a synaptonemal complex protein. Cell. *79*, 283–292.

Syrjänen, J.L., Pellegrini, L., and Davies, O.R. (2014). A molecular model for the role of SYCP3 in meiotic chromosome organisation. Elife. *3*, e02963.

Takai, A., Murata, M., Isobe, M., Mieskes, G., and Yasumoto, T. (1992). Inhibitory effect of okadaic acid derivatives on protein phosphatases. A study on structure-affinity relationship. Biochem. J. *284*, 539–544.

Tam, P.P.L., and Zhou, S.X. (1996). The allocation of epiblast cells to ectodermal and germ-line lineages is influenced by the position of the cells in the gastrulating mouse embryo. Dev. Biol. *178*, 124–132.

Tang, S., Wu, M.K.Y., Zhang, R., and Hunter, N. (2015). Pervasive and essential roles of the top3-rmi1 decatenase orchestrate recombination and facilitate chromosome segregation in meiosis. Mol. Cell. *57*, 607–621.

Tankimanova, M., Hultén, M.A., and Tease, C. (2004). The initiation of homologous chromosome synapsis in mouse fetal oocytes is not directly driven by centromere and telomere clustering in the bouquet. Cytogenet. Genome Res. *105*, 172–181.

Tease, C., and Hultén, M.A. (2004). Inter-sex variation in synaptonemal complex lengths largely determine the different recombination rates in male and female germ cells. Cytogenet. Genome Res. *107*, 208–215.

Tokuo, H., and Ikebe, M. (2004). Myosin X transports Mena/VASP to the tip of filopodia. Biochem. Biophys. Res. Commun. *319*, 214–220.

Tosi, A., Haas, C., Herzog, F., Gilmozzi, A., Berninghausen, O., Ungewickell, C., Gerhold, C.B., Lakomek, K., Aebersold, R., Beckmann, R., et al. (2013). Structure and subunit topology of the INO80 chromatin remodeler and its nucleosome complex. Cell. *154*, 1207–1219.

Totsukawa, G., Yamakita, Y., Yamashiro, S., Hartshorne, D.J., Sasaki, Y., and Matsumura, F. (2000). Distinct roles of ROCK (Rho-kinase) and MLCK in spatial regulation of MLC phosphorylation for assembly of stress fibers and focal adhesions in 3T3 fibroblasts. J. Cell Biol. *150*, 797–806.

Truong, L.N., Li, Y., Shi, L.Z., Hwang, P.Y.H., He, J., Wang, H., Razavian, N., Berns, M.W., and Wu, X. (2013). Microhomology-mediated End Joining and Homologous Recombination share the initial end resection step to repair DNA double-strand breaks in mammalian cells. Proc. Natl. Acad. Sci. U. S. A. *110*, 7720–7725.

Usui, T. (2007). Actin- and microtubule-targeting bioprobes: Their binding sites and inhibitory mechanisms. Biosci. Biotechnol. Biochem. 300–308.

Uyeda, T.Q.P., Abramson, P.D., and Spudich, J.A. (1996). The neck region of the myosin motor domain acts as a lever arm to generate movement. Proc. Natl. Acad. Sci. U. S. A. *93*, 4459–4464.

Vandekerckhove, J., and Weber, K. (1978). At least six different actins are expressed in a higher mammal: An analysis based on the amino acid sequence of the amino-terminal tryptic peptide. J. Mol. Biol. *126*, 783–802.

Verver, D.E., Langedijk, N.S.M., Jordan, P.W., Repping, S., and Hamer, G. (2014). The SMC5/6 complex is involved in crucial processes during human spermatogenesis. Biol. Reprod. *91*, 1–10.

Vicente-Manzanares, M., Ma, X., Adelstein, R.S., and Horwitz, A.R. (2009). Non-muscle myosin II takes centre stage in cell adhesion and migration. Nat. Rev. Mol. Cell Biol. 778–790.

Volkmann, N., Amann, K.J., Stoilova-McPhie, S., Egile, C., Winter, D.C., Hazelwood, L., Heuser, J.E., Li, R., Pollard, T.D., and Hanein, D. (2001). Structure of arp2/3 complex in its activated state and in actin filament branch junctions. Science. *293*, 2456–2459.

De Vries, F.A.T., De Boer, E., Van Den Bosch, M., Baarends, W.M., Ooms, M., Yuan, L., Liu, J.G., Van Zeeland, A.A., Heyting, C., and Pastink, A. (2005). Mouse Sycp1 functions in synaptonemal complex assembly, meiotic recombination, and XY body formation. Genes Dev. *19*, 1376–1389.

De Vries, S.S., Baart, E.B., Dekker, M., Siezen, A., De Rooij, D.G., De Boer, P., and Te Riele, H. (1999). Mouse MutS-like protein Msh5 is required for proper chromosome synapsis in male and female meiosis. Genes Dev. *13*, 523–531.

Wada, A., Fukuda, M., Mishima, M., and Nishida, E. (1998). Nuclear export of actin: A novel mechanism regulating the subcellular localization of a major cytoskeletal protein. EMBO J. *17*, 1635–1641.

Wakatsuki, T., Schwab, B., Thompson, N.C., and Elson, E.L. (2001). Effects of cytochalasin D and latrunculin B on mechanical properties of cells. J. Cell Sci. *114*, 1025–1036.

Wang, X., and Haber, J.E. (2004). Role of Saccharomyces single-stranded DNA-binding protein RPA in the strand invasion step of double-strand break repair. PLoS Biol. *2*, E21.

Wang, F., Kovács, M., Hu, A., Limouze, J., Harvey, E. V., and Sellers, J.R. (2003). Kinetic mechanism of non-muscle myosin IIB: Functional adaptations for tension generation and maintenance. J. Biol. Chem. *278*, 27438–27448.

Wang, N., Satirapod, C., Ohguchi, Y., Park, E.S., Woods, D.C., and Tilly, J.L. (2017). Genetic studies in mice directly link oocytes produced during adulthood to ovarian function and natural fertility. Sci. Rep. *7*, 10011.

Wang, S., Liu, J., Li, X., Ji, X., Zhang, J., Wang, Y., and Cui, S. (2016). MiR-125b regulates primordial follicle assembly by targeting activin receptor type 2a in neonatal mouse ovary. Biol. Reprod. *94*, 1–12.

Watanabe, Y., and Nurse, P. (1999). Cohesin Rec8 is required for reductional chromosome segregation at meiosis. Nature. *400*, 461–464.

Webster, A., and Schuh, M. (2017). Mechanisms of Aneuploidy in Human Eggs. Trends Cell Biol. 55–68.

Wellington, A., Emmons, S., James, B., Calley, J., Grover, M., Tolias, P., and Manseau, L. (1999). Spire contains actin binding domains and is related to ascidian posterior end mark-5. Development. *126*, 5267–5274.

Wendt, T., Taylor, D., Trybus, K.M., and Taylor, K. (2001). Three-dimensional image reconstruction of dephosphorylated smooth muscle heavy meromyosin reveals asymmetry in the interaction between myosin heads and placement of subfragment 2. Proc. Natl. Acad. Sci. U. S. A. *98*, 4361–4366.

Wieland, T., Faulstich, H., and Fiume, L. (1978). Amatoxins, phallotoxins, phallolysin, and antamanide: The biologically active components of poisonous amanita mushroom. Crit. Rev. Biochem. Mol. Biol. *5*, 185–260.

Wiltshire, T., Park, C., Caldwell, K.A., and Handel, M.A. (1995). Induced Premature G2/M-Phase Transition in Pachytene Spermatocytes Includes Events Unique to Meiosis. Dev. Biol. *169*, 557–567.

Wineland, D.., Kelpsch, D.., and Tootle, T.. (2018). Multiple pools of nuclear actin. Anat. Rec. *301*, 2014–2036.

Wojtasz, L., Daniel, K., Roig, I., Bolcun-Filas, E., Xu, H., Boonsanay, V., Eckmann, C.R., Cooke, H.J., Jasin, M., Keeney, S., et al. (2009). Mouse HORMAD1 and HORMAD2, two conserved meiotic chromosomal proteins, are depleted from synapsed chromosome axes with the help of TRIP13 AAA-ATPase. PLoS Genet. *5*, e1000702.

Wojtasz, L., Cloutier, J.M., Baumann, M., Daniel, K., Varga, J., Fu, J., Anastassiadis, K., Francis Stewart, A., Reményi, A., Turner, J.M.A., et al. (2012). Meiotic DNA double-strand breaks and chromosome asynapsis in mice are monitored by distinct HORMAD2-independent and -dependent mechanisms. Genes Dev. *26*, 958–973.

Woods, D.C., White, Y.A.R., and Tilly, J.L. (2013). Purification of oogonial stem cells from adult mouse and human ovaries: An assessment of the literature and a view toward the future. Reprod. Sci. 7–15.

Xie, A., Kwok, A., and Scully, R. (2009). Role of mammalian Mre11 in classical and alternative nonhomologous end joining. Nat. Struct. Mol. Biol. *16*, 814–818.

Xu, Y., Moseley, J.B., Sagot, I., Poy, F., Pellman, D., Goode, B.L., and Eck, M.J. (2004). Crystal structures of a formin homology-2 domain reveal a tethered dimer architecture. Cell. *116*, 711–723.

Yin, Y., and Smolikove, S. (2013). Impaired Resection of Meiotic Double-Strand Breaks Channels Repair to Nonhomologous End Joining in Caenorhabditis elegans. Mol. Cell. Biol. *33*, 2732-2747.

Yoshida, K., Kondoh, G., Matsuda, Y., Habu, T., Nishimune, Y., and Morita, T. (1998). The mouse RecA-like gene Dmc1 is required for homologous chromosome synapsis during meiosis. Mol. Cell. *1*, 707–718.

Yoshida, S., Sukeno, M., Nakagawa, T., Ohbo, K., Nagamatsu, G., Suda, T., and Nabeshima, Y.I. (2006). The first round of mouse spermatogenesis is a distinctive program that lacks the self-renewing spermatogonia stage. Development. *133*, 1495–1505.

Young, E., Briggs, S., and Miller, C. (2015). The Actin Cytoskeleton as a Therapeutic Target for the Prevention of Relapse to Methamphetamine Use. CNS Neurol. Disord. - Drug Targets *14*, 731–737.

Young, E.J., Blouin, A.M., Briggs, S.B., Sillivan, S.E., Lin, L., Cameron, M.D., Rumbaugh, G., and Miller, C.A. (2016). Nonmuscle myosin IIB as a therapeutic target for the prevention of relapse to methamphetamine use. Mol. Psychiatry. *21*, 615–623.

Young, E.J., Briggs, S.B., Rumbaugh, G., and Miller, C.A. (2017). Nonmuscle myosin II inhibition disrupts methamphetamine-associated memory in females and adolescents. Neurobiol. Learn. Mem. *139*, 109–116.

Zakharyevich, K., Ma, Y., Tang, S., Hwang, P.Y.H., Boiteux, S., and Hunter, N. (2010). Temporally and Biochemically Distinct Activities of Exo1 during Meiosis: Double-Strand Break Resection and Resolution of Double Holliday Junctions. Mol. Cell. *40*, 1001–1015.

Zakharyevich, K., Tang, S., Ma, Y., and Hunter, N. (2012). Delineation of joint molecule resolution pathways in meiosis identifies a crossover-specific resolvase. Cell. *149*, 334–347.

Zhang, J., Fujiwara, Y., Yamamoto, S., and Shibuya, H. (2019). A meiosis-specific BRCA2 binding protein recruits recombinases to DNA double-strand breaks to ensure homologous recombination. Nat. Commun. *10*, 722.

Zheng, B., Han, M., Bernier, M., and Wen, J.K. (2009). Nuclear actin and actin-binding proteins in the regulation of transcription and gene expression. FEBS J. 2669–2685.

Zhou, Y., Wang, P., Tian, F., Gao, G., Huang, L., Wei, W., and Xie, S. (2017). Painting a specific chromosome with CRISPR/Cas9 for live-cell imaging. Cell Res. 298–301.

Zhu, Z., Chung, W.H., Shim, E.Y., Lee, S.E., and Ira, G. (2008). Sgs1 Helicase and Two Nucleases Dna2 and Exo1 Resect DNA Double-Strand Break Ends. Cell. *134*, 981–994.

Zickler, D. (2006). From early homologue recognition to synaptonemal complex formation. Chromosoma. 158–174.

Acknowledgements

I would like to thank Melina Schuh for providing me with the opportunity to conduct a PhD in the Schuh lab. This has been a fantastic opportunity to work on various exciting projects, which have enabled me to learn a variety of techniques and develop as an independent researcher. Thank you also to Melina for always being available to discuss experimental results and the valuable suggestions you have regarding experiments and the overall direction of scientific projects.

I would like to thank the whole Schuh lab for the help and discussions throughout my PhD studies. Thank you also for providing a nice working environment, this made lab work even more enjoyable. I would like to say a special thank you to Alexandre Webster. Thank you for the valuable critical discussions we have shared during my PhD. These discussions helped me to refine my scientific questions and advance my scientific research projects. Thank you also to Alexandre for all the advice you provided me with during my studies. In particular, this advice helped me to further develop my laboratory and communication skills. I would also like to say thank you to Katharina Schücker for teaching me how to isolate and prepare spermatocytes for fixed cell analyses. Thank you to both Katharina Schücker and Lena Wartosch for preparing the animal licenses required for conducting live-cell imaging of spermatocytes. Thank you to Silke Schlott for conducting the live animal surgeries.

I would also like to thank the Boehringer Ingelheim Fonds (BIF) for funding a large portion of my PhD studies. Thank you also to the entire BIF team for arranging fantastic seminars and conferences. I have very fond memories from these seminars and through these events I was fortunate to meet wonderful fellow scientists.

Thanks to the members of the Schuh lab for the fantastic times outside of work we have spent together. Thank you for arranging fun events including lab excursions, movie nights, and our delicious summer barbeques. A special thanks to Alexandre Webster, Eirini Bellou, Ida Jentoft, Chris Thomas, Ninadini Sharma, and Tommaso Cavazza. I have shared such enjoyable times with you all including during our summer lake days, city trips, and biking tours! These wonderful experiences allowed me to further enjoy my time in Göttingen during my PhD studies.

Finally, and most importantly I would like to say a big thank you to my mum, Julie Charalambous. Thank you for all your support and encouragement you have provided me with throughout my studies. From my first day in school to my final days of PhD studies you have always stood by me and cheered me along, thank you so much!